

**SPIN-POLARIZED NEUTRON REFLECTIVITY AND X-RAY  
SCATTERING STUDIES ON THIN FILM SUPERCONDUCTORS**

---

**A Dissertation  
presented to  
the Faculty of the Graduate School  
University of Missouri-Columbia**

---

In Partial Fulfillment  
of the Requirements for the Degree

Doctor of Philosophy

---

by  
SANG-WOOK HAN  
Dr. Paul F. Miceli, Dissertation Supervisor

1999

## ACKNOWLEDGMENTS

As recalling my graduate school years, I would like to acknowledge the aid and support of several individuals. First, I would like to acknowledge the support of my advisor, Paul F. Miceli. Without his good nature, patient, diligent, persistent and sharp scientific insight, these works were not possible to be completed. We have started studying spin-polarized neutron reflectivity from a superconductor at MURR without any background knowledge. We had to figure out all of problems and finally met the end of a dark tunnel. What I also deeply appreciate to Paul is not only the academic help but also his humanity.

Without John F. Ankner's help for spin-polarized neutron reflectometry, the works described in this thesis could not be possible. He has sincerely supported us for the project technically as well as academically. Without his help, I could not obtain the enough knowledge of neutron reflectivity to complete this thesis work. He has introduced several books and papers of neutron scattering studies to me. He is always kind and just like an elder brother. I would like to acknowledge the support of Helmut Kaiser. As a supervisor at the MURR, he helped for the problems which were related to the MURR, such as, required paper works, equipments needed for the experiments and aid from the MURR staffs. I would like to thank Mike Killfoil, at the MURR. Without his help, I could have big troubles in the experiments at the MURR. He helped for moving the superconducting magnet,

taking care the pumps and making some toys for the experiments. And also I appreciate to the MURR machine shop, specially Ken for his sincere help.

I would like to thank my colleagues at Missouri for their companionship. Bill Elliott helped for computer works and my English. His help was the crucial for me to be familiar to the Linux system. During summer, we have played tennis at least twice a week. It helped for keeping in health mentally as well as physically. Cristian Botez, Kaile Lee and Nobuyuki Tsuchiya helped me for moral support. We are from different countries, Cristian (Romania), Kaile (China), Nobu (Japan) and me (Korea). Discussing a problem with them helped me to wisely open the eyes and to approach a problem by several different ways. My research assistantship at Missouri was funded by the Midwest Superconductivity Consortium (MISCON) under DOE grant DE-FG02-90ER45427, the NSF DMR 96-23827.

I would like to thank Professor Laura H. Greene's group at the University of Illinois-Urbana who provided samples that were the key to be successful in the works. She was always kind, sincerely interested in the project and provided useful information as well as samples for the studies. Her students, Mark Covington, Elvira Paraoanu and Igor R. Roshchin, sincerely helped for fabricating the samples to us. I would like to thank to Professor D. H. Lowndes's group at the Oak Ridge National Laboratory who provided some samples and helped for understanding the surface roughness of oxide superconductors.

I would like to thank Dr. Gian Felcher for his sincere support and help. Last

year of my graduate schools, I had a good opportunity to work with him and to use the POSYI reflectometry. He taught not only scientific knowledge but also scientific philosophy and wisdom fatherly. I appreciate to Rick Goyette for technical aid on POSYI and the computer at IPNS. I have enjoyed working with John E. Pearson, a technician at Argonne National Laboratory. I also would like to thank Professor John Ketterson and a graduate student Grant Kiehne at Northwestern University for their samples.

I would like to thank Professor James J. Rhyne for friendly discussion in any kinds of topics. Every Tuesday, he shared the lunch time with our group at the Shakespeare pizza restaurant. I would like to acknowledge Dr. John Farmer and Mike Kornecki for the SQUID magnetization measurements. They allowed and helped me to use their SQUID magnetometry. I appreciate to Dr. Lewis and Virginia Wall (once a chancellor at Western Illinois University) for their moral support. I will not forget their friendship and Virginia's cookies and lasagna. I would like to acknowledge Cliff Holmes, Sam Potts, Rod Schlotzhauer and Warren Stiefermann at the MU Physics Machine Shop for their machining. I also thank Korean friends including Kyung Pook National University Alumni in Columbia, MO for their moral support and friendship.

Without the moral and financial support of all my families, brothers, sister, sister-in-laws, my studying abroad could not succeed. Particularly, I exceedingly thank my eldest brother, Sang-Dea Han and his wife for their financial support

during my initial graduate school years. I am deeply grateful to my parents, mother who always gives endless affection to her children and father who has lived for his sons and daughter during his whole life and rests in the other world.

A very special thanks to my wife, Kyungha Im. Because of my graduate studying abroad, we could not stay together. Without her endless affection, support, tolerance and incredible patience, all of my works would be dissipated. Last year of my graduate schools, Jeahe, an unborn baby made her dad and mom always happy and keeping in the endless conjugal affection, even staying far apart (Korea-America).

To anyone and everyone whom I have forgotten to list for my acknowledgment. I am sure that one day, I will remember and feel guilty, so that you will at least have the satisfaction of living on in my neuroses.

**I dedicate my Ph. D. degree thesis works to my parents.**

SPIN-POLARIZED NEUTRON REFLECTIVITY AND X-RAY SCATTERING  
STUDIES ON THIN FILM SUPERCONDUCTORS

SANG-WOOK HAN

Dr. PAUL F. MICELI, Dissertation Supervisor

ABSTRACT

We have first demonstrated that SPNR has the unique capability to measure vortices running parallel to surface. The hysteresis loop of a  $\text{YBa}_2\text{Cu}_3\text{O}_{7-x}$  film measured by SPNR obviously demonstrated the vortices trapped by bulk and surface pinnings. In a Nb film, the magnetization measured by SPNR for ascending and descending fields applied parallel to the film plane was reversible whereas DC magnetization measurements showed a hysteresis loop. The discrepancy of SPNR and DC magnetization measurements could be explained by the vortex rotation. We also have studied one dimensional (1-D) vortex distribution in a [Nb/Al] multilayer by SPNR and DC magnetization measurements. We have developed a theoretical model calculation for 1-D spatially varying magnetization with vortices in a thin superconducting film. We have used the x-ray scattering technique to characterize films, buried interfaces and crystal structures in the films.

# TABLE OF CONTENTS

ACKNOWLEDGMENTS .....	ii
ABSTRACT .....	vi
LIST OF FIGURES .....	x
LIST OF TABLES .....	xv
Chapter	
1. General Introduction .....	1
2. Vortex Interactions in Superconductor .....	5
2.1. Introduction .....	5
2.2. Vortex-vortex Interaction .....	6
2.3. Bulk Pinning of Vortices .....	8
2.4. Vortex-surface Interaction .....	11
3. Spin-polarized Neutron Reflectivity .....	15
3.1. General Theory of SPNR .....	15
3.2. Spin-polarized Neutron Reflectometry at MURR .....	20
3.2.1. GANS Reflectometry Alignment .....	23
3.2.2. Polarizer and Polarization .....	28
3.2.3. Resolution Correction in Small Angle Reflectivity .....	33
4. One-dimensional Magnetization in Superconductor .....	37
4.1 Critical Current Model .....	37
4.2 Exact Solution of 1-D Magnetization with Vortices in Film .....	40
5. Vortices Parallel to Surface in Thin Superconducting Films .....	52

5.1.	Vortices in a $\text{YBa}_2\text{Cu}_3\text{O}_{7-x}$ Film .....	52
5.1.1.	Characterization of a $\text{YBa}_2\text{Cu}_3\text{O}_{7-x}$ Film .....	52
5.1.2.	SPNR from a $\text{YBa}_2\text{Cu}_3\text{O}_{7-x}$ Film .....	53
5.2.	Vortices measured by SPNR .....	57
5.3.	Vortices Pinned by Surface in a $\text{YBa}_2\text{Cu}_3\text{O}_{7-x}$ Film .....	64
5.4.	Vortices in a Nb Film .....	73
5.4.1.	Characterization of a Nb Film .....	73
5.4.2.	SPNR from a Nb Film .....	74
5.5.	DC Magnetization in a Nb Film .....	79
5.6.	Vortex Direction Transition .....	82
6.	Vortex Line Transition in Nb/Al Multilayered Films .....	90
6.1.	Introduction .....	90
6.2.	Characterizations of Nb/Al Multilayered Films .....	92
6.3.	DC Magnetization in Nb/Al Multilayered Films .....	92
6.4.	SPNR from a Nb/Al Multilayered Film .....	102
7.	X-ray Scattering Studies on Thin Films .....	109
7.1.	General Introduction of Reflectivity .....	109
7.2.	X-ray Diffraction from a $\text{YBa}_2\text{Cu}_3\text{O}_{7-x}$ Film .....	112
7.2.1	YBCO(2500Å)/SrTiO <sub>3</sub> by PLD .....	113
7.3.	Interdiffusion at $\text{YBa}_2\text{Cu}_3\text{O}_{7-x}$ Metal Interface .....	118
7.3.1	YBCO(300Å)/SrTiO <sub>3</sub> by Sputtering .....	119
7.3.2	Au(300Å)/YBCO(300Å)/SrTiO <sub>3</sub> by Sputtering .....	122
7.3.3	Ag(300Å)/YBCO(300Å)/SrTiO <sub>3</sub> by Coevaporation .....	124



7.3.4	Pb(300Å)/YBCO(300Å)/SrTiO <sub>3</sub> .....	125
7.4.	X-ray Reflectivity from Nb Films .....	127
7.5.	X-ray Diffraction from a Nb/Al multilayered Film .....	130
<b>References</b> .....		136
<b>Appendix</b>		
<b>Reflectivity Calculation Program for a Superconducting Film with Vor-</b>		
<b>tices</b> .....		143



## LIST OF FIGURES

Fig. 1	The schematic diagram shows a vortex located between the su- perconducting (S) and normal region (N).	.....10
Fig. 2	Vortex potentials calculated at 300 Oe, 1000 Oe and 5000 Oe as a function of position assuming a smooth surface and no bulk pinning centers in the superconductor.	.....13
Fig. 3	SPNR from a 500 Å thick NiMnSb alloy was measured as a function of q at 1000 Oe, room temperature and atmosphere.	.....19
Fig. 4	Schematic diagram of the GANS reflectometry at MURR.	.....21
Fig. 5	Sample translation scan at $2\theta = 0^\circ$ with a 6000 Å thick YBa <sub>2</sub> Cu <sub>3</sub> O <sub>7-x</sub> (2 mm thick SrTiO <sub>3</sub> substrate) mounted on a 0.8 mm thick Cd plate.	.....27
Fig. 6	Schematic diagram for the positions of the polarizer, analyzer, flippers at the GANS reflectometry.	.....29
Fig. 7	The flipping ratio at the GANS reflectometry with a supercon- ducting magnet was measured as a function of applied field at room temperature.	.....32
Fig. 8	Solid line is calculated reflectivity from a 6000 Å YBCO /SrTiO <sub>3</sub> with no surface roughness and dashed line is a Gaussian convo- luted reflectivity with a Gaussian beam profile(dotted line).	.....35
Fig. 9	Calculation for a Gaussian convoluted polarization of a 6000 Å thick YBCO /SrTiO <sub>3</sub> with H = 300 Oe and $\lambda_L = 1400$ Å with assuming different beam cuts, $\Delta q$ (dotted line), $2\Delta q$ (dashed line) and $4\Delta q$ (solid line).	.....36
Fig. 10	Magnetization in a superconducting slab calculated by using Bean model is shown at top and the bottom figures shows the local magnetic field profiles which are corresponding to the po- sitions indicated by arrows in top.	.....39
Fig. 11	Schematic diagram shows the geometry of the vortices and spin- polarized neutron reflectivity.	.....41
Fig. 12	Schematic diagram shows the vortex and its image vortices of which contribution to the local magnetic field at the surfaces vanishes.	.....42
Fig. 13	Magnetic fields are calculated with different distribution of vor- tices, assuming that $\lambda_L = 1400$ Å film thickness = 6000 Å, H = 2500 Oe and vortex density = 40 per $\mu m^2$ .	.....47
Fig. 14	Effective flux quantum is calculated as a function of vortex po- sition (dashed line) and FWHM of a Gaussian distribution of vortices (solid line), assuming that film thickness 6000 Å and $\lambda_L$ 1400 Å.	.....48

Fig. 15	Spin-up and spin-down neutrons encounter a different scattering potential due to the spatially varying magnetization in the superconductor. The scattering potential is calculated for: (Solid line) nuclear scattering only; (dot-dashed curve) London penetration without vortices; (dotted curve) vortices in the center of the sample; and a (dashed curve) uniform distribution of vortices. In each case, the lower branch is for spin-up neutrons and the upper branch is for spin-down neutrons.	.....50
Fig. 16	Calculation of $\Delta R/\bar{R}$ is for three different distributions of vortices (same average density). Inset shows the spatially varying magnetization for each case. (solid curve) vortices localized in the line through the center of the sample, (dotted curve) vortices localized on two lines and (dashed curve) vortices spread over a Gaussian distribution with FWHM, 1000 Å.	.....51
Fig. 17	(a) shows the spin-up and spin-down neutron reflectivities vs. $q$ at 300 Oe and 10 K and the solid line is a best fit. (b) shows $\Delta R/\bar{R}$ obtained from the data in (a). The solid line is the theoretical calculation with $\lambda_L = 1400$ Å.	.....54
Fig. 18	(a) shows the spin-up and spin-down neutron reflectivities vs. $q$ at 2400 Oe and 10 K. (b) shows $\Delta R/\bar{R}$ obtained from the data in (a) and the solid curve is a calculation with the theoretical model described in Ch. 4.2.	.....56
Fig. 19	Extremal $\Delta R/\bar{R}$ was measured as a function of applied field. The dotted line is the theoretical calculation, assuming that London penetration only at the surfaces contributes to the magnetization of the film. The arrows indicate the order in which the data were taken.	.....58
Fig. 20	$\Delta R/\bar{R}$ vs. $q$ were consecutively measured at 2400 Oe (a), 1200 Oe (b) and 65 Oe (c) as a function of $q$ . The solid line and dashed line are the model calculations with the same parameters except with $Qc^2$ , $\lambda_L$ and $\lambda$ .	.....59
Fig. 21	The average density of vortices was extracted from the data in Fig. 19, using a theoretical model described in Sec. 4.2.	.....61
Fig. 22	Vortex potential was calculated as a function of position with assuming $\lambda_L = 1400$ Å and $\xi = 20$ Å (dashed line). The solid line is the calculation with assuming $\lambda_L(z)$ shown in inset (solid line).	.....63
Fig. 23	(a) shows $\Delta R/\bar{R}$ measured at 40 K as a function of applied field. (b) is the average vortex density extracted from the data in (a). The arrows indicate the directions where the data were taken.	.....66
Fig. 24	The vortex densities vs. applied field were measured at 10 K, 25 K, 40 K and 55 K. The lines are for a guide to the eye.	.....67
Fig. 25	The vortex density pinned by surface as a function of applied field at 40 K (a) and 55 K (b) is extracted from the data in Fig. 24 using Eq. (5.5).	.....69

Fig. 26	The magnetic moment was measured from a Au(300Å) /YBCO(2500Å) /SrTiO <sub>3</sub> film by SQUID at zero-field cooled 4.5 K and 40 K with applied field parallel to the surface. ....	71
Fig. 27	(a) shows the reflectivities for spin-up and spin down neutrons measured at 2 K and 1000 Oe. The solid curve is a best fit. (b) shows $\Delta R/\bar{R}$ from the data in (a) and the solid line is theoretical calculation with assuming no vortices and dashed and dotted curves with assuming vortices. ....	75
Fig. 28	$\Delta R/\bar{R}$ at $2\theta$ of $0.38^\circ$ was measured for increasing and decreasing field. The lines are for a guide to the eye. ....	76
Fig. 29	(a) shows the $\Delta R/\bar{R}$ at $H = 600$ Oe and $T = 2$ K and the lines are the theoretical calculations with different magnetic screening lengths. (b) shows the polarization at $H = 2000$ Oe after the field cycling to 3000 Oe. The lines are a best fit, assuming that vortices are uniformly distributed through the sample (solid line), in the middle line of the sample (dashed line), and in two rows (dotted line). ....	78
Fig. 30	Density of vortices was extracted from the data in Fig.28 assuming a uniform distribution of vortices and $\lambda_L$ 490 Å. ....	79
Fig. 31	Magnetic moment are measured as a function of applied field with different tilt angle at 2 K, by using a SQUID magnetometer and the solid lines are for a guide of the eye. The inset shows the slope of the magnetization in the linear region of small field as a function of tilt angle. The solid line is a best fit to a model described in the text. ....	81
Fig. 32	(a) shows magnetization measured by SPNR. (b) the dotted line shows the measured magnetization by a SQUID magnetometer, open circle is the recalculated magnetization from the data in (a) for ascending field and closed circle is for descending field, assuming the vortex changing their direction perpendicular to the surface. ....	84
Fig. 33	The dotted line shows the measured magnetization by a SQUID magnetometer, open circle is the recalculated magnetization from the data in Fig. 32 (a) for ascending field and closed circle is for descending field, assuming that the total flux due to the vortices is constant and change their direction perpendicular to the surface. ....	86
Fig. 34	(a) shows the extracted vortex density running perpendicular (open circle) and parallel (solid circle) to the surface, basing on the data in Fig. 30 (b). (b) shows the vortex angle, $\omega = \tan^{-1}(n_\perp \Phi_o / n_\parallel \Phi_{eff})$ , as the applied field decreased from 3000 Oe to zero. ....	87
Fig. 35	Magnetizations as a function of applied field at 2.2 K were measured on Nb/Al multilayers by a SQUID magnetometer. The field applied parallel to the surface. The arrows indicate maxima. ....	93

Fig. 36	Effective flux quantum was calculated as a function of vortex core position for a single vortex (dashed line) and FWHM of a Gaussian distribution of vortices (solid line), assuming $\lambda_L = 1500 \text{ \AA}$ and film thickness $2200 \text{ \AA}$ .	....95
Fig. 37	SQUID magnetic moment was measured at two different tilt angles. The arrows indicate the maxima.	....98
Fig. 38	The magnetization slopes below $H_{c1}$ were measured as a function of tilt angle at 2 K and 4.5 K. The data of 4.5 K was intentionally shifted down. The solid lines are a best fit to the model calculation described in Sec. 5.4.	... 100
Fig. 39	Hysteresis loop was measured on a Nb/[Al( $20 \text{ \AA}$ )/Nb( $70 \text{ \AA}$ )] $\times$ 20 multilayer at 2 K with tilt angle of $2.15^\circ$ . The arrows indicate the positions of the maxima and the solid line is for a guide to the eye.	... 101
Fig. 40	(a) shows the grazing neutron reflectivity from a Nb( $180 \text{ \AA}$ )/[Al( $20 \text{ \AA}$ )/Nb( $72 \text{ \AA}$ )] $\times$ 20/Si film measured as a function of $q$ at 2 K and 700 Oe. The solid line is a best fit. (b) shows the normalized reflectivity difference for spin up and spin down neutrons obtained from the data in (a). The solid line is a best fit and shows $\lambda_L = 1500 \pm 200 \text{ \AA}$ .	... 103
Fig. 41	The polarizations were measured at zero-field cooled 1500 Oe (a), 2000 Oe (b) and 2 K on a Nb( $70 \text{ \AA}$ )/Al( $20 \text{ \AA}$ ) multilayer. The lines are a best fit with assuming different distribution of vortices and the magnetic screening length $1500 \text{ \AA}$ .	... 105
Fig. 42	(a) shows the polarization at 2000 Oe and 2 K after the field cycling to 5400 Oe. For a best fit, a Gaussian distribution of vortices with FWHM $400 \text{ \AA}$ (solid line) and a uniform distribution of vortices (dotted line) are assumed. (b) shows the scattering density profile corresponding to the solid line in (a) for spin-up neutrons as a function of position. The inset is a vertical expansion.	... 107
Fig. 43	Normalized scattering density profile for a Gaussian distribution of surface high. Solid line shows slices in multi-sliced method.	... 111
Fig. 44	X-ray reflectivity was measured on a YBCO( $2500 \text{ \AA}$ )/SiTiO <sub>3</sub> film vs. $2\theta$ . The solid curve is a best fit.	... 113
Fig. 45	X-ray transverse scans from a YBCO( $2500 \text{ \AA}$ )/SiTiO <sub>3</sub> film at different $2\theta$ .	... 115
Fig. 46	Top shows the Bragg peaks of YBCO and SrTiO <sub>3</sub> . Bottom shows the broadenings of Bragg peaks as a function of $\theta$ and the solid line is a best fit.	... 116
Fig. 47	(a) shows the Bragg diffraction at (102) of YBCO single crystal and (b) for (108) Bragg peak.	... 118
Fig. 48	X-ray reflectivity was measured on a $300 \text{ \AA}$ thick YBCO on a SrTiO <sub>3</sub> . The solid curve is a best fit. The film oscillations correspond to the $210 \text{ \AA}$ thickness of the YBCO. The scattering density profile of the sample is shown in the inset.	... 120

Fig. 49	(a) shows the Bragg diffraction from a c-axis YBCO single crystal on a $\text{SrTiO}_3$ (001) substrate. (b) shows the broadenings of the YBCO Bragg peaks in (a) vs. $\theta$ .	... 121
Fig. 50	X-ray reflectivity was measured from $\text{Au}(300\text{\AA}) / \text{YBCO}(300\text{\AA}) / \text{SrTiO}_3$ film and the solid line is a best fit. The scattering density profile of the film is shown in the inset.	... 123
Fig. 51	X-ray reflectivity was measured from $\text{Ag}(300\text{\AA}) / \text{YBCO}(300\text{\AA}) / \text{SrTiO}_3$ film and the solid line is a best fit. The inset shows the scattering density profile of the film.	... 124
Fig. 52	X-ray reflectivity was measured as a function of $2\theta$ from $\text{Pb} / \text{YBCO} / \text{SrTiO}_3$ films. (a) $\text{Pb}$ was sputtered <i>ex-situ</i> on a YBCO film and (b) $\text{Pb}$ was evaporated <i>in-situ</i> on a YBCO film. The insets show the scattering density profiles.	... 126
Fig. 53	(a) shows the grazing angle x-ray reflectivity from $\text{Nb}(144\text{\AA}) / \text{Al}_2\text{O}_3$ , (b) from $\text{Al}(760\text{\AA}) / \text{Nb}(1380\text{\AA}) / \text{Al}_2\text{O}_3$ and (c) from $\text{Nb}(97\text{\AA}) / \text{InAs}$ .	... 128
Fig. 54	X-ray reflectivity from a $\text{Nb} / [\text{Al}(19\text{\AA}) / \text{Nb}(74\text{\AA})] \times 20 / \text{Si}$ film is measured as a function of $2\theta$ .	... 131
Fig. 55	X-ray transverse scans from $\text{Nb} / [\text{Al}(19\text{\AA}) / \text{Nb}(74\text{\AA})] \times 20 / \text{Si}$ at different $2\theta$ are shown.	... 133
Fig. 56	X-ray diffraction from $\text{Nb} / [\text{Al}(19\text{\AA}) / \text{Nb}(70\text{\AA})] \times 20 / \text{Si}$ was measured as a function of $2\theta$ .	... 134

## LIST OF TABLES

TABLE 1	Spin-polarized Neutron Reflectometry in the World	.....22
TABLE 2	The maximum positions vs. Nb thickness	.....93





## 1. GENERAL INTRODUCTION

Grazing angle x-ray and neutron reflectivities have been widely used for academic research because of their sensitivity to interfaces. They are a simple, convenient and unique technique to study buried interfaces without destroying a sample. X-rays interact with electrons [1] and neutrons are scattered by nuclei [2]. Although x-ray and neutron could be used to study magnetic structures at higher angle, near a Bragg peak [2,3], grazing angle spin-polarized neutron reflectivity (SPNR) is a unique tool to reveal the magnetic profile perpendicular to the film surface [4].

The application of SPNR to thin-film superconductors was first demonstrated by G. Felcher *et al.* [6] where the London penetration length  $\lambda_L$  was measured for Nb. Further refinement of the technique for Nb by H. Zhang *et al.* [7] included the effect of the electron mean-free path on  $\lambda_L$ . The technique has also been used to determine  $\lambda_L$  for high-temperature superconducting oxides [32]. All of these studies were performed at low field, below  $H_{c1}$ .

As a superconductor is placed at a small magnetic field, the electrons in the superconducting state (superelectrons) try to expel the field from the superconductor. Therefore, the field is exponentially decayed from the surface over the length scale, London penetration depth [5]. At higher field, quantized magnetic

fluxes, vortices, will be generated in a type-II superconductor because for  $H > H_{c1}$ , the Gibbs free energy difference between superconducting and normal states is too big to expel the field by the superelectrons. The behavior of magnetic vortices is a subject of both fundamental and practical importance. The interaction between vortices as well as their interaction with pinning centers can lead to complex magnetic phase diagrams: vortices may order in a lattice or exhibit glassy or liquid behavior. These properties have been extensively studied in both conventional and high temperature superconductors [9–12]. Current-transport properties, which are central to technological applications of superconductors, strongly depend on the pinning of vortices.

For these reasons, there is considerable interest in having the capability to examine the spatial configuration of vortices. Several techniques have been used, including surface decoration with magnetic particles [13], electron microscopy [14], scanning tunneling microscopy [15], Hall probe microscopy [16], electron holography [17], and small-angle diffraction [12,18]. With the exception of the latter, these methods only image vortices at their point of exit through the surface. However, neutron diffraction requires both an long-range ordered lattice of vortices as well as large-volume samples so that films cannot be investigated.

We have first demonstrated that the specular reflection of spin-polarized neutrons can be used to study vortices in *thin-film* superconductors [19]. The method makes possible the study of a unique geometry whereby vortices which run parallel to the surface can be investigated. Moreover, an ordered vortex lattice is

not necessary for this technique so that one can study the vortex distribution in the direction perpendicular to the surface and it will give an opportunity to study the vortex-surface interaction.

The vortex-surface interaction has been studied by measuring the average magnetization in specimens. A first maximum (small bump) in a magnetization curve just above  $H_{c1}$  was first observed by J. Guimpel *et al.* [20] in Nb/Cu multilayers by using a SQUID magnetometer with applied field near parallel to the surface. They explained the maximum with vortex rearrangement, one row to two rows, comparing with a model calculation for the minimizing the Gibbs free energy in a superconductor with vortices. S. H. Brongersma *et al.* [21] have also studied the maxima in Nb/Cu multilayers, by using a torque magnetometer with applied field near parallel to the surface. And they reported the observation of several maxima in the magnetization curve with the results of Monte Carlo simulations in which they chose 60 vortices in a superconductor and allow them freely located, minimizing the free energy under a given field. And the maxima were consecutively found in a Nb/Ti multilayer by the AC susceptibility measurements [22], Nb/Si multilayer [23] and Nb/Al [24] by SQUID magnetization measurements.

The non-superconducting layers in the multilayers might help strong anisotropy in the superconductor and the vortices would sit in the non-superconducting layers which might be in the less density of Cooper pairs. However, above described techniques measure only the average magnetization which run parallel and perpendicular to the surface [25]. With a torque magnetometry,

one will measure only the magnetization which is perpendicular to applied field [26]. The vortices in a thin film under an applied field tilted to the surface is partial to staying in nearly parallel or nearly perpendicular to the surface because the vortices staying with a intermediate angle will create extra free energy [27]. The vortex transition of direction to the perpendicular to the surface will considerably contribute to the measured magnetization even with the demagnetization [25]. Therefore, the measurement of vortices which run parallel to the surface would be crucial to understand the vortex distribution in a thin-film for studying the vortex-surface interaction.

In this thesis, I will introduce the vortex interactions in Ch. 2 and the SPNR technique in Ch. 3. And I will describe a theoretical model calculation of a one-dimensional spatially varying magnetization with vortices in a *thin-film* superconductor in Ch. 4. The experimental results of vortices in a  $\text{YBa}_2\text{Cu}_3\text{O}_{7-x}$  film measured by SPNR and the comparison of magnetization in a Nb film measured by SPNR and SQUID magnetometer will be discussed in Ch. 5. And I will discuss the studies of vortex distribution in Nb/Al multilayer in Ch. 6. Finally, x-ray scattering studies on *thin-films* will be shown in Ch. 7.



## 2. VORTEX INTERACTIONS IN SUPERCONDUCTOR

### 2.1. Introduction

Superconductor could be defined by two characteristics, perfect conductor and diamagnetic. At small field, Meissner region, the magnetization in a superconductor linearly decreases with applied field increasing. Above a lower critical field,  $H_{c1}$  the magnetization in a superconductor called type-I superconductor will be vanished immediately whereas a type-II superconductor will generate vortices and the magnetization of a type-II superconductor rather slowly approaches zero up to a upper critical field,  $H_{c2}$ . The critical fields for an isotropic and uniform superconductor,  $H_{c1} = (\Phi_o/4\pi\lambda_L^2)K_o(\xi/\lambda_L)$  and  $H_{c2} = \Phi_o/2\pi\xi^2$  are predicted by Ginzburg-Landau theory [5], where  $\Phi_o$  is the vortex flux quantum,  $ch/2e = 20.679$  G  $\mu\text{m}^2$ ,  $\lambda_L$  is London penetration depth,  $\xi$  is coherence length and  $K_o$  is a modified Bessel function. The typical  $H_{c1}$  is couple of hundred Oersted (Oe) for a bulk superconductor. However  $H_{c1}$  of a thin film superconductor depends on applied field direction to the film plane. At a few Oe, vortices could pierce a thin film superconductor for applied field perpendicular the the film plane while for applied field parallel to the surface,  $H_{c1}$  shown in Eq. (5.2) which is considerably higher than  $H_{c1}$  of the bulk superconductor.  $H_{c2}$  for conventional superconductors is several Kilo-Oe. However an oxide superconductor will keep its superconductivity up to

couple of hundred Tesla.

For  $H < H_{c1}$ , the local magnetic field will be described by the London equation [5].

$$\vec{B} + \lambda_L^2 \nabla \times \nabla \times \vec{B} = 0 \dots\dots\dots(2.1)$$

At a higher field,  $H > H_{c1}$ , vortices will enter a type-II superconductor. For a single vortex, the equation (2.1) will be modified to [5]

$$\vec{B} + \lambda_L^2 \nabla \times \nabla \times \vec{B} = \Phi_o \delta^2(\vec{r} - \vec{r}_o) \dots\dots\dots(2.2)$$

where  $\delta^2(\vec{r} - \vec{r}_o)$  is a two dimensional delta function. For an isotropic, uniform superconductor of infinite extent, the magnetic field due to a vortex could be determined by solving Eq. (2.2).

$$\vec{B} = \frac{\Phi_o}{2\pi\lambda_L^2} K_0 \left( \frac{\sqrt{|\vec{r} - \vec{r}_o|}}{\lambda_L} \right) \dots\dots\dots(2.3)$$

Once vortices enter a practical superconductor, a vortex will interact with neighboring vortices, defects (pinning centers) and the surfaces.

## 2.2. Vortex-vortex Interaction

Assuming an isotropic, uniform superconductor, consider two vortices located at  $r_1$  and  $r_2$  in the superconductor. The total free energy in the supercon-



ductor [5] can be described by

$$W_T = W_o + \frac{L_V}{2} \int_s \vec{B}_V \cdot \vec{V}(\vec{r}) da \dots\dots\dots (2.4)$$

where  $W_o$  is the total free energy of the superconductor without the vortices,  $L_V$  is the length of the vortices,  $B_V$  is the magnetic field due to the vortices and  $V(\vec{r}) = \Phi_o\{\delta^2(\vec{r}_1)+\delta^2(\vec{r}_2)\}$ . The magnetic fields due to a single vortex was described in Eq. (2.3). The magnetic field due to the vortices of which directions are parallel each other will be found to be,

$$\begin{aligned} \vec{B}_V = & \frac{\Phi_o}{2\pi\lambda_L^2} \left\{ K_o \left( \frac{\sqrt{(z-z_1)^2 + (y-y_1)^2}}{\lambda_L} \right) \right. \\ & \left. + K_o \left( \frac{\sqrt{(z-z_2)^2 + (y-y_2)^2}}{\lambda_L} \right) \right\} \hat{x} \dots\dots\dots (2.5) \end{aligned}$$

where orientation of vortices along x-axis was assumed.

By replacing Eq. (2.5) into Eq. (2.4) and assuming the core of vortex is normal over the radius,  $\xi$ , the free energy is calculated to,

$$W_T = W_o + \frac{\Phi_o^2 L_V}{2\pi\lambda_L^2} \left\{ K_o \left( \frac{\xi}{\lambda_L} \right) + 2K_o \left( \frac{\rho}{\lambda_L} \right) \right\} \dots\dots\dots (2.6)$$

where  $\rho$  is the distance between vortices,  $\sqrt{(z_1 - z_2)^2 + (y_1 - y_2)^2}$ . The first term is from the free energy of the vortices themselves and the second term is due to the vortex-vortex interaction.

From Eq. (2.6), the force of which a vortex at  $\vec{r}_1$  exerts on the other one at  $\vec{r}_2$  can be calculated to

$$\vec{F}_{12} = \frac{\Phi_o^2 L_V}{2\pi \lambda_L^3} K_1 \left( \frac{\rho}{\lambda_L} \right) \hat{\rho} = L_V \vec{J}_{12} \times \Phi_o \hat{x} \dots\dots\dots (2.7)$$

where  $K_1(r)$  is the modified Bessel function of second kind of order 1 and  $J_{12}$  is the density of current at  $\vec{r}_2$  generated by the vortex at  $\vec{r}_1$ . The supercurrent density could be found with assuming that the electric field in the superconductor is negligible.

$$\vec{J}_s = \nabla \times \vec{B} \dots\dots\dots (2.8)$$

This result shows that the vortices oriented in the same direction are repulsive each other and depends on the distance between vortices and London penetration depth. Also the force is proportional to the density of current at the vortex position. When current is applied through a superconductor, the current will force vortices to move.

### 2.3. Bulk Pinning of Vortices

Practical superconductors has defects, bulk pinning centers of vortices at which superelectron density is lower than at other regions. When a vortex enter a superconductor which has defects, the vortex will interact with the defects. The free energy difference between the normal and superconducting state of a vortex

core [5] is

$$\Delta E_{core} = \frac{1}{2} H_c^2 V_V \dots\dots\dots (2.9)$$

where  $H_c$  is the thermodynamic critical field,  $\Phi_o/(2\sqrt{2}\pi\lambda_L\xi)$  and  $V_V$  is the volume of a vortex core,  $\pi\xi^2 L_V$ , as shown in Fig. 1. It shows that if the core of a vortex stays in the superconducting region, the free energy will be increased by the amount of  $\Delta E_{core}$ . The energy difference depending on the vortex position will create a force to the vortex.

Assuming a normal region is somewhat bigger than the diameter of a vortex core and the core is located between the normal and superconducting region, as shown in Fig. 1. The equation (2.9) shows that the energy difference of the core depends on the volume which occupies the superconducting region. The volume of the core which is located in the superconducting region is

$$V_S = l\sqrt{\xi^2 - l^2} - \cos^{-1}\left(\frac{l}{\xi}\right)\xi^2 \dots\dots\dots (2.10)$$

where  $|l| \leq \xi$ . If the core of a vortex is totally located in the normal region or in the superconducting region, the free energy of the core will not depend on the core position.

With Eqs. (2.9) and (2.10), the energy difference could be calculated as a function of  $l$ . And then the pinning force to the core due to the normal boundary

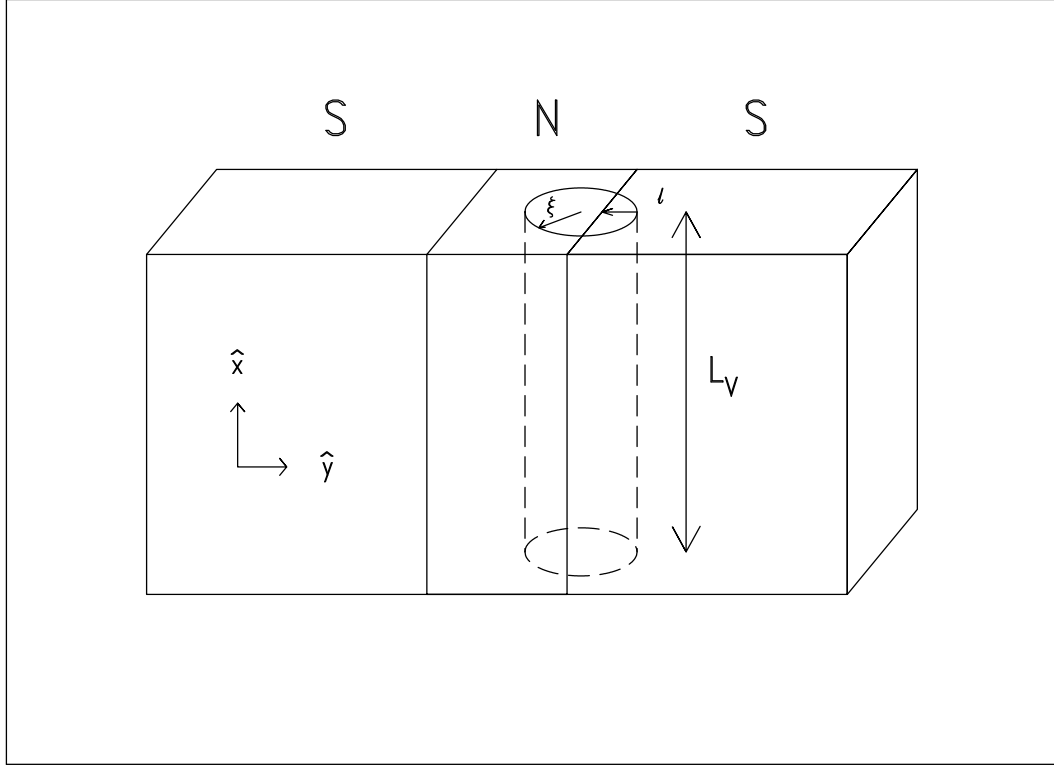


FIG. 1. The schematic diagram shows a vortex located between the superconducting (S) and normal region (N).

can be found to be,

$$\vec{F}_p = -\frac{\partial}{\partial l} \Delta E_{core} \hat{y} = -\frac{\Phi_o^2 L_V}{8\pi \lambda_L^2 \xi^2} \sqrt{\xi^2 - l^2} \hat{y} \dots \dots \dots (2.11)$$

It shows that the pinning force to a vortex core is attractive and depends on the coherence length and position of the core.

From Eq. (2.11), the maximum pinning force can be found at  $l = 0$  where the center of the vortex core is located at the boundary.

$$\vec{F}_{max} = -\frac{\Phi_o^2 L_V}{8\pi\lambda_L^2\xi}\hat{y} \equiv \vec{J}_c \times \Phi_o L_V \hat{x} \dots\dots\dots (2.12)$$

where  $J_c$  is the critical current density above which a vortex starts to move. This model calculation shows that the vortex pinning force depends on  $\lambda_L$  and  $\xi$  which are temperature dependent [29]. The critical current density is somewhat smaller than the depairing critical current density,  $\Phi_o/(3\sqrt{3}\pi\lambda_L^2\xi)$  [5] at which the Cooper pairs depair because of an external force. In a practical superconductor,  $J_c$  is a factor of order smaller than this model calculation because the bulk pinning force depends on the shape of a superconductor and also the size and shape of a pinning center.

The interaction forces, vortex-vortex and bulk pinning of vortex, depends on temperature. Thus, the vortices stay in a lattice or randomly distribute through a superconductor, depending on temperature. These properties have been intensively studied with several techniques, as mentioned in Ch. 1.

## 2.4. Vortex-surface Interaction

As vortices are located parallel to the surfaces of a superconductor, the vortices will interact with the boundaries, their image vortices as well as the surface screening field at a boundary. Below we assume a single vortex is placed parallel

to a single boundary of a uniform superconductor, the total free energy of the superconductor with the vortex [5] would be described to,

$$W_T = W_o + \int_{v_s} \vec{V}(\vec{r}) \cdot (\vec{B}_L + \frac{1}{2}\vec{B}_V - \vec{H}) dv \dots\dots\dots (2.13)$$

where  $W_o$  is the total free energy of the superconductor without the vortex,  $v_s$  is the volume of the superconductor,  $\vec{V}(\vec{r}) = \delta^2(\vec{r})$ ,  $\vec{B}_L$  is the magnetic field of surface screening and  $\vec{B}_V$  is the magnetic field due to the vortex and its image vortices.

The total free energy of the superconductor,  $W_T$ , will be found to,

$$W_T = W_o + \Phi_o \vec{H} L_V (e^{-z'/\lambda_L} - 1) + \frac{\Phi_o^2 L_V}{4\pi\lambda_L^2} \left\{ K_o \left( \frac{\xi}{\lambda_L} \right) - K_o \left( \frac{|2z'|}{\lambda_L} \right) \right\}. (2.14)$$

where the vortex position relative to surface is  $z'$  and the core of vortex is assumed to be normal.

The thermodynamic potential per vortex and per unit length,  $\Delta W = (W_T - W_1)/(\Phi_o L_V)$ , in the superconductor will be an interesting quantity because it will provide the information on  $H_{c1}$ . Figure 2 (a), (b) and (c) show the vortex potential as a function of the vortex position. For the calculation, a  $\text{YBa}_2\text{Cu}_3\text{O}_{7-x}$  (YBCO) superconductor with London penetration depth, 1400 Å [8] and the coherence length, 16 Å [9] is assumed. As the thickness of the superconductor goes to infinite, the surface and image vortex contribution to the free energy would be ignored. The total energy difference per vortex and unit length of vortex,  $\Delta W$ , will be  $\Phi_o/(4\pi\lambda_L^2)K_o(\frac{\xi}{\lambda_L}) = H_{c1}$ , the low critical field for a bulk superconductor.

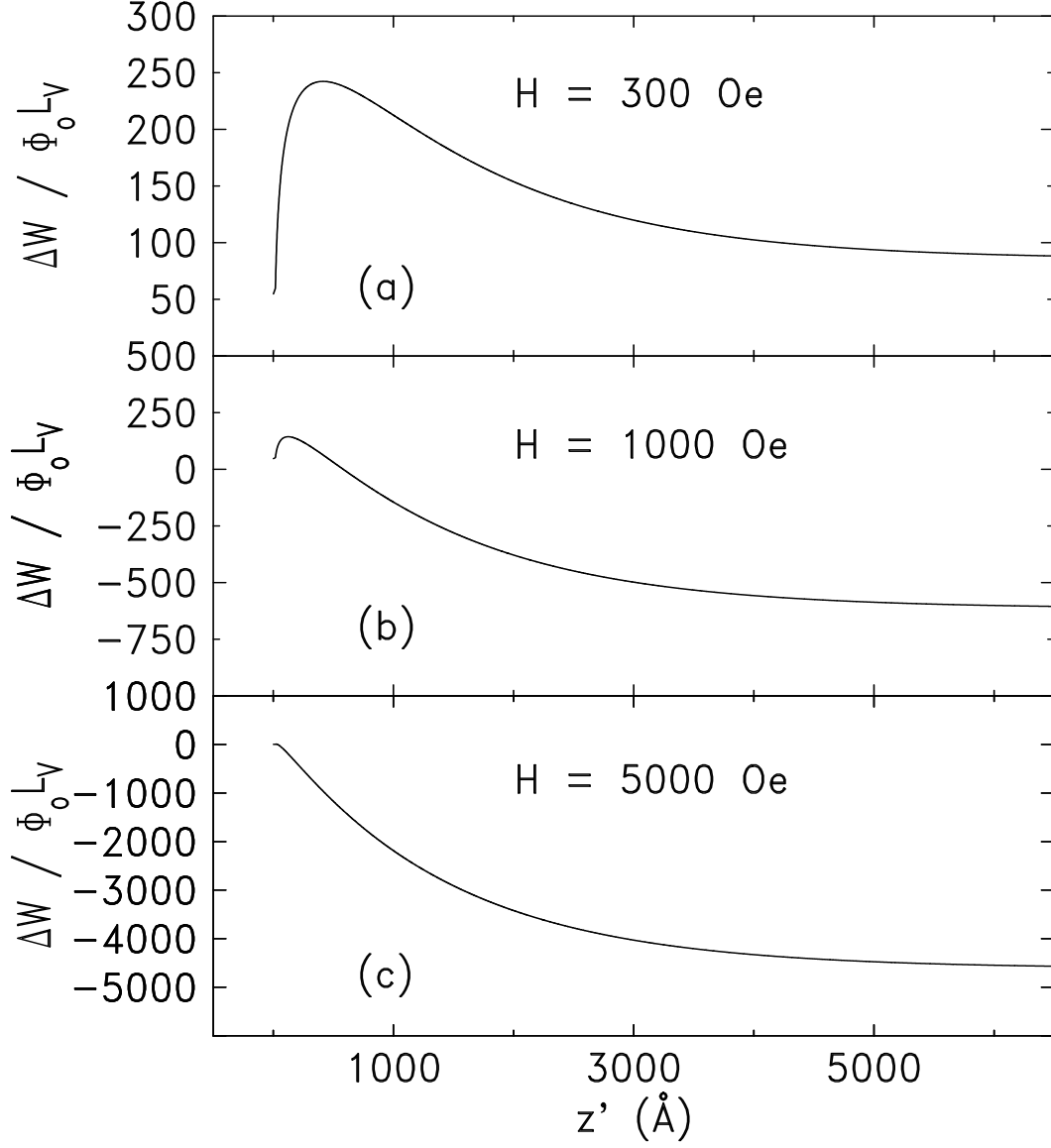


FIG. 2. Vortex potentials calculated at 300 Oe, 1000 Oe and 5000 Oe as a function of position assuming a smooth surface and no bulk pinning centers in the superconductor.

The lower critical field  $H_{c1}$ , for a YBCO superconductor is calculated to be  $\sim 372$  Oe, using  $\lambda_L$  1400 Å and  $\xi$  16 Å. Figure 2 shows that at applied field above the critical field,  $H > H_{c1}$ , there is a barrier for a vortex to enter the superconductor because of the image vortex. Once if a vortex enters the superconductor, it will

move toward the middle of the superconductor. However a practical superconductor has the surface roughness and bulk pinning centers, defects that will affect to the vortex potential [30].

From Eq. (2.14), the force on the vortex could be calculated.

$$\vec{F} = -\frac{\Delta W}{\Delta z'} \hat{z} = \frac{\Phi_o H}{\lambda_L} e^{-z'/\lambda_L} \hat{z} - \frac{\Phi_o^2}{2\pi\lambda_L^3} K_1\left(\frac{2z'}{\lambda_L}\right) \hat{z} \dots\dots\dots (2.15)$$

This calculation result shows that the surface pushes a vortex into superconductor whereas the image vortex pulls a vortex from superconductor. The surface contribution to the interaction depends on applied field however the force due to image vortex is constant to applied field. Therefore, as the applied field increased, the force pushing a vortex toward a superconductor is getting stronger. It might be the explanation why vortices more easily enter a superconductor at a high field. In Chap.5, the vortex-surface interaction in a *thin-film* superconductor will be discussed in detail.





### 3. SPIN-POLARIZED NEUTRON REFLECTIVITY

#### 3.1. General Theory of Spin-polarized Neutron Reflectivity

As a neutron propagates through a medium, the wave function as well as the flux of the neutron can be known by solving a Schrödinger equation.

$$\left( -\frac{\hbar^2}{2m_n} \nabla^2 + V(\vec{r}) \right) \Psi(\vec{r}) = E \Psi(\vec{r}) \dots\dots\dots (3.1)$$

where  $m_n$  is the neutron mass,  $V(\vec{r})$  is neutron optical potential. The neutron potential,  $V(\vec{r})$ , is determined by the scattering length and the density of nuclei, as well as the magnetization from the electrons in a unfilled shell and nuclear spins. The nuclear scattering of a neutron can be described within the Born approximation by the Fermi pseudo-potential [2].

$$V_n(\vec{r}) = \frac{2\pi\hbar^2}{m_n} \sum_i b_{ci} \delta(\vec{r} - \vec{R}_i) = \frac{2\pi\hbar^2}{m_n} N_n \langle b_c \rangle \dots\dots\dots (3.2)$$

where  $b_{ci}$  is the  $i^{th}$  bound coherent scattering length,  $N_n$  is the density of nuclei,  $\langle b_c \rangle$  is the average bound coherent scattering length and assumed that the averaged incoherent scattering density is negligible. The magnetic scattering for spin-polarized neutrons is determined by the neutron magnetic moment and the

magnetization [31].

$$V_m(\vec{r}) = -\vec{\mu}_n \cdot \vec{M}(\vec{r}) \dots\dots\dots (3.3)$$

where  $\mu_n$  is the neutron magnetic moment and  $\vec{M}(\vec{r})$  is the spatially varying magnetization. The neutron magnetic moment is described to,  $\vec{\mu}_n = \gamma \mu \vec{\sigma}$ , where  $\gamma$  is the magnetic dipole moment of a neutron, -1.913,  $\mu$  is nuclear magneton,  $e \hbar / 2 m_p = 5.049 \times 10^{-27}$  J(Joule)/T(Tesla) and  $\vec{\sigma}$  is a Pauli matrix.

Let's assume that  $z$ -axis is perpendicular to the film surface and in the scattering plane determined by incident neutron wave vector and exiting neutron wave vector. And  $x$  and  $y$  axes are assumed in the film plane and the neutron is assumed to be polarized in  $x$ -axis. The magnetization which contributes to the neutron scattering will be,

$$\vec{M}(\vec{r}) = M_x \hat{x} + M_y \hat{y} \dots\dots\dots (3.4)$$

and the Pauli matrix of neutron is,

$$\vec{\sigma} = \begin{pmatrix} 1 & 0 \\ 0 & -1 \end{pmatrix} \hat{x} + \begin{pmatrix} 0 & 1 \\ 1 & 0 \end{pmatrix} \hat{y} + \begin{pmatrix} 0 & -i \\ i & 0 \end{pmatrix} \hat{z} \dots\dots\dots (3.5)$$

Therefore, the Eq. (3.3) can be separated to four different magnetic scattering potentials:

$$\left. \begin{aligned} V_m^{++}(\vec{r}) &= -\gamma\mu M_x(\vec{r}) \\ V_m^{--}(\vec{r}) &= \gamma\mu M_x(\vec{r}) \\ V_m^{+-}(\vec{r}) &= -\gamma\mu M_y(\vec{r}) \\ V_m^{-+}(\vec{r}) &= \gamma\mu M_y(\vec{r}) \end{aligned} \right\} \dots\dots\dots (3.6)$$

where  $^{++}$  is for the spin-up of a incident and exiting neutron,  $^{--}$  is for the spin down of a incident and exiting neutron,  $^{+-}$  is for spin-up of a incident neutron and spin down of the exiting neutron and  $^{-+}$  is for spin down of a incident neutron and spin-up of the exiting neutron. It shows that the magnetization parallel or anti-parallel to the polarized direction of a incident neutron,  $M_x\hat{x}$ , does not affect the exiting neutron spin state. However the magnetization perpendicular to the polarized direction of a neutron,  $M_y\hat{y}$ , makes the exiting neutron spin flip. For the neutron spinors, the Schrödinger equation, Eq. (3.1), can be changed to,

$$\left. \begin{aligned} \left(-\frac{\hbar^2}{2m_n}\nabla^2 + V_n(\vec{r}) + V_m^{++}(\vec{r})\right) \Psi_+(\vec{r}) + V_m^{-+}\Psi_-(\vec{r}) &= E\Psi_+(\vec{r}) \\ \left(-\frac{\hbar^2}{2m_n}\nabla^2 + V_n(\vec{r}) + V_m^{--}(\vec{r})\right) \Psi_-(\vec{r}) + V_m^{+-}\Psi_+(\vec{r}) &= E\Psi_-(\vec{r}) \end{aligned} \right\} \dots\dots\dots (3.7)$$

However, as the magnetization is near parallel or anti-parallel to the neutron spin direction, the spin flip scattering can be ignored. Then the Schrödinger equation for neutron spinors can be changed to a homogeneous Helmholtz equation which includes a magnetization scattering.

$$\left. \begin{aligned} \left\{ \nabla^2 + K^2 \left[ 1 - \left( \frac{4\pi}{K^2} N_n < b_c > \mp \frac{2m_n}{\hbar^2 K^2} \mu_n M_x(\vec{r}) \right) \right] \right\} \Psi_{\pm} \\ = \{ \nabla^2 + K^2 n^2(\vec{r}) \} \Psi_{\mp} = 0 \end{aligned} \right\} \dots\dots\dots (3.8)$$

where  $n(\vec{r})$  is a refractive index.

For the reflectivity condition where momentum is transferred only perpendicular to the film surface,  $z$ -axis, reflectivity will give the spatial information of optical potential along only  $z$ -axis. Thus, the magnetization  $M(\vec{r})$  should be averaged over  $x$ -axis and  $y$ -axis. With given neutron scattering density assuming constant magnetization, one can solve the Schrödinger equation, Eq. (3.8), and find the reflectivities for spin up neutrons and spin down neutrons as a function of momentum transfer,  $q_z = 4\pi \sin\theta/\lambda$  where  $\theta$  is the half angle between incident and exiting wave vectors and  $\lambda$  is the incident beam wave length.

$$R_{\pm} = \left| \frac{q_z - \sqrt{q_z^2 - (16\pi N_n \langle b_c \rangle)^2 \mp (1.162 \times 10^{-8} M)^2}}{q_z + \sqrt{q_z^2 - (16\pi N_n \langle b_c \rangle)^2 \mp (1.162 \times 10^{-8} M)^2}} \right|^2 \dots\dots\dots (3.9)$$

where the magnetization  $M$  is in a Gauss unit.

Eq. (3.9) clearly demonstrates that SPNR would be affected by magnetization. Figure 3 shows SPNR near the critical angle measured as a function of  $q$  from a 500 Å thick NiMnSb alloy at 1000 Oe. SPNR which is sensitive to the spatial gradient of magnetization has been used to study magnetic structure in thin films [4], to measure a magnetic screening length of superconductors at a small magnetic field [6,8,7] and also to study the superconducting surface sheath [32]. At a high field, the vortices will be generated in a type-II superconductor. The magnetization in a thin film superconductor will be contributed by the vortices and the London penetration at the surfaces. This technique should give an opportunity to study

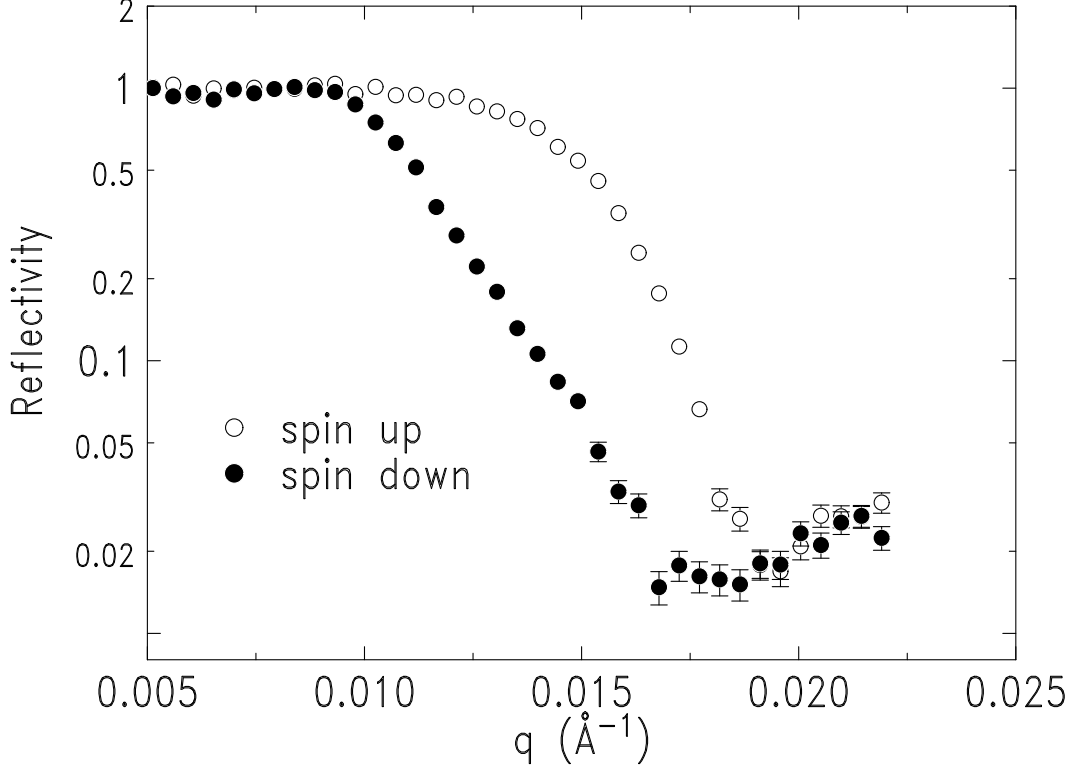


FIG. 3. SPNR from a 500 Å thick NiMnSb alloy was measured as a function of  $q$  at 1000 Oe, room temperature and atmosphere.

the density as well as distribution of the vortices in superconductor and allow to study the interaction, vortex-surface.

The magnetization in a *thin-film* superconductor at a field applied parallel to the surfaces depends on position perpendicular to the surface. That is described in Sec. 4.2 in detail. When one calculates SPNR from the superconductor, the magnetization could not be assumed as a constant within the superconducting film. Therefore, we have numerically solved Eq. (3.8), using a multi-sliced method which is described in Ch. 7.

### 3.2. Spin-polarized Neutron Reflectometry at MURR

The neutron reflectometer at the Missouri University Research Reactor (MURR), the Grazing Angle Neutron Spectroscopy (GANS) [33], uses a continuous beam of neutrons from the 10 MW reactor source. Figure 4 shows the schematic diagram of the GANS. After neutrons exit from the source, they travel through a pyrolytic graphite (PG-002) filter which suppress fast neutrons (short wavelength neutrons), and reflected from a HoPG graphite monochromator. The neutrons with wave length  $2.35 \text{ \AA}$  are obtained through Bragg diffraction from the monochromator. The reflected neutrons from the monochromator meet the first slit (rotary type  $\sim 0.47\text{mm}$  open) which is located just after the monochromator and most unwanted radiations, fast neutrons, slow neutrons, and gamma-ray are blocked at this point. And then neutrons go through the second slit (fixed slit  $\sim 0.5\text{mm}$  open) which controls the shape of beam cross section to symmetry (it is asymmetry for the upstream rotary slit) and is polarized by reflecting from a polarizing mirror which is a [Cr/Fe] multi-layered film on a glass plate. Once the neutrons are polarized, the spin direction would be maintained by a 10 Oe magnetic field in the beam path. Just after the polarizer a flipper, which consists of two crossed plate solenoids, sets the neutron spin direction up or down. Before the spin-polarized neutrons hit the sample surface, it will travel through a third slit (fixed slit,  $\sim 0.3\text{mm}$ ) which mainly determines the beam size and angular divergence of the incident beam at the sample position. The neutrons reflected by the sample surface travel through a second flipper which is identical to the first flipper and hit an analyzer which is

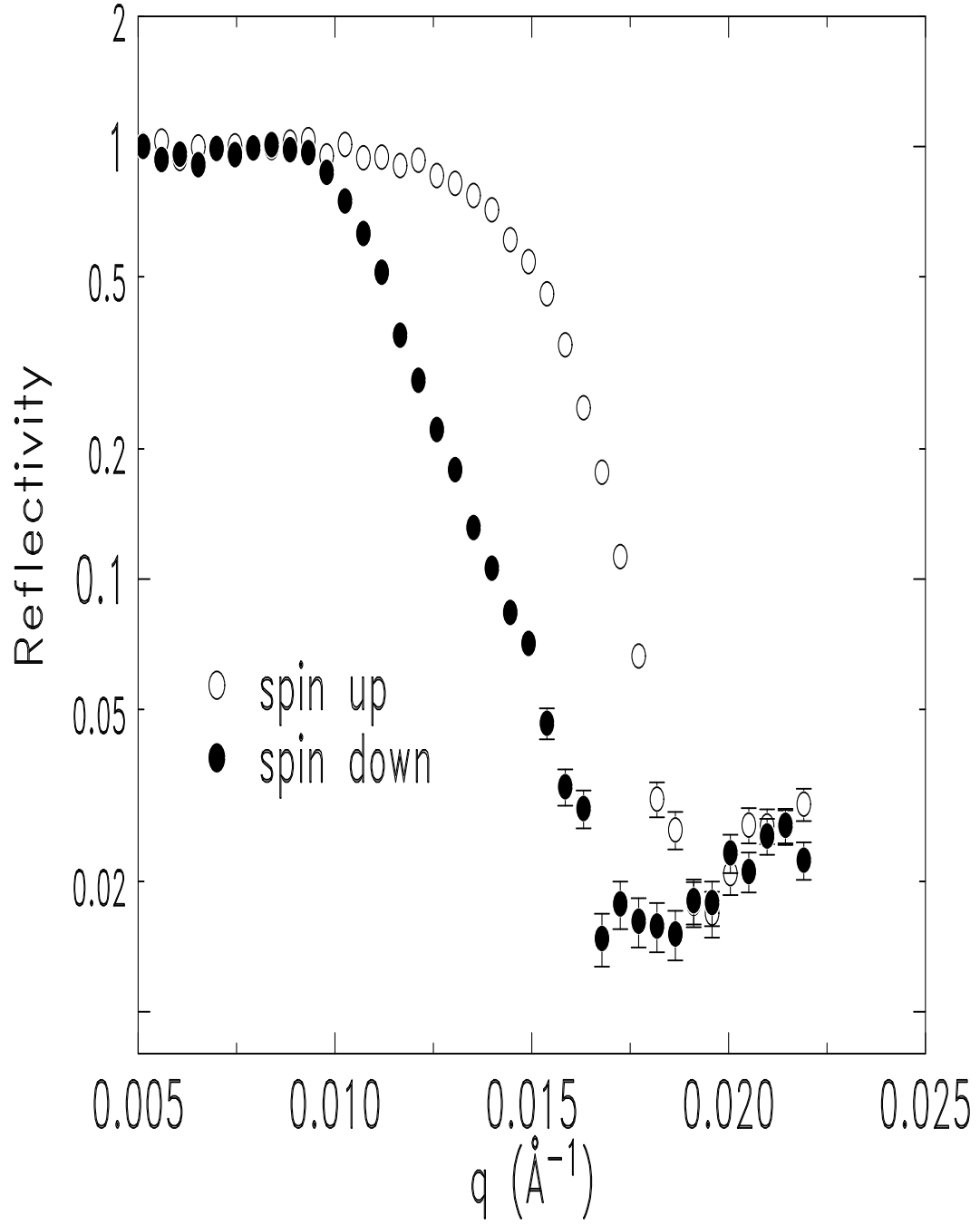


FIG. 4. Schematic diagram of the GANS reflectometry at MURR.



identical to the polarizer. Our experiments typically did not utilize the second flipper and analyzer. The final slit (fixed slit,  $\sim 1\text{mm}$ ) reduces the back ground and its size was chosen to accepted all of the beam reflected by the sample surface. And the neutrons were counted by a 1 / 2" Reuter-Stokes  $^3\text{He}$  filled gas proportional detector.

One could compare the GANS reflectometer with other spin-polarized neutron refelctometers in the world shown in Table 1.

TABLE I. Spin-Polarized Neutron Reflectometers in the World

Instrument	Source	Mode	Wavelength( $\text{\AA}$ )	Q-range( $\text{\AA}^{-1}$ )	Startup
POSY I	IPNS, Argonne	TOF	3.0 - 15.0	0 - 0.5	1984
CRISP	ISIS, Rutherford	TOF	0.5 - 13.0	0.006 - 1.0	1986
EVA	ILL, Grenoble	Reactor	5.5	0.0012 - 0.15	1987
ROG	IRI, Delft	TOF	1.0 - 15	0.006 - 1.75	1988
SPN	FLNP Dubna	TOF	0.7 10.0	0.003 - 0.2	1988
NG-7	NIST	Reactor	3.25 - 5.5	0.003 - 0.4	1990
SPEAR	LANSCE, Los Alamos	TOF	1 - 32	0.008 - 0.3	1991
V6	HMI, Berlin	Reactor			1992
NG-1	NIST	Reactor	4.75	0 - 2.2	1996
GANS	MURR	Reactor	2.35	0 - 0.4	1996
V14	HMI, Berlin	Reactor		0 - 1.5	1996

### 3.2.1. GANS Reflectometry Alignment

In this section, the alignments of slits, polarizer, analyzer and sample, the reflectometer centering to the beam, and flipper setting will be discussed. To set the first slit (rotary slit) located just after the monochromator, everything even the detector slit should be removed from the beam path. For the first slit, the opening slit size is proportional to the rotational angle,  $y \text{ (mm)} = 0.557 \times \theta \text{ (degree)} + 17.851$  where the slit is wide open at  $0^\circ$  and the beam is perfectly closed at  $-32^\circ$ . For obtaining in resolution, one will set the angle at the first slit  $\sim -31.2^\circ$  (0.47mm open). Once set the first slit, the beam profile (asymmetry shape) of the intensity cross section could be measured with a slit ( $< 0.15\text{mm}$ ) at the detector.

A second slit (0.5mm fixed slit) is located at the end of a collimator before a polarizer. The second slit (0.5mm fixed slit) should be placed at the strongest beam intensity position. To find the position of the strongest beam intensity position, one would play with a 0.5mm slit, horizontally moving the slit and counting the beam intensity without the detector slit. When the second slit is set, the cross section profile of the beam intensity should be symmetry. Then the polarizer would be aligned.

For aligning the polarizer, one will check if the supermirror surface is parallel to gravity by using a balancer. One could make the supermirror surface located in the middle of the beam and parallel to the beam by horizontally moving and rocking the supermirror without the detector slit. And then one will set the polarizer at

0.3° where it has the maximum polarization efficiency without losing neutrons very much. Now, the beam is polarized. The polarized beam intensity should be close to half of the main beam (before the beam polarized). One will set a guide field ( $> 10$  Oe) in the beam path to keep the neutron spin orientation.

The third slit (0.3 mm fixed slit) will be set now. With nothing in the beam path from the polarizer to the detector, one will find a horizontal position of the slit at which the beam intensity is maximum and then maximize the beam intensity by tilting the slit. One will do aligning the third slit at least twice with the same procedure. After set the horizontal position and tilt angle of the third slit, one will check if the slit is parallel to the beam by rocking the slit. After the third slit set, one will align the reflectometer because the beam going through the center of the rotational axis of the reflectometer is very important for the reflectivity measurements.

First it makes sure that the beam directly hit the detector with nothing in the beam path from the third slit to the detector. For the reflectometer alignment, an L-shaped arm which will hold a slit ( $< 0.3\text{mm}$ ) is necessary. The arm is screwed down on the top of the goniometer and holds a fixed slit. By  $\theta$ -rocking, one will find the beam location at upstream  $\theta_u$  and downstream  $\theta_d$ . The shortest distance  $\Delta x$  between the center of rotation and the beam is determined to,

$$\Delta x = L \times \sin\left(\frac{\theta_d - \theta_u}{2}\right) \dots\dots\dots (3.10)$$

where L is the arm length from the center of rotation to the slit. After the re-

flectometer moved by  $\Delta x$ , one will check the beam position again with the same procedure. After set the reflectometer, one will check the polarized beam angular divergence with a fixed slit ( $< 0.15$  mm) at the detector.

Next step, one will set the analyzer located on a detector arm. Setting the analyzer is the same to the setting procedure of the polarizer. However, after the analyzer half-cut the beam and set at  $0.3^\circ$ , the detector only should be shifted (without moving the detector arm) to pick up the reflected beam from the analyzer.

One will want to check the polarization efficiency of the beam before starting a SPNR measurement. After it makes sure the guide field in the beam path, one will set the flippers. At both sides of the flipper, upstream and downstream, the guide field should be uniform (vertically) and identical. The vertical component of the guide field will be  $\sim 30$  Oe at the flipper and its radial component should be less than  $1/3$  of the vertical field. The flipper generates magnetic field in two directions, vertically (for canceling the guide field in the flipper) and horizontally (for flipping the neutrons). One will maximize the flipper efficiency by changing a small step of applying current. The polarization efficiency is determined by the intensity ratio for spin-up neutrons (flipper off) and spin down neutrons (flipper on). That is described in Sec. 3.2.2 in detail.

A sample alignment for the neutron reflectivity studies is very different from x-ray because the absorption cross section for neutron is relatively much smaller than for x-ray. With a line beam, one will align a sample which has three freedoms:

the sample surface should be parallel (vertically and horizontally) to the beam and be in the middle of the beam. First one will find the sample position to the polarized beam. There are couple of ways to find the sample position to the beam. I will discuss two ways in this thesis. First, set the detector at the beam ( $2\theta = 0^\circ$ ) and do a sample translational scan. The neutron beam will mostly transmit through the sample. However, one will see a dent in the scan due to the beam reflected by the sample surface. If the dent does not show, then change the sample angle a little bit and try again. Once the dent shows up, fix the sample translation position near the dent and move  $2\theta$  to an angle below critical angle below which the beam is totally reflected by the surface. And find the beam reflected by the surface, using  $\theta$ -rocking and then maximize the reflected beam intensity by sample translational scan,  $\theta$ -rocking and  $\chi$ -rocking (to make the sample surface vertically parallel to the beam). This method is useful for a big sample because the dent could be easily found for a large amount of beam reflected by a big surface.

If a sample surface is small, the dent will be hard to be found. Then one could find the sample position to the polarized beam by using an extra plate which has a large neutron absorption cross section, such as Cd plate. A sample is mounted on a Cd plate which is well attached on a sample holder. The sample translational scan will show the position of Cd plate to the beam. Once one finds the Cd plate position, one could calculate the sample surface position with known sample thickness. Figure 5 shows a sample translational scan with a 2 mm thick substrate and 0.8 mm thick Cd plate. At (a) a Cd plate starts to cut the beam,

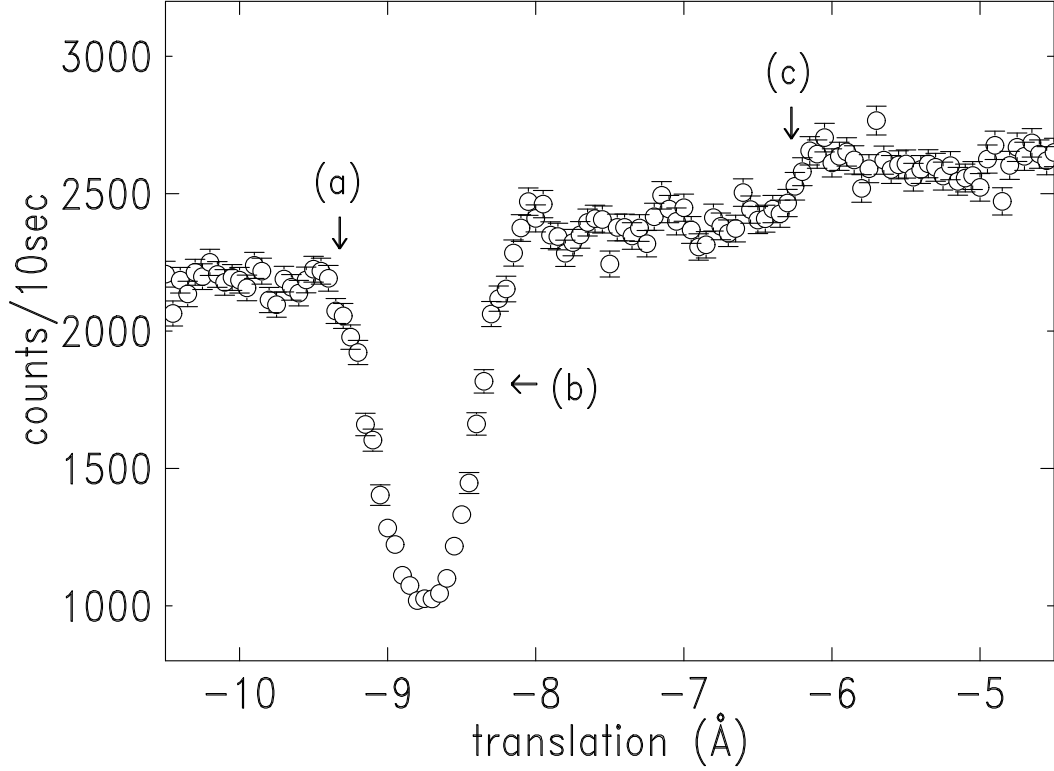


FIG. 5. Sample translation scan at  $2\theta = 0^\circ$  with a  $6000 \text{ \AA}$  thick  $\text{YBa}_2\text{Cu}_3\text{O}_{7-x}$  (2 mm thick  $\text{SrTiO}_3$  substrate) mounted on a 0.8 mm thick Cd plate.

at (b) the back side of the substrate mounted on the Cd plate is in the middle of the beam and at (c) the sample surface is in the middle of the beam. The distance from (b) to (c) is the substrate thickness.

However, if a Cd plate (sample surface) is not parallel to the beam, the calculated beam position will be different from the real beam position. To find a tilt angle of the Cd plate to the beam, one will scan the sample translations with a small step changing  $\theta$  and plot the Cd plate position as a function of  $\theta$ .  $\theta$  at the extremal value of the Cd plate is for the Cd plate closest parallel to the beam. After

set the sample translation position, move  $2\theta$  to an angle below a critical angle. And maximize the beam intensity reflected from the sample surface by rocking  $\theta$  and translation. Finally one will check if the sample surface is vertically parallel to the beam by rocking  $\chi$ .

### *3.2.2. Polarizer and polarization*

The polarizer and the analyzer at the GANS reflectometry are basically identical. Spin-up neutrons and spin down neutrons have a different critical angle due to the magnetic layers of the mirror, as described in Sec. 3.1. The polarizer was made of [Fe/Cr] multi-layer deposited on a glass plate by sputtering magnetron. Practically, the beam will be not perfectly polarized. The polarization efficiency of the beam is contributed by the efficiency of polarizer, the efficiency of flipper and a magnetic field which remains in the beam path.

One could determine the polarization of beam by using a polarizer, an analyzer and a flipper. The schematic diagram, Fig. 6 shows the side view of the arrangement at the GANS reflectometry. The polarizer efficiency is  $P_p$ , the analyzer efficiency is  $P_a$  and Flipper1 efficiency is  $P_f$ .

1. Between the polarizer and Flipper1 (in this case, Flipper2 is off), the intensity of the spin-up neutron beam is  $P_p$  and the intensity of spin down neutron beam is  $1 - P_p$ , assuming that the total intensity of reflected beam from the polarizer is 1.

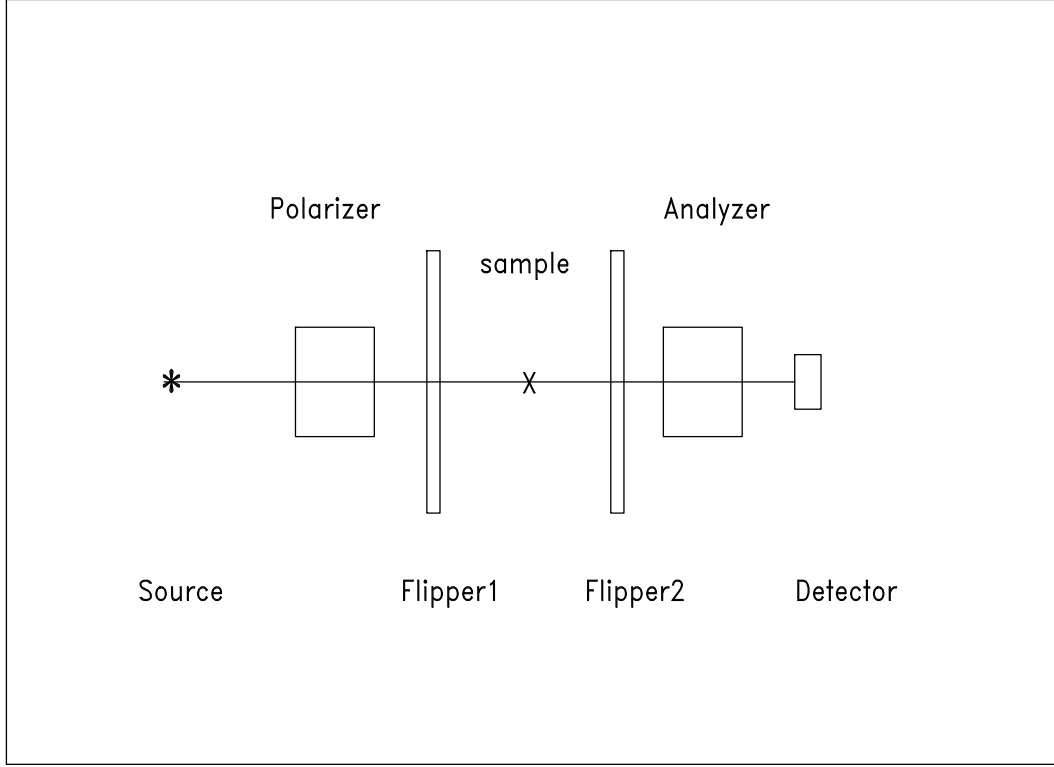


FIG. 6. Schematic diagram for the positions of the polarizer, analyzer, flippers at the GANS reflectometry.

2. Between Flipper1 and the analyzer, with Flipper1 turned off, the intensity of the spin-up neutron beam is  $P_p$  and the intensity of spin down neutron beam is  $1 - P_p$ . With Flipper1 turned on, the intensity of the spin-up neutron beam is  $P_p(1 - P_f) + (1 - P_p)P_f$  and the intensity of spin down neutron beam is  $(1 - P_p)(1 - P_f) + P_pP_f$ .

3. Between the analyzer and the detector, with Flipper1 turned off, the intensity of the spin-up neutron beam is  $\alpha P_p P_a + \alpha(1 - P_p)(1 - P_a)$  and the intensity of spin down neutron beam is  $\alpha(1 - P_p)P_a + \alpha P_p(1 - P_a)$  where  $\alpha$  is the total



intensity of the beam reflected by the analyzer. With Flipper1 turned on, the intensity of the spin-up neutron beam is  $(P_p + P_f - 2P_pP_f)\alpha P_a + (1 - P_p - P_f + 2P_pP_f)\alpha(1 - P_a)$  and the intensity of spin down neutron beam is  $(1 - P_p - P_f + 2P_pP_f)\alpha P_a + (P_p + P_f - 2P_pP_f)\alpha(1 - P_a)$ .

4. At the detector, the count ratio  $N$  for Flipper1 turned on and off will be

$$N = \frac{\text{counts}(\text{flipper on})}{\text{counts}(\text{flipper off})}$$

$$= \frac{1 - P_p - P_a + 2P_pP_a}{(P_p + P_f - 2P_pP_f)P_a + (1 - P_p - P_f + 2P_pP_f)(1 - P_a)} \dots\dots\dots (3.11)$$

One can assume that  $P_p$  (polarization efficiency of polarizer + demagnetization from the polarizer to Flipper1)  $\simeq P_a$  (polarization efficiency of polarizer + demagnetization from the analyzer to the detector) because the polarizer and the analyzer are identical. The efficiency of Flipper1 (Flipper1 efficiency + demagnetization from Flipper1 to the analyzer) is 1 because it is difficult to distinguish the polarizer and flipper efficiencies. Finally, the polarization efficiency  $P_p$  can be calculated with a given flipping ratio.

$$P_p = \frac{1 \pm \sqrt{1 - 2/(1 + N)}}{2} \dots\dots\dots (3.12)$$

where  $\pm$  is for the polarized and unpolarized neutrons.

Without an analyzer, the measured reflectivity from a sample with a flipper

turned on and off will be

$$\begin{aligned}
R_{\uparrow} &= P_p R_{++} + P_p R_{+-} + (1 - P_p) R_{--} + (1 - P_p) R_{-+} + Bg_{\uparrow} \\
&= P_p (R_{++} - R_{--}) + R_{--} + R_{-+} + Bg_{\uparrow} \\
R_{\downarrow} &= (P_p + P_f - 2P_p P_f)(R_{++} + R_{+-}) \\
&\quad + (1 - P_p - P_f + 2P_p P_f)(R_{--} + R_{-+}) + Bg_{\downarrow} \dots \dots \dots (3.13)
\end{aligned}$$

where  $Bg_{\uparrow}$  and  $Bg_{\downarrow}$  are background counts (including diffuse scattering) for the flipper turned on and off. Therefore the measured polarization is

$$\frac{R_{\uparrow} - R_{\downarrow}}{R_{\uparrow} + R_{\downarrow}} = \frac{(2P_p P_f - P_f)(R_{++} - R_{--})}{(2P_p + P_f - 2P_p P_f)(R_{++} - R_{--}) + 2R_{-+} + 2Bg} \dots \dots \dots (3.14)$$

where assumed  $Bg_{\uparrow} = Bg_{\downarrow} = Bg$  and  $R_{+-} = R_{-+}$ . For  $P_f = 1$ , the polarization will be

$$\frac{R_{\uparrow} - R_{\downarrow}}{R_{\uparrow} + R_{\downarrow}} = \frac{(2P_p - 1)(R_{++} - R_{--})}{(R_{++} + R_{--}) + 2R_{-+} + 2Bg} \dots \dots \dots (3.15)$$

As applied field is parallel to the film surface and specular reflectivities are measured, the polarization can be described to

$$\frac{R_{\uparrow} - R_{\downarrow}}{R_{\uparrow} + R_{\downarrow}} = \frac{(2P_p - 1)(R_{++} - R_{--})}{(R_{++} + R_{--})} \dots \dots \dots (3.16)$$

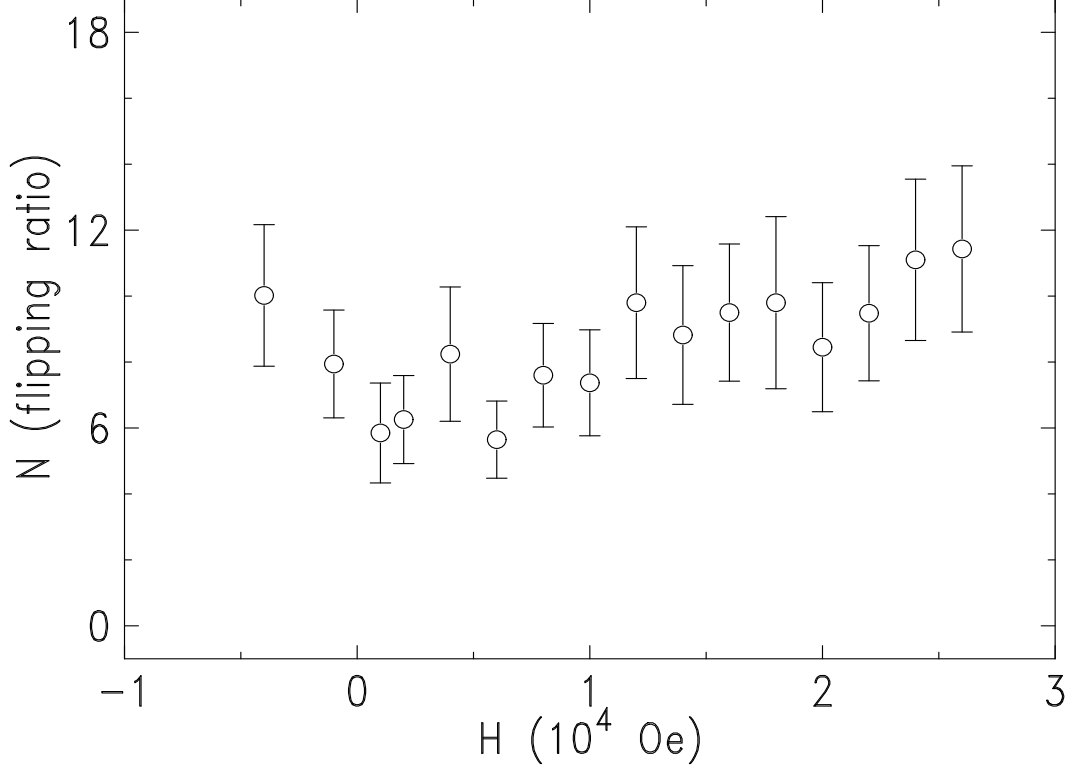


FIG. 7. Flipping ratio,  $\text{counts(Flipper1 off)} / \text{counts(Flipper1 on)}$  was measured as a function of applied field at room temperature.

For the SPNR measurements with using a polarizer and an analyzer (Flipper1 and Flipper2 will be necessary), one could figure out the flipping ratio,  $(R_{\uparrow} - R_{\downarrow}) / (R_{\uparrow} + R_{\downarrow})$  with the same idea described above.

Figure 7 shows the flipping ratio as a function of applied field. For the measurement, the polarizer, Flipper1 and a 500 Å thick NiMnSb alloy as an analyzer mounted in a superconducting split-coil magnetic cryostat were used. The reason why we have mounted the soft magnetic film in the superconducting magnet without using the analyzer is that we want to know the flipping ratio at the sample

position in the cryostat as a function of applied field. The magnetization of the film saturates at  $\sim 100$  Oe. SPNR from the film is shown in Fig. 3. The spin-up and spin down neutrons reflected from the film were counted at  $q \simeq 0.013 \text{ \AA}^{-1}$ ,  $\theta = 0.14^\circ$ .

### 3.2.3. Resolution Correction in Small Angle Reflectivity

The resolution for reflectivity is determined by instrumental limits (wave length spread, angular divergence) and sample characteristics (surface flatness for small angle, crystal mosaicity for high angle reflectivity). One could independently determine the angular divergence,  $\Delta\theta$ , and wave length spread,  $\Delta\lambda$ .  $\Delta\theta$  could be determined by measuring the broadening of the beam reflected by the sample surface at an angle below the critical angle.  $\Delta\lambda$  could be determined by measuring a Bragg diffraction from a known crystal at the sample position.  $\Delta\lambda/\lambda$  of the GANS at MURR 1.9 % for  $\lambda = 2.35 \text{ \AA}$  [33] was determined by measuring the broadening of the Si(111) Bragg peak.

With given  $\Delta\theta$  and  $\Delta\lambda$ , the resolution for small angle reflectivity can be calculated to,

$$\frac{\Delta q}{q} = \sqrt{\left(\frac{\Delta\lambda}{\lambda}\right)^2 + \left(\frac{\Delta\theta}{\tan\theta}\right)^2} \dots\dots\dots (3.17)$$

Once the resolution,  $\Delta q$  is known, the measured reflectivity,  $\bar{R}(q)$  can be compared with a theoretical reflectivity model calculation  $R(q')$  [44] using the

resolution correction,

$$\bar{R}(q) = \int_{-\infty}^{\infty} R(q')W(q' - q)dq' \dots\dots\dots(3.18)$$

where W is a normalized weight function. The reflectivity could be numerically integrated.

However, practically one would not integrate the reflectivity over whole q' range because the tail of the beam does not contribute to the reflectivity very much. Thus the integration for the reflectivity would be calculated within a certain q' range. The q' range for the integration could be determined at the point where the reflectivity difference is negligible with changing the q' range.

Assuming a Gaussian distribution of beam intensity in a beam cross section, the reflectivity is Gaussian convoluted (defining FWHM  $\equiv \Delta q$  where FWHM is the broadening of the beam reflected by the sample surface),

$$\bar{R}(q) = \frac{1}{N} \int_{q-\Delta q/2}^{q+\Delta q/2} R(q')e^{-4\ln 2(q'-q)^2/\Delta q^2} dq' \dots\dots\dots(3.19)$$

where N is a normalization factor and  $N = \Delta q \sqrt{\pi} \operatorname{erf}(\sqrt{4\ln 2}/2) / \sqrt{4\ln 2}$ , where  $\operatorname{erf}()$  is the error integral. Figure 8 shows the reflectivity with a Gaussian convolution.

For the Gaussian convolution in Eq. (3.19), the reflectivity was integrated over the q' range from  $q - \Delta q / 2$  to  $q + \Delta q / 2$  and the tails of the beam

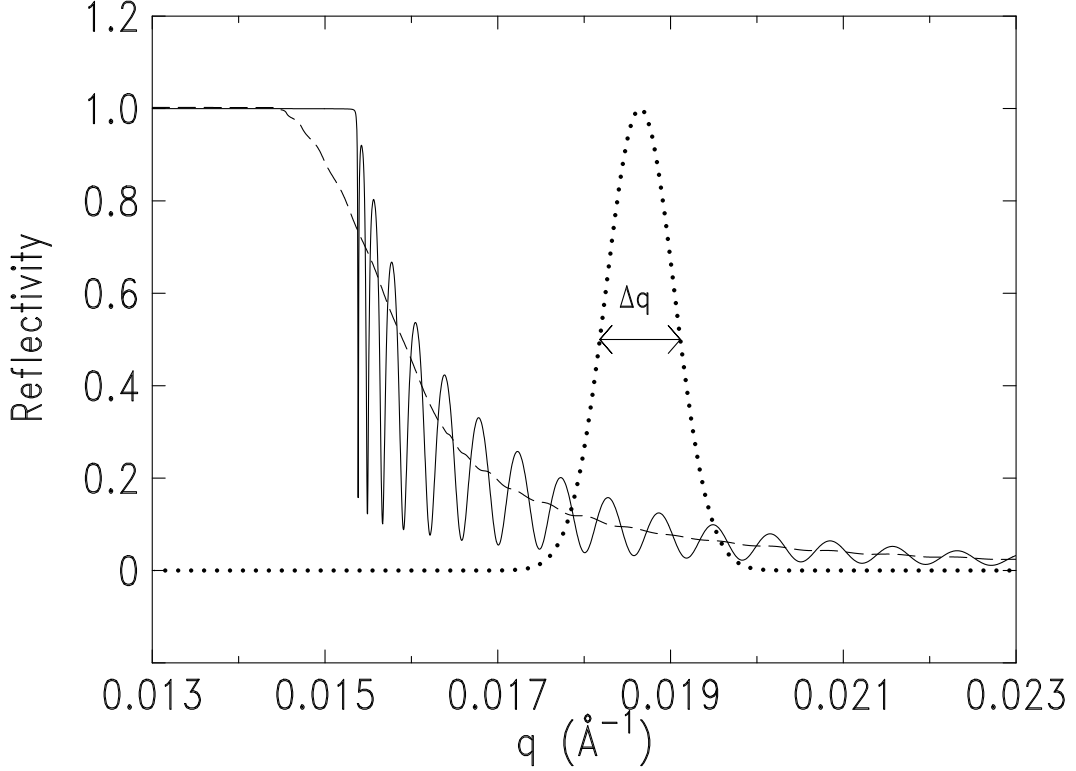


FIG. 8. Solid line is calculated reflectivity from a 6000 Å YBCO /SrTiO<sub>3</sub> with no surface roughness and dashed line is a Gaussian convoluted reflectivity with a Gaussian beam profile(dotted line).

were disregarded. However frequently the tails of beam will be needed in the reflectivity calculation, particularly, for polarization. Figure 9 shows the calculation of polarization on a 6000 Å thick YBa<sub>2</sub>Cu<sub>3</sub>O<sub>7-x</sub> (YBCO) superconducting film with  $\lambda_L$  1400 Å and applied field 300 Oe. The dotted line is the Gaussian convoluted polarization using the beam within  $\Delta q \simeq 0.002 \text{ Å}^{-1}$ , the dashed line with using the beam within  $2\Delta q$  and the solid line with using the beam within  $4\Delta q$ . Figure 9 shows that polarization is considerably sensitive to the truncation error of the

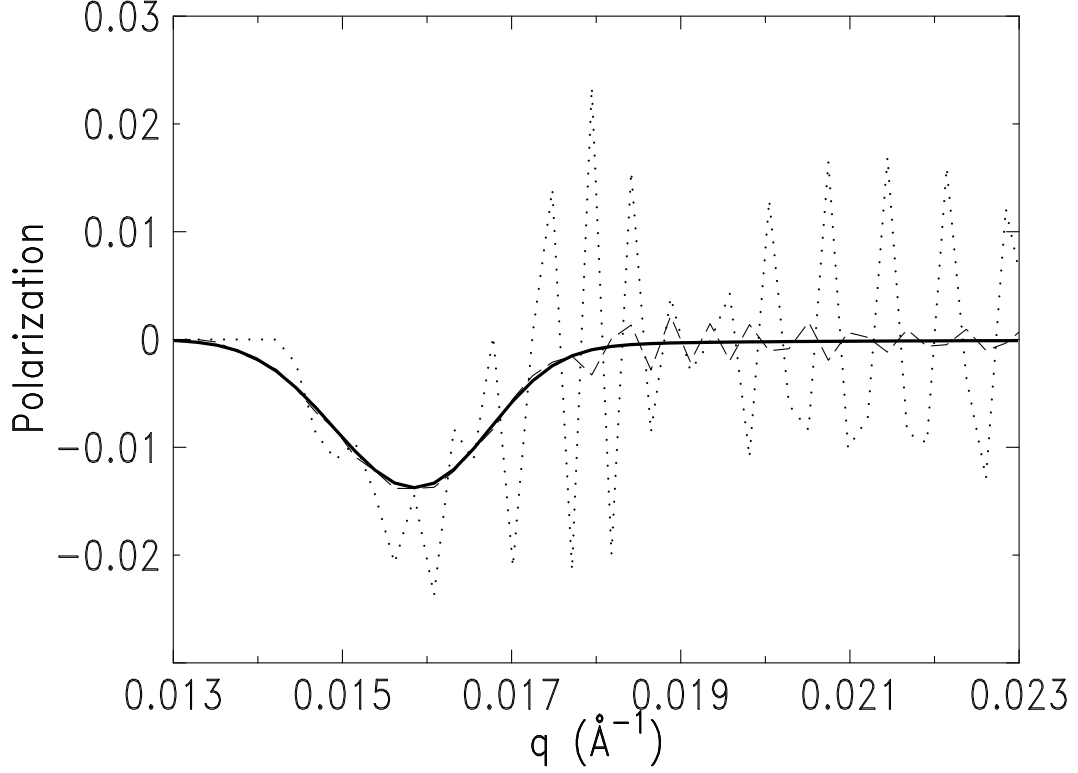


FIG. 9. Calculation for a Gaussian convoluted polarization of a 6000 Å thick YBCO /SrTiO<sub>3</sub> with  $H = 300$  Oe and  $\lambda_L = 1400$  Å with assuming different beam cuts,  $\Delta q$  (dotted line),  $2\Delta q$  (dashed line) and  $4\Delta q$  (solid line).

beam. For these calculations, the Eq. (3.19) is modified to,

$$\bar{R}(q) = \frac{1}{N} \int_{q-M\Delta q/2}^{q+M\Delta q/2} R(q') e^{-4ln2(q'-q)^2/\Delta q^2} dq' \dots\dots\dots (3.20)$$

where  $N$  is a normalization factor,  $\Delta q = \sqrt{\pi} \operatorname{erf}(M\sqrt{4ln2}/2) / \sqrt{4ln2}$  and  $M$  is a constant to control the resolution window without disturbing the beam intensity profile. In Fig. 9,  $M$  was 1 (dotted line), 2 (dashed line) and 4 (solid line).





## 4. ONE-DIMENSIONAL MAGNETIZATION IN SUPERCONDUCTOR

### 4.1. Critical Current Model

As a type-II superconductor is placed in a high magnetic field, vortices will enter the superconductor. For a bulk superconductor, the London penetration at surface can be ignored. Assuming a strong pinning bulk superconductor, vortices will enter from the surface and stay near surface at a small field. As the field increased, the first vortices will be pushed toward the middle of the superconductor by the second vortices. Charles Bean modeled the local magnetic field in the superconductor with the vortices which satisfies the critical current density [34].

$$\left| \nabla \times \vec{B}(\vec{r}) \right| = J_c \dots \dots \dots (4.1)$$

where  $J_c$  is the critical current density which can be determined by the interaction of bulk pinning centers and vortices, as described in Sec. 2.3. Near  $H_{c1}$ ,  $J_c$  will be near a constant without depending on applied field meanwhile at a higher field,  $J_c$  might be different, as applied field changing. This model shows that the local magnetic field in the superconductor is linearly decayed from surface.

For a superconducting slab, the local magnetic field which satisfies the boundary condition,  $B\hat{x} = H\hat{x}$ , can be calculated to,

$$B(z)\hat{x} = J_c(z - t/2)\hat{x} + H\hat{x} \dots\dots\dots (4.2)$$

where  $t$  is the thickness of a slab. Eq. (4.2) is valid for only  $H \leq tJ_c / 2$  and ascending field. At other fields, one can calculate the local magnetic field by using Eq. (4.1) with the boundary condition. The top in Fig. 10 shows a typical hysteresis loop predicted by the critical current model with a given critical current. The bottom figures show a local magnetic field profile which is corresponding to the applied field shown at the top. It shows that the vortices enter the superconductor from the surfaces for increasing field and disappear from the surfaces as the applied field decreased.

By measuring magnetization of a superconductor as a function of applied field, one can determine a critical current density from the plateaus of a hysteresis loop.

$$J_c = \frac{2\Delta M}{t} \dots\dots\dots (4.3)$$

where  $\Delta M$  is the magnetization difference between the plateaus. And also if  $J_c$  is known, measuring by other techniques, one can predict magnetization as well as spatially varying magnetization of the superconductor at a given field.

The critical current model is suitable to briefly predict the spatially varying magnetization and  $J_c$  of a hard bulk superconductor. However for a soft bulk

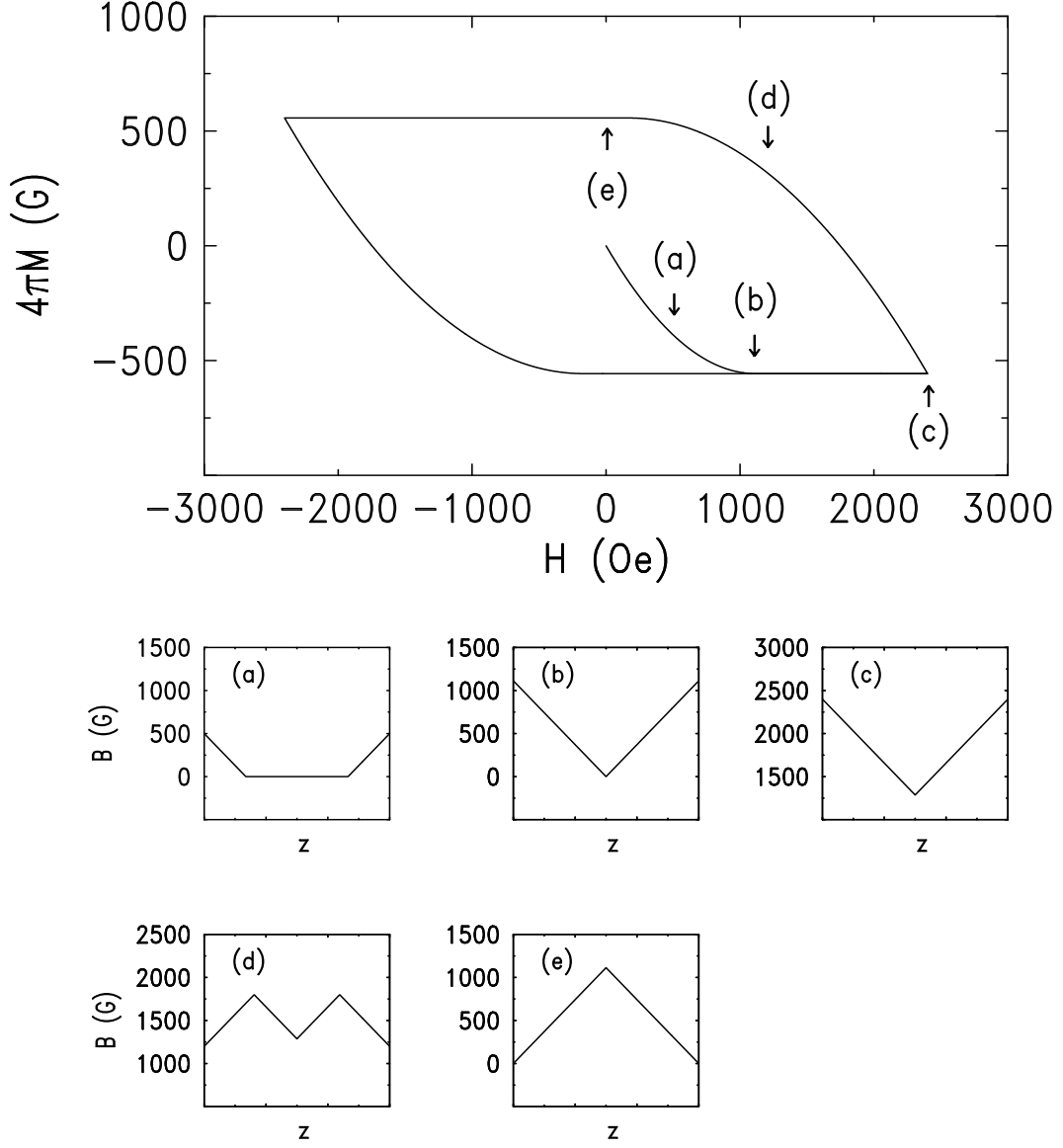


FIG. 10. Magnetization in a superconducting slab calculated by using Bean model is shown at top and the bottom figures shows the local magnetic field profiles which are corresponding to the positions indicated by arrows in top.

superconductor and a thin film superconductor, this model might not be applicable. In a soft bulk superconductor of which the interaction of vortex and pinning centers is not strong, one can not expect an irreversible hysteresis loop in magnetization

measurements because the vortices will exit as applied field decreased. For a thin film with the geometry of applied field perpendicular to the surface, vortices will not come into the superconductor from the edges. They will pierce the film as the applied field is above a certain field. Thus one can not expect that vortices will move from the edges to the middle of film. As a small field (Meissner region) applied parallel to the surface, the local magnetic field which is exponentially decayed can be predicted by the London equation [5] and at a higher field the interaction of vortex and surface should not be ignored [20–24]. In the following section, I will introduce an exact solution of one-dimensional spatially varying magnetization in a thin superconducting film with the geometry where the applied field is parallel to the surface.

#### 4.2. Exact Solution of 1-D Magnetization with Vortices in Film

As a superconductor placed at a magnetic field, the spatially varying magnetization in the superconductor is contributed by the London penetration at surface and vortices. The local magnetic field in superconductor is governed by a London equation. With a single vortex, the London equation [5] is

$$\vec{B} + \lambda_L^2 \nabla \times \nabla \times \vec{B} = \Phi_o \delta^2(\vec{r} - \vec{r}_o) \dots \dots \dots (4.4)$$

where  $\Phi_o = ch / 2e$  is the vortex flux quantum,  $2.0679 \times 10^9 Oe\text{\AA}^2$  and  $\delta^2(\vec{r})$  is a two dimensional delta function. Assuming a superconducting thin slab and applied

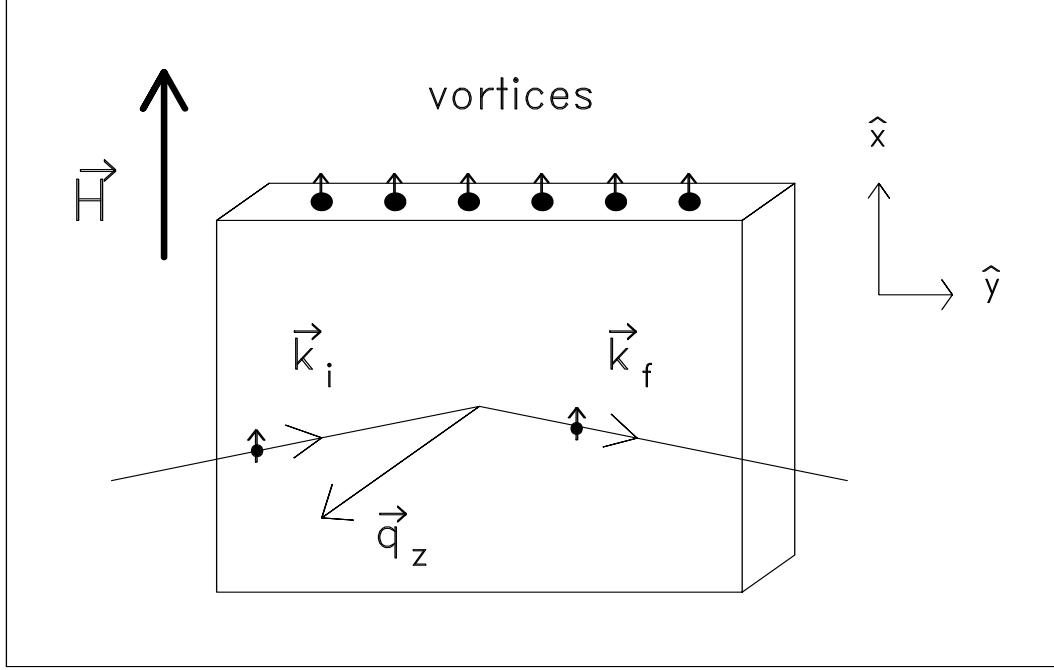


FIG. 11. Schematic diagram shows the geometry of the vortices and spin-polarized neutron reflectivity.

field parallel to the surfaces shown in Fig. 11, the local magnetic field near the surfaces is exponentially decayed without including the vortex contribution. Therefore, the magnetic field,  $\vec{B}_L$ , is

$$\vec{B}_L = Ce^{-\frac{z}{\lambda_L}} + De^{\frac{z}{\lambda_L}} \dots \dots \dots (4.5)$$

where C and D are the constants which will be determined by the boundary condition,  $\vec{B} = H\hat{x}$  at the surfaces. In the superconductor, the magnetic field due to vortices can also be known by solving a London equation [5]. Assuming a single vortex running parallel to  $x$ -axis and placed in a uniform, homogeneous and boundaryless superconductor, the magnetic field,  $\vec{B}_V$ , is

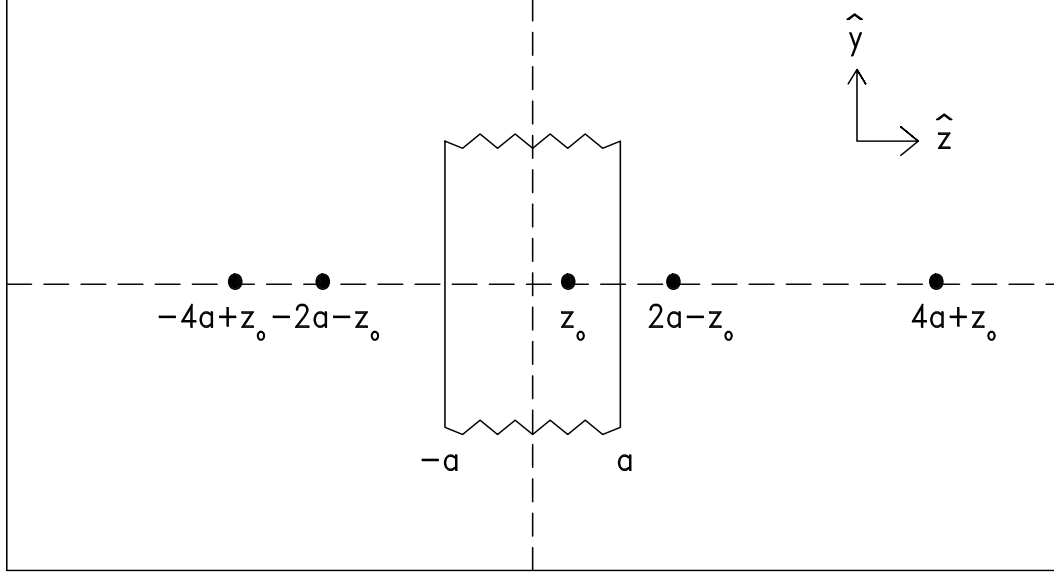


FIG. 12. Schematic diagram shows the vortex and its image vortices of which contribution to the local magnetic field at the surfaces vanishes.

$$\vec{B}_V = \frac{\Phi_o}{2\pi\lambda_L^2} K_0\left(\frac{\sqrt{(z - z_o)^2 + (y - y_o)^2}}{\lambda_L}\right) \hat{x} \dots\dots\dots (4.6)$$

where  $K_0(|\vec{r}|)$  is the modified Bessel function of second kind of order 0 and the center of the vortex is located at  $(z_o\hat{z}, y_o\hat{y})$ . Once a vortex enters a superconductor, the contribution of the vortex to the local magnetic field at the surface vanishes because of the image vortices. Figure 12 shows the vortex and its image vortices.

The local magnetic field due to the vortex in a film can be described to,

$$\vec{B}_V = \frac{\Phi_o}{2\pi\lambda_L^2} \sum_{n=-\infty}^{n=\infty} (-1)^{|n|} K_0\left(\frac{|(z - 2na - (-1)^{|n|}z')|}{\lambda_L}\right) \dots\dots\dots (4.7)$$

where  $n = 0$  is for the real vortex and the other terms are due to its images. The local magnetic field by the London penetration at the surfaces will be

$$\vec{B}_L = H \frac{\cosh(z/\lambda_L)}{\cosh(a/\lambda_L)} \hat{x} \dots \dots \dots (4.8)$$

The magnetic field in a superconducting slab with a single vortex can be obtained by simply adding the two equations, (4.7) and (4.8) because both satisfy the boundary condition.

For  $H > H_{c1}$ , many vortices would enter a superconductor. The London equation with  $N_V$  vortices will be

$$\vec{B} + \lambda_L^2 \nabla \times \nabla \times \vec{B} = \vec{\Phi}_o \sum_{k=1}^{k=N_V} \delta^2(\vec{r} - \vec{r}_k) \dots \dots \dots (4.9)$$

Considering the boundary condition, the magnetic field due to the London penetration at the surfaces is the same to Eq. (4.8) because the contribution of each vortex to the magnetization at the surfaces is zero. The magnetic field due to  $N_V$  vortices is

$$\vec{B}_V = \frac{\vec{\Phi}_o}{2\pi\lambda_L^2} \sum_{k=1}^{k=N_V} \sum_{n=-\infty}^{n=\infty} (-1)^{|n|} K_0 \left( \frac{\sqrt{(z - 2na - (-1)^{|n|}z_k)^2 + (y - y_k)^2}}{\lambda_L} \right) \quad (4.10)$$

where the  $k^{th}$  vortex is at  $(z_k \hat{z}, y_k \hat{y})$ .

Assuming a row of the vortices along  $y$ -axis,  $(z' \hat{z}, y_k \hat{y})$ , one will average the magnetic field over  $y$ -direction because of the specular reflectivity condition

which reflectivity gives a one dimensional optical potential perpendicular to the scattering surface, as shown in Fig. 11. One can assume that the vortices are identical because the slab length in  $y$ -direction is infinite, compared with a London penetration depth and the vortices sit in a line along  $y$ -direction. Using  $\int_{-\infty}^{\infty} K_0(\sqrt{(a^2 + x^2)}/b)dx = \pi b e^{-|a|/b}$  for  $b > 0$  [35] and defining the average distance between vortices in  $y$ -direction,  $d_v \equiv L/N_V$  where  $L$  is the lateral sample length, one dimensional spatially varying magnetic field with  $N_V$  vortices in a superconducting film is calculated to,

$$\begin{aligned} \vec{B} = \vec{H} \frac{\cosh(\frac{z}{\lambda_L})}{\cosh(\frac{t}{2\lambda_L})} \\ + \frac{\vec{\Phi}_o}{2d_v\lambda_L} \left\{ e^{-\frac{|z-z'|}{\lambda_L}} - e^{\frac{z-t/2}{\lambda_L}} \frac{\sinh(\frac{z'+t/2}{\lambda_L})}{\sinh(\frac{t}{\lambda_L})} + e^{-(\frac{z+t/2}{\lambda_L})} \frac{\sinh(\frac{z'-t/2}{\lambda_L})}{\sinh(\frac{t}{\lambda_L})} \right\} \dots\dots\dots (4.11) \end{aligned}$$

where  $t$  is film thickness and the cores of vortices are at  $z'$ . The last two terms are from the image vortices. As the thickness of the slab is infinite, the last two terms vanishes. Also as the core of vortex moves to the surfaces, the vortex contribution to the field vanishes.

The vortex distribution would be determined by the interactions of vortices discussed in Ch. 2. With a given distribution of vortices, the one dimensional spatially varying magnetization can be calculated to,

$$\vec{B} = \vec{H} \frac{\cosh(\frac{z}{\lambda_L})}{\cosh(\frac{t}{2\lambda_L})} + \frac{\vec{\Phi}_o}{2d_v\lambda_L} \int_{-t/2}^{t/2} \left\{ e^{-\frac{|z-z'|}{\lambda_L}} \right.$$



$$\left. -e^{\frac{z-2/t}{\lambda_L}} \frac{\sinh(\frac{z'+t/2}{\lambda_L})}{\sinh(\frac{t}{\lambda_L})} + e^{-(\frac{z+t/2}{\lambda_L})} \frac{\sinh(\frac{z'-t/2}{\lambda_L})}{\sinh(\frac{t}{\lambda_L})} \right\} D(z') dz' \dots\dots\dots (4.12)$$

where  $D(z')$  is a normalized distribution function of vortices,  $1 = \int_{-t/2}^{t/2} D(z') dz'$ . It shows that the one-dimensional spatially varying magnetic field is independent from the anisotropic problem.

Here I will introduce three cases of vortex distributions, in rows, uniform distribution and a Gaussian distribution. For vortices in a line, the distribution function is  $D(z') = \delta(z')$ . The magnetic field in a film with vortices in a single row will be the same to Eq. (4.11). If the vortices stay in several lines, the distribution function will be  $D(z') = [\delta(z_1) + \delta(z_2) + \delta(z_3) + \dots] / n$  where  $n$  is the number of vortex rows. Each vortex satisfies the boundary condition and also each line of vortices satisfies the boundary condition.

If the vortices are uniformly distributed through whole film, the distribution function is  $D(z') = 1 / t$ . The local magnetic field will be calculated using Eq. (4.12).

$$\vec{B} = \vec{H} \frac{\cosh(\frac{z}{\lambda_L})}{\cosh(\frac{t}{2\lambda_L})} + \frac{\vec{\Phi}_o}{2d_v \lambda_L} \left\{ 1 - \frac{\cosh(\frac{z-t/2}{\lambda_L})}{\cosh(\frac{t}{2\lambda_L})} \right\} \dots\dots\dots (4.13)$$

It shows that the spatial magnetic field due to vortices is the same shape as the magnetic field from London penetration at the surfaces.

When a Gaussian distribution of vortices is assumed, the distribution of vortices will be  $D(z') = N e^{-4 \ln 2 z'^2 / \Omega^2}$  where  $N$  is a normalization factor and  $\Omega$  is a

full width at half maximum. The normalization factor can be found by integrating the Gaussian function within the film.

$$\frac{1}{N} = \int_{-t/2}^{t/2} e^{-4\ln 2 z'^2 / \Omega^2} dz' = \Omega \sqrt{\frac{\pi}{4\ln 2}} \operatorname{erf} \left( \frac{t\sqrt{4\ln 2}}{2\Omega} \right) \dots\dots\dots (4.14)$$

where  $\operatorname{erf}()$  is an error integral and assumed that the center of the Gaussian distribution is in the middle line of a film. With the normalization factor and the Gaussian distribution function, one could calculate a spatially varying magnetic field, using Eq. (4.12).

$$\begin{aligned} \vec{B} = & \left\{ \vec{H} - \frac{\vec{\Phi}_o}{4\lambda_L d_v} \frac{e^{-t/2\lambda_L + \Omega^2/16\ln 2\lambda_L^2}}{\operatorname{erf}(t\sqrt{4\ln 2}/2\Omega)} \times \left| \operatorname{erf} \left( \frac{\sqrt{4\ln 2}}{\Omega} \left[ \frac{t}{2} - \frac{\Omega^2}{8\ln 2\lambda_L} \right] \right) \right. \right. \\ & \left. \left. + \operatorname{erf} \left( \frac{\sqrt{4\ln 2}}{\Omega} \left[ \frac{t}{2} + \frac{\Omega^2}{8\ln 2\lambda_L} \right] \right) \right| \right\} \times \frac{\cosh(z/\lambda_L)}{\cosh(t/2\lambda_L)} \\ & + \frac{\vec{\Phi}_o}{4\lambda_L d_v \operatorname{erf}(t\sqrt{4\ln 2}/2\Omega)} \left\{ e^{-z/\lambda_L + \Omega^2/16\ln 2\lambda_L^2} \left| -\operatorname{erf} \left( \frac{\sqrt{4\ln 2}}{\Omega} \left[ t - z + \frac{\Omega^2}{8\ln 2\lambda_L} \right] \right) \right. \right. \\ & \left. \left. + \operatorname{erf} \left( \frac{\sqrt{4\ln 2}}{\Omega} \left[ \frac{t}{2} + \frac{\Omega^2}{8\ln 2\lambda_L} \right] \right) \right| + e^{z/\lambda_L + \Omega^2/16\ln 2\lambda_L^2} \right. \\ & \left. \times \left| \operatorname{erf} \left( \frac{\sqrt{4\ln 2}}{\Omega} \left[ t - z - \frac{\Omega^2}{8\ln 2\lambda_L} \right] \right) + \operatorname{erf} \left( \frac{\sqrt{4\ln 2}}{\Omega} \left[ \frac{t}{2} + \frac{\Omega^2}{8\ln 2\lambda_L} \right] \right) \right| \right\}. \quad (4.15) \end{aligned}$$

Using Eq. (4.15), the local magnetic field calculated with different vortex distributions,  $\Omega = 0 \text{ \AA}$ ,  $2000 \text{ \AA}$  and  $20000 \text{ \AA}$  is shown in Fig. 13. For the calculations,  $\lambda_L$   $1400 \text{ \AA}$ , film thickness  $6000 \text{ \AA}$ , applied field  $2500 \text{ Oe}$  and vortex density

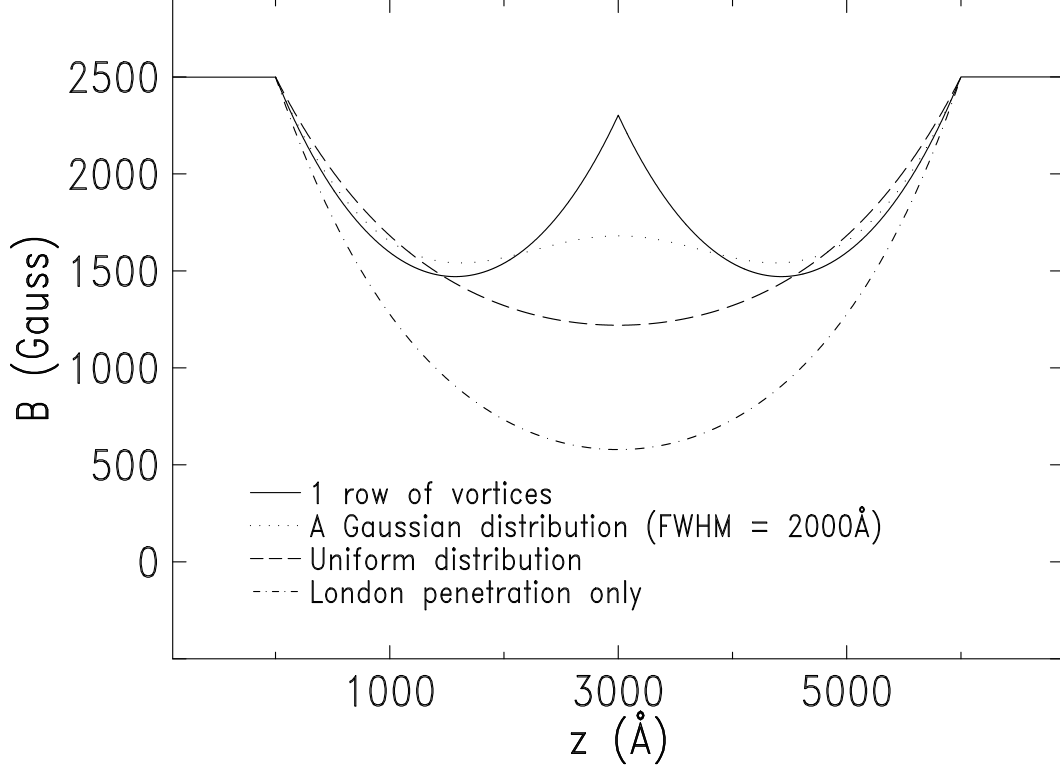


FIG. 13. Magnetic fields are calculated with different distribution of vortices, assuming that  $\lambda_L = 1400 \text{ \AA}$  film thickness =  $6000 \text{ \AA}$ ,  $H = 2500 \text{ Oe}$  and vortex density =  $40 \text{ per } \mu m^2$ .

$40 \text{ per } \mu m^2$  were assumed. The calculation for  $\Omega = 0 \text{ \AA}$  is the same to the vortices located in the middle line of the film, as described in Eq. (4.11). And the calculation for  $\Omega = 20000 \text{ \AA}$  is basically same to a uniform distribution of vortices, as described in Eq. (4.13). Figure 13 obviously shows that the distribution of vortices as well as the vortex density affects the spatially varying magnetization and average magnetization in a superconducting film.

The density of vortices in a superconductor could be found by using Eq. (4.12). It could be assumed that an averaged single vortex exists within  $d_v \times t$

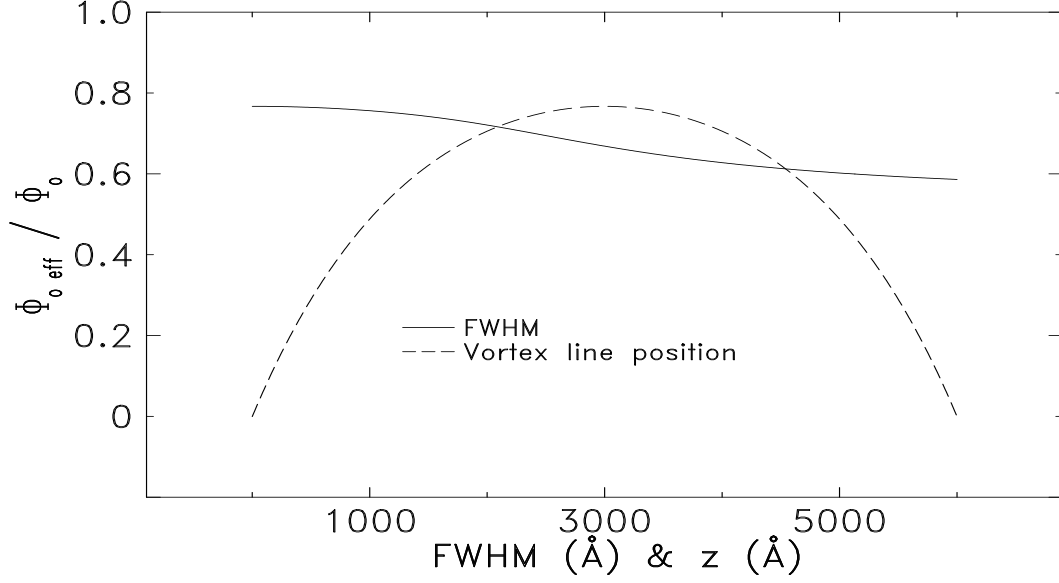


FIG. 14. Effective flux quantum is calculated as a function of vortex position (dashed line) and FWHM of a Gaussian distribution of vortices (solid line), assuming that film thickness 6000 Å and  $\lambda_L$  1400 Å.

area. Then the density of vortices will be described as

$$n_o = \frac{1}{td_v} \dots \dots \dots (4.16)$$

However, the flux quantum of vortex in a slab is not  $\Phi_o$  because of the image vortices. If the distribution of vortices is given, one can calculate the effective flux quantum of vortex.

$$\Phi_{eff} = \frac{\Phi_o}{2\lambda_L} \int_{-t/2}^{t/2} \int_{-t/2}^{t/2} \left\{ e^{-\frac{|z-z'|}{\lambda_L}} - e^{\frac{z-t/2}{\lambda_L}} \frac{\sinh(\frac{z'+t/2}{\lambda_L})}{\sinh(\frac{t}{\lambda_L})} \right. \\ \left. + e^{-\frac{(z+t/2)}{\lambda_L}} \frac{\sinh(\frac{z'-t/2}{\lambda_L})}{\sinh(\frac{t}{\lambda_L})} \right\} D(z') dz' dz \dots \dots \dots (4.17)$$

The effective flux quantum depends on the distribution of vortices, film thickness and London penetration depth. As the thickness of the slab is infinite, the last two term will be vanished and  $\Phi_{eff}$  approaches to  $\Phi_o$ . As the vortex approaches to surface, the effective flux quantum of vortex will be vanished. Figure 14 shows the effective flux quantum. Assuming that film thickness = 6000 Å and London penetration depth = 1400 Å, the solid line is the effective flux as a function of the vortex position and the dashed line is the effective flux as a function of FWHM, assuming a Gaussian probability of vortex position.

The average magnetization of a superconducting film can be calculated if the density and distribution of vortices is given.

$$4\pi\bar{M} = H \left\{ \frac{2\lambda_L}{t} \tanh \left( \frac{t}{2\lambda_L} \right) - 1 \right\} + n_v \Phi_{eff} \dots\dots\dots (4.18)$$

For a bulk superconductor,  $\Phi_{eff}$  goes to  $\Phi_o$  and the averaged London penetration contribution to magnetization can be ignored.

It is clear that the presence of vortices and their distribution will affect the spatially varying magnetization. It will affect the spin-polarized neutron reflectivity which is sensitive to the spatial gradient of neutron scattering density. Using Eq. (4.9), one can calculate the neutron scattering density profile with a given spatially varying magnetization.

$$V = V_n(\vec{r}) + V_m(\vec{r}) = \frac{2\pi\hbar^2}{m_n} (N_n < b_c > \pm 2.312 \times 10^{-10} 4\pi M(z)) \dots\dots\dots (4.19)$$

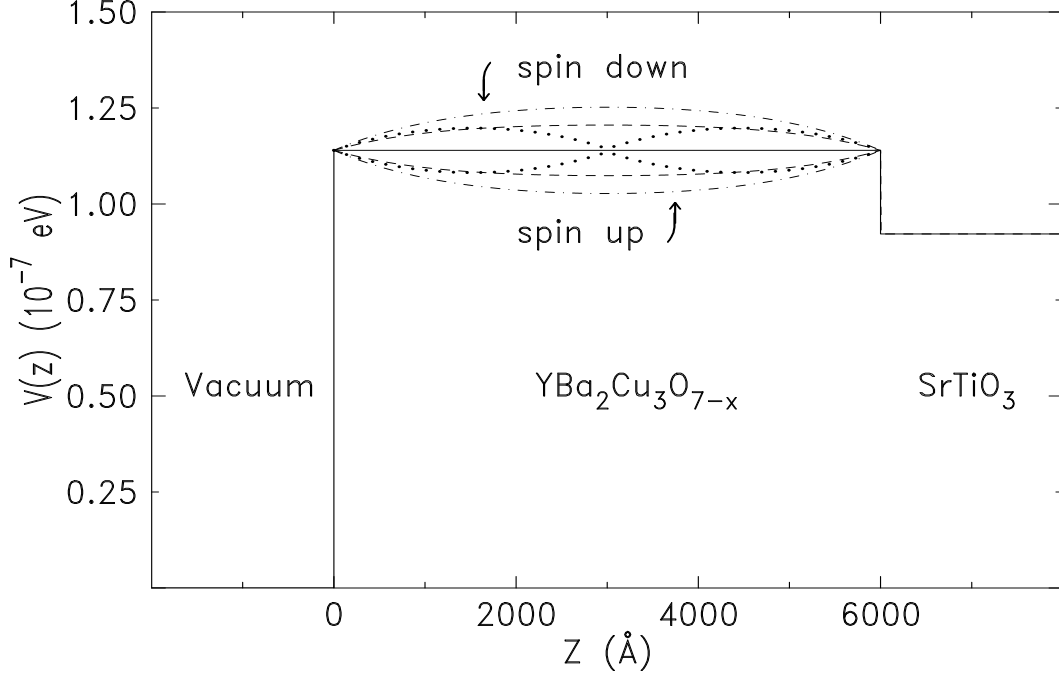


FIG. 15. Spin-up and spin-down neutrons encounter a different scattering potential due to the spatially varying magnetization in the superconductor. The scattering potential is calculated for: (Solid line) nuclear scattering only; (dot-dashed curve) London penetration without vortices; (dotted curve) vortices in the center of the sample; and a (dashed curve) uniform distribution of vortices. In each case, the lower branch is for spin-up neutrons and the upper branch is for spin-down neutrons.

where  $2\pi\hbar^2/m_n$  is  $\sim 2.6 \times 10^{-2}$  eV and  $4\pi M(z)$  is in a Gauss unit. Fig. 15 shows the neutron optical potential which is contributed by the nuclei and the spatial magnetization, assuming that a 6000 Å thick  $\text{YBa}_2\text{Cu}_3\text{O}_{7-x}$  on  $\text{SrTiO}_3$ ,  $\lambda_L = 1400$  Å and applied field 2500 Oe. The solid line shows the contribution of London penetration to the magnetization only and the dotted line and dashed line are calculated with vortices which mostly stay in the middle line of the sample (dotted line) and uniformly distribute through the sample (dashed line).

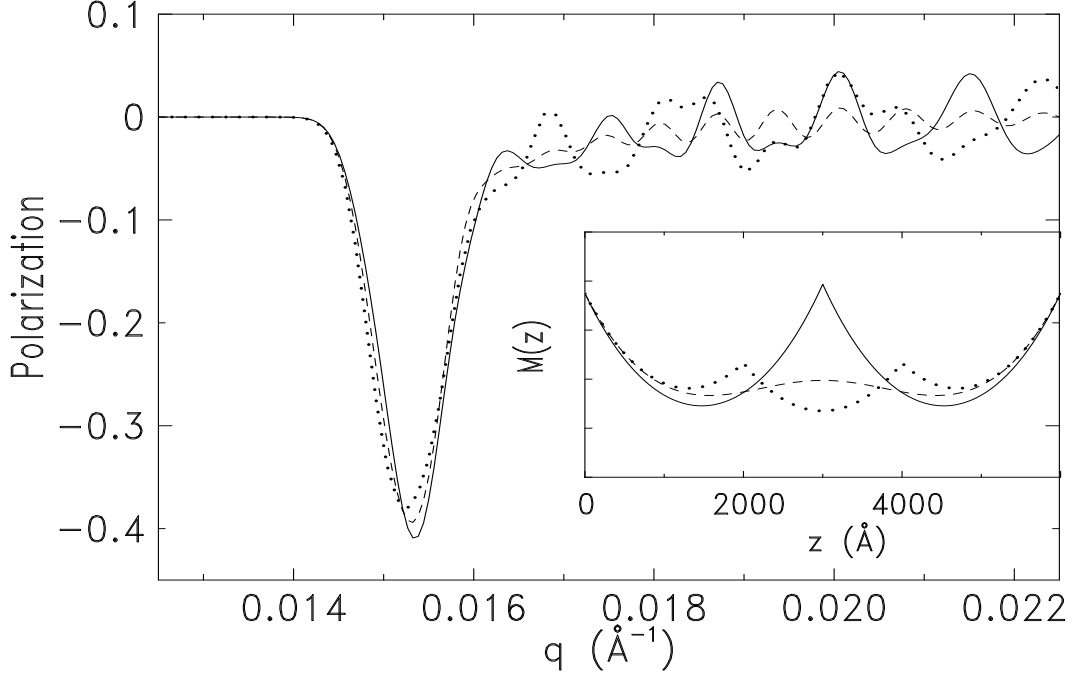


FIG. 16. Calculation of  $\Delta R/\bar{R}$  is for three different distributions of vortices (same average density). Inset shows the spatially varying magnetization for each case. (solid curve) vortices localized in the line through the center of the sample, (dotted curve) vortices localized on two lines and (dashed curve) vortices spread over a Gaussian distribution with FWHM, 1000  $\text{\AA}$ .

The polarization for spin-polarized neutron reflectivity was numerically calculated (using multi-sliced method described in Ch. 7) with different distributions of vortices and the same density of vortices 45 per  $\mu m^2$ , as shown in Fig. 16. For these calculations, the parameters for the specimen are the same in Fig. 15. And the angular divergence of the beam  $0.005^\circ$  is assumed. The calculations shows that the distribution of vortices could be more clearly observed at somewhat higher  $q$  because small  $q$  is corresponding with long d-space.





## 5. VORTICES PARALLEL TO SURFACE IN THIN SUPERCONDUCTING FILMS

### 5.1. Vortices in a $\text{YBa}_2\text{Cu}_3\text{O}_{7-x}$ Film

#### 5.1.1. *Characterization of a $\text{YBa}_2\text{Cu}_3\text{O}_{7-x}$ film*

For the studies of vortices which run parallel to surface by spin-polarized neutron reflectivity (SPNR), E. Paraoanu and Dr. L. H. Greene prepared a 6000 Å thick  $\text{YBa}_2\text{Cu}_3\text{O}_{7-x}$  (YBCO) film, *c*-axis perpendicular to a (1 cm × 1 cm)  $\text{SrTiO}_3$  (001) substrate surface (2 mm thickness), grown by the magnetron sputtering [36]. The resistivity, measured on similar samples by the four-probe technique, was 208  $\mu\Omega$  cm at room temperature with an onset to superconductivity at 89.8 K and a transition width, 0.8 K.

The X-ray specular reflectivity on the sample could not be obtained above the critical angle because of an enormous roughness of the surface. The rms surface roughness of the sample,  $170 \pm 30$  Å, was determined by unpolarized neutron reflectivity and atomic force microscopy (AFM) measurements. Figure 17 (a) shows the specular neutron reflectivity measured at 300 Oe and 10 K and the solid line is a best fit. The best fit shows that the rms roughness is larger than 140 Å. However specular neutron reflectivity could not determine the upper-bound of the

rms roughness because it is not very sensitive to such a large rough surface. The AFM measurements showed that the rms roughness of the sample was from 140 Å to 200 Å depending on the positions. These also showed the step edge pattern on the surface with randomly distributed rectangular shaped bars, around  $1 \times 4 \mu m^2$  area and  $\simeq 0.4 \mu m$  height which is similar to the previous observation by L. H. Greene *et al.* [36].

The SPNR measurements were performed using the GANS reflectometer at Missouri University Research Reactor which is described in Ch. 3. The sample was located in vacuum and cooled to 10 K at zero field using a close-cycle refrigerator. Subsequently, a magnetic field was applied parallel to the surface using a electromagnet which can generate magnetic field from 0 to 2400 Oe. The reflectivity was measured consecutively for spin-up and spin-down neutrons. The size of beam at the sample was 0.23 mm, the angular divergence was  $0.02^\circ$  and the polarization efficiency of the incident beam was around 95 %. In this measurement, the analyzer mirror was not used.

#### 5.1.2. SPNR from $YBa_2Cu_3O_{7-x}$

At 300 Oe and 10 K, the SPNRs measured as a function of momentum transfer,  $q$ , near the critical angle are shown in Fig. 17 (a). Figure 17 (b) shows the spin up and spin down reflectivity difference divided by their average,  $\Delta R/\bar{R}$ , which more clearly shows the contribution of magnetization to the reflectivity. The

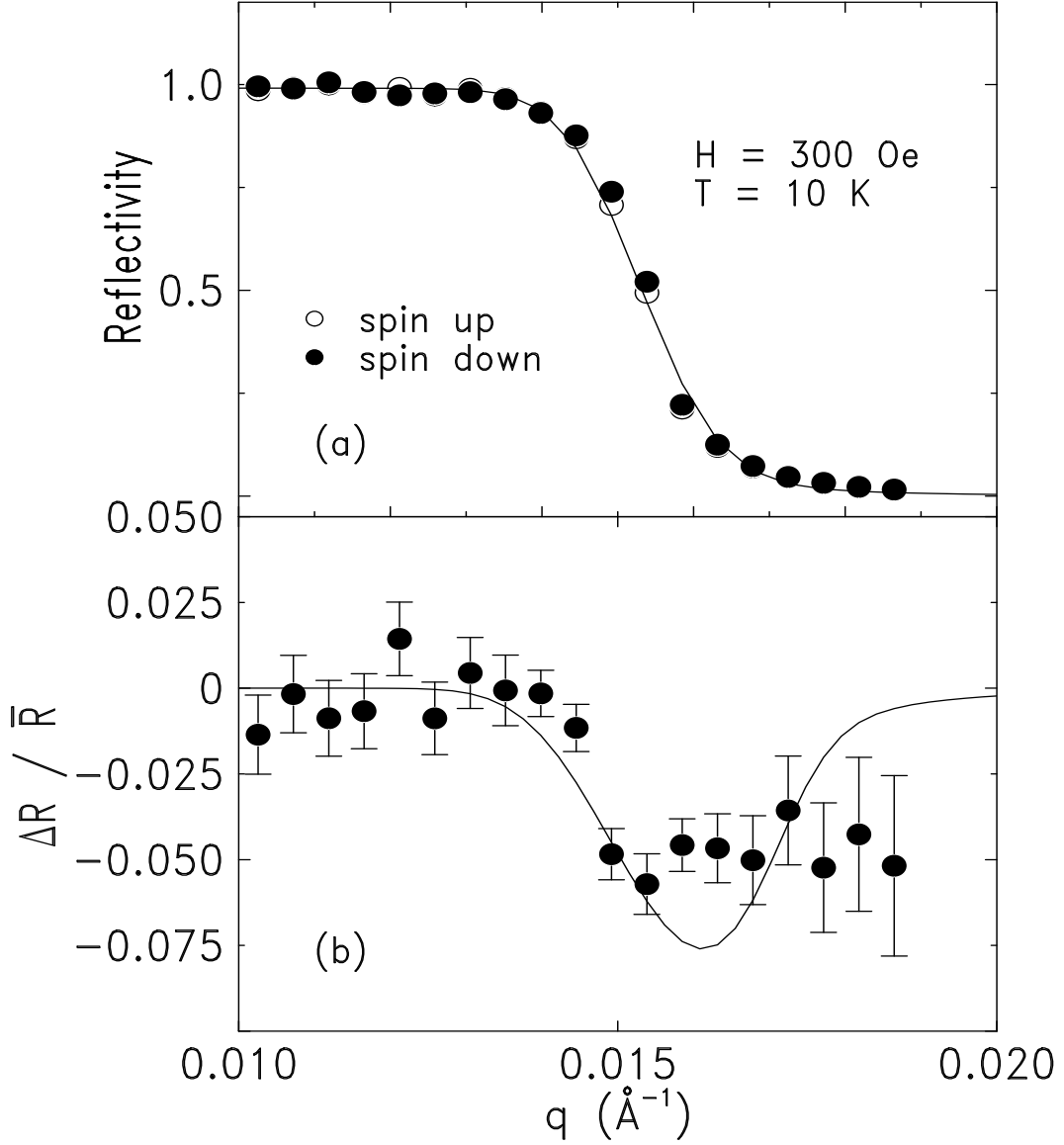


FIG. 17. (a) shows the spin-up and spin-down neutron reflectivities vs.  $q$  at 300 Oe and 10 K and the solid line is a best fit. (b) shows  $\Delta R / \bar{R}$  obtained from the data in (a). The solid line is the theoretical calculation with  $\lambda_L = 1400 \text{ \AA}$ .

solid line is a theoretical calculation from the London equation for a thin film (4.8) using a London penetration depth,  $1400 \text{ \AA}$ , obtained from SPNR by A. Mansour *et al.* [8]. Because of the surface roughness, the reflectivity from the  $6000 \text{ \AA}$  thick

film could not be obtained at higher  $q$ , as shown in Fig. 17 and 18. We could not determine the magnetic screening length of the superconductor because of the interdependency of the nuclear scattering density of the YBCO film, incident beam wave length and surface roughness in the reflectivity. However at higher field, we obtain a large magnetic signal.

At 2400 Oe and 10 K, the spin-dependent neutron reflectivities were measured as a function of  $q$ , as shown in Fig. 18 (a). Figure 18 (b) shows the  $\Delta R/\bar{R}$  obtained from the data in Fig 18 (a) and the solid line is a theoretical model calculation described in Sec. 4.2. The calculation shows that the width of the depression is mainly determined by resolution. And the depth of the depression is contributed by not only the magnetic scattering parameters (magnetic screening length, presence of vortices and polarization efficiency) but also the nuclear scattering parameters (neutron scattering densities of YBCO and  $\text{SrTiO}_3$ , surface roughness, and resolution). The position of the extremal value is directly related to the critical angle which is determined by the wave length of the beam and the nuclear scattering density of the YBCO film. Because of uncertainties of the parameters, we could not extract the vortex contribution to the reflectivity from the data measured at 2400 Oe. However at a fixed temperature, the parameters which affect to the SPNRs are constants to the applied field except the contribution of vortices. Therefore, the measurement of field dependent  $\Delta R/\bar{R}$  will clarify vortex contribution to SPNR, magnetization in the film.

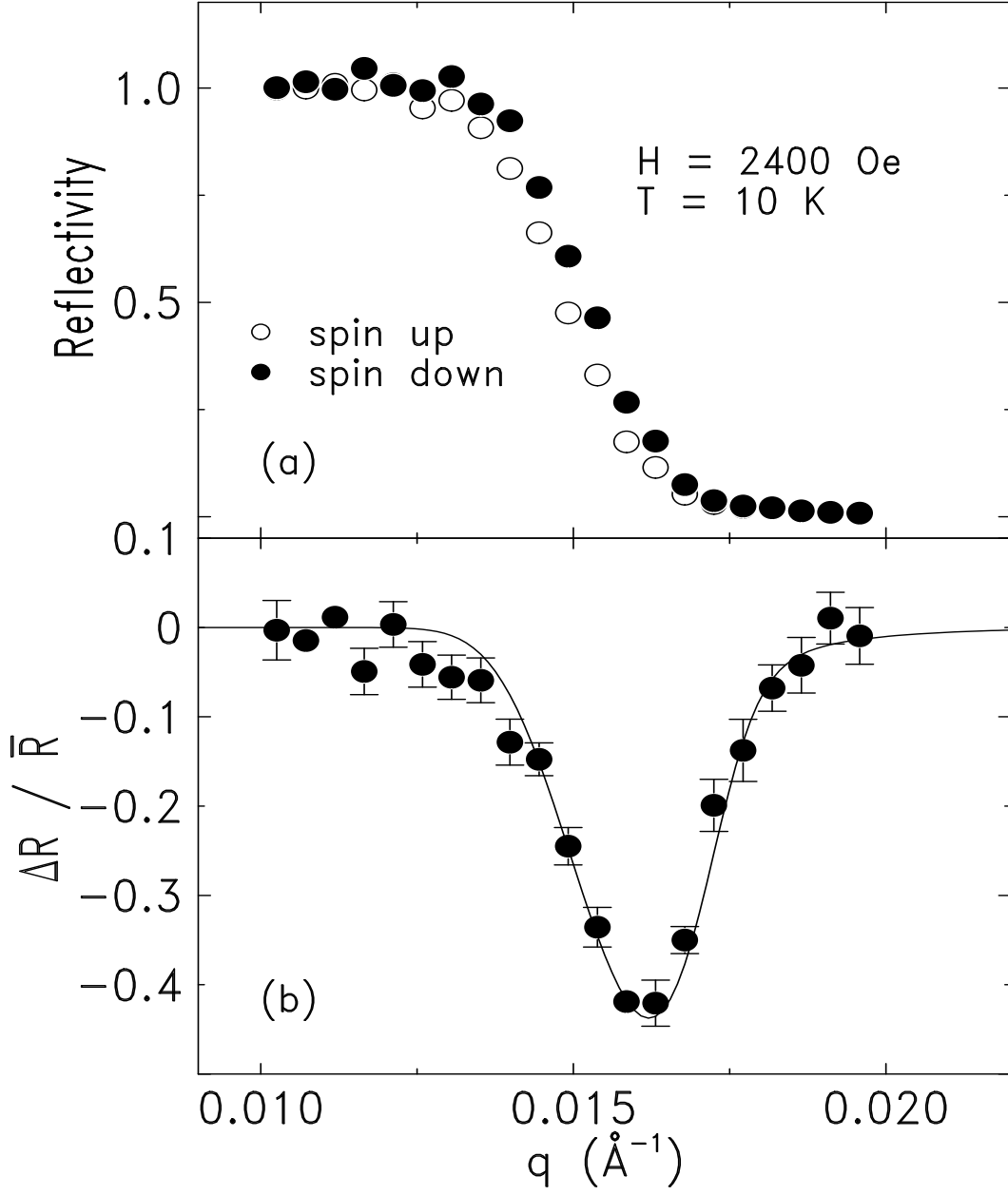


FIG. 18. (a) shows the spin-up and spin-down neutron reflectivities vs.  $q$  at 2400 Oe and 10 K. (b) shows  $\Delta R / \bar{R}$  obtained from the data in (a) and the solid curve is a calculation with the theoretical model described in Sec. 4.2.

## 5.2. Vortices measured by SPNR

Figure 19 shows the measured extremal value of  $\Delta R/\bar{R}$  as a function of applied field. Initially, at low field, there is a nearly linear change in  $\Delta R/\bar{R}$  due to the London penetration; however, at higher field, the slope of  $\Delta R/\bar{R}$  changes as vortices are generated. The hysteresis shape unambiguously demonstrates that vortices can be detected by SPNR. Even when the applied field is reduced to a small value (65 Oe) there is a large spin-polarized signal (Fig. 20 (c)), which is opposite in sign to that of Fig. 20 (a), due to the remanent condition where flux is trapped in the sample. From the measured data, one would extract the density of vortices in the film. However without being known the parameters which contribute to SPNR, the density of the vortices in the film will not be obtained from the SPNR data.

In Fig. 19, the dotted line is a theoretical calculation without including vortices in the specimen. From the calculation, the uncertainty limits of the parameters could be determined. However it is not clear yet how the parameters are correlative with the density and distribution of vortices at higher field. I chose the two sets of parameters (YBCO neutron scattering density ( $Qc^2$ ), London penetration depth ( $\lambda_L$ ) and the beam wave length ( $\lambda$ )) with which the calculated values are consistent with the dotted line in Fig. 19. With given a vortex density and a uniform distribution of vortices, the polarizations are calculated for the two sets of parameters. Figure 20 shows the SPNR measurements and the calculations. The

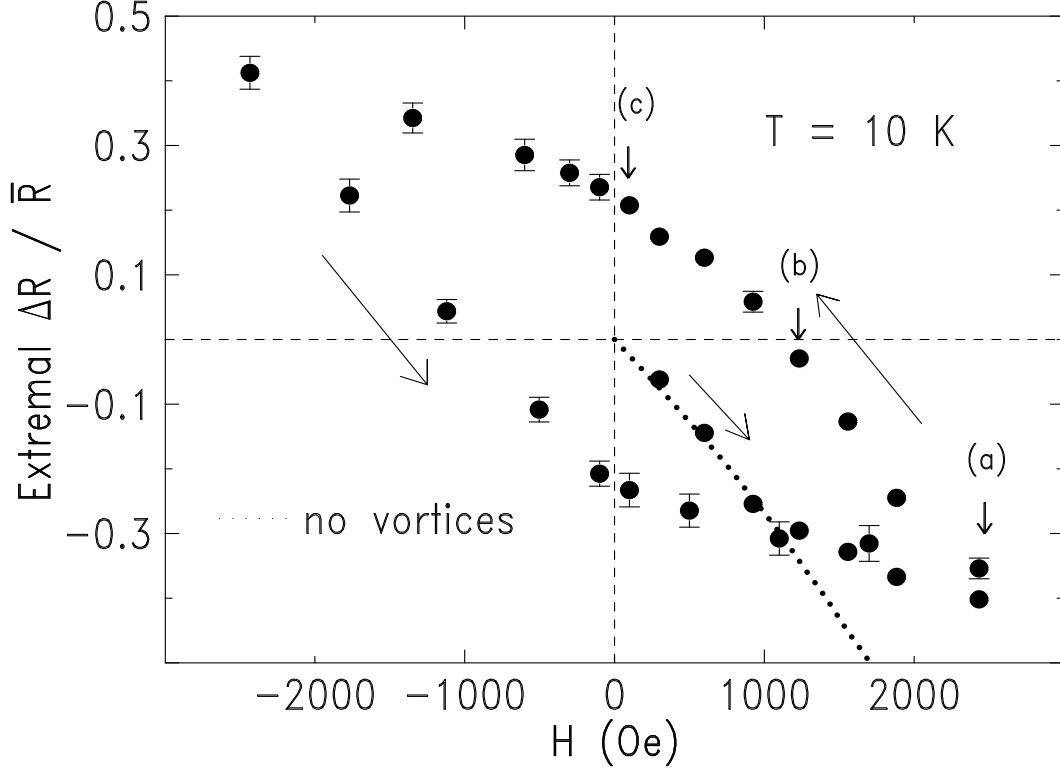


FIG. 19. Extremal  $\Delta R/\bar{R}$  was measured as a function of applied field. The dotted line is the theoretical calculation, assuming that London penetration only at the surfaces contributes to the magnetization. The big arrows indicate the order in which the data were taken. The small arrows indicate the fields at which  $q$ -dependent SPNR was measured and shows in Fig. 20.

SPNR measured as a function of  $q$  at three different fields (2400 Oe, 1200 Oe and 65 Oe) indicated by the down arrows in Fig. 19.

Figure 20 (a), (b) and (c) show  $\Delta R/\bar{R}$  as a function of  $q$  at 2400 Oe, 1200 Oe and 65 Oe where the data were taken at 2400 Oe, 1200 Oe and 65 Oe consecutively. The solid line and dashed line are the theoretical model calculations with the two different sets of parameters. The difference between the two lines is negligible. For

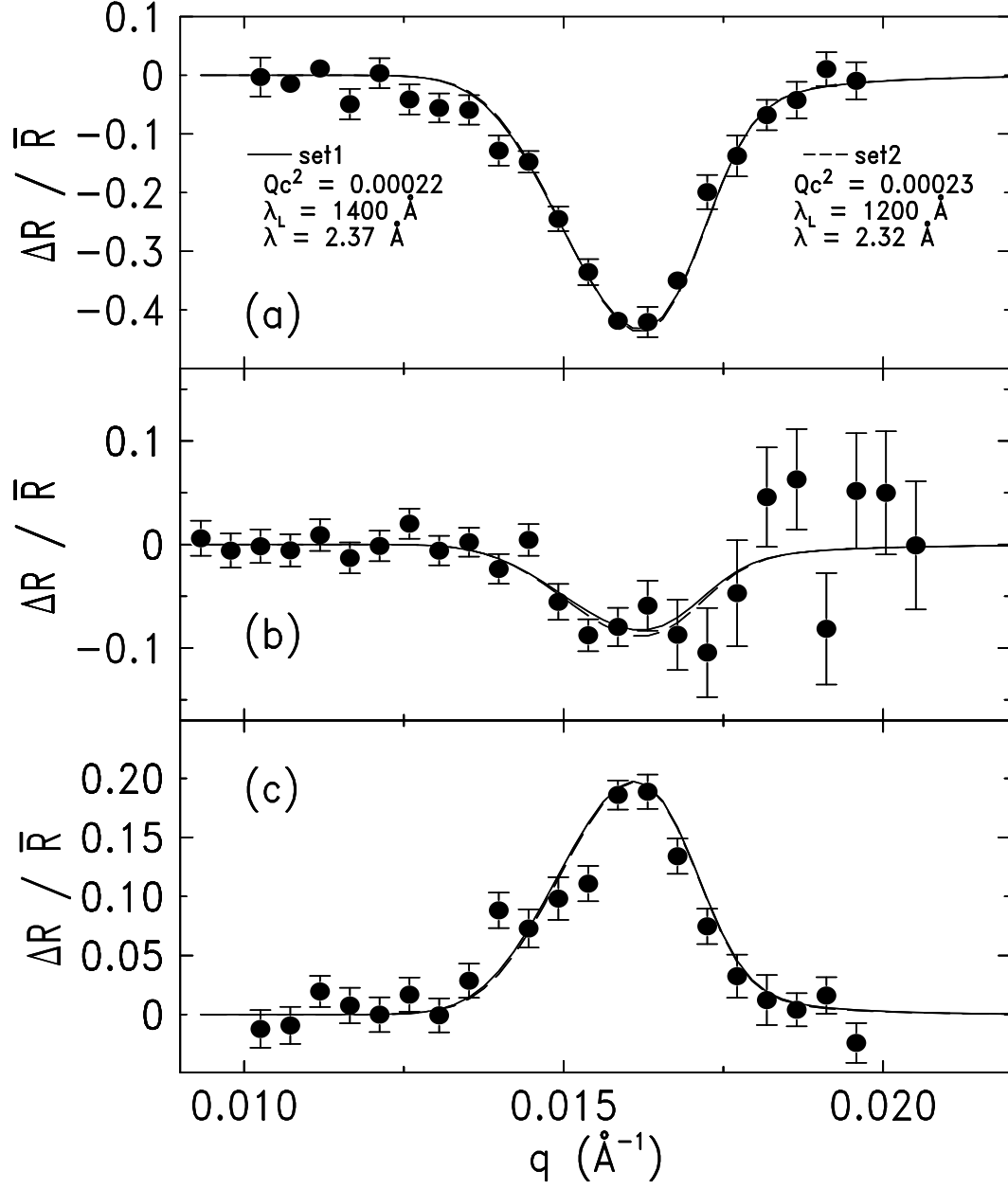


FIG. 20.  $\Delta R/\bar{R}$  vs.  $q$  were consecutively measured at 2400 Oe (a), 1200 Oe (b) and 65 Oe (c) as a function of  $q$ . The solid line and dashed line are the model calculations with the same parameters except with  $Qc^2$ ,  $\lambda_L$  and  $\lambda$ .



the calculations, the density of vortices 47 per  $\mu m^{-2}$  at 2400 Oe, 47 per  $\mu m^{-2}$  at 1200 Oe and 40 per  $\mu m^{-2}$  at 65 Oe obtained by a single-parameter least-squares fit to the data was used. And the uniform distribution of vortices was assumed. The SPNR data have limited sensitivity to the shape of the vortex distribution because these experiments were obtained at low  $q$  (dictated by the large surface roughness [38]) so that the average scattering density is effectively measured in this limit. For understanding spatial distribution of vortices, the reflectivity should be measured at high  $q$ , as shown in Fig. 16.

With assuming a uniform distribution of vortices in a 6000 Å thick YBCO superconducting film, the density of vortices at the three fields ( $47.7 \pm 2.3$  per  $\mu m^{-2}$  at 2400 Oe,  $53.7 \pm 5.2$  per  $\mu m^{-2}$  at 1200 Oe and  $41.8 \pm 5.1$  per  $\mu m^{-2}$ ) could be extracted from the SPNR data by a best fit, single-parameter least-squares fit. Analyzing data at the three fields show that one can extract the vortex density from the SPNR data measured as a function of applied field without knowing the exact values of the parameters which affect SPNR but you did require mutual consistencies among them.

The density of vortices, shown in Fig. 21, were extracted from the data in Fig. 19, assuming a uniform distribution of vortices and using the London penetration depth, 1400 Å [8]. Figure 21 shows that initially no vortices were in the superconductor and the vortices first enter the superconductor near  $1050 \pm 100$  Oe. Above  $H_{c1}$  the density of vortices is linearly increased up to the maximum field. As the field is reduced, there is little change in the vortex density until rather low

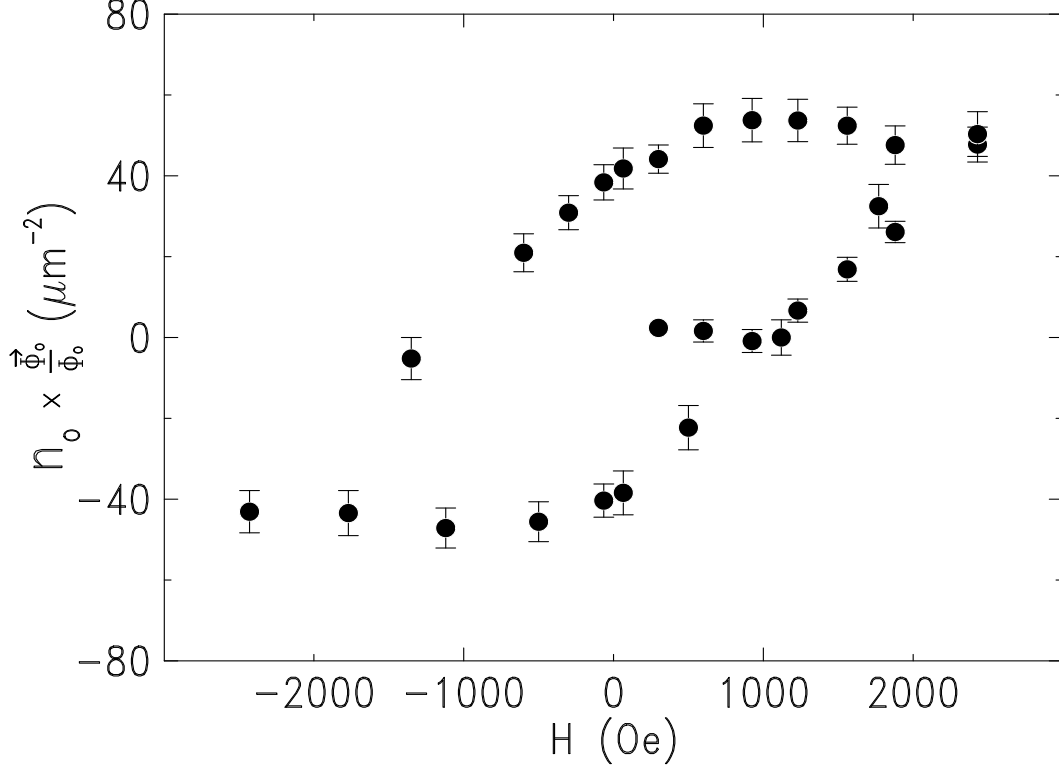


FIG. 21. The average density of vortices was extracted from the data in Fig. 19, using a theoretical model described in Sec. 4.2.

field, indicative of a barrier for vortices to exit the sample. The slope of the linear portions, which is symmetric for increasing or decreasing fields, is determined to be  $\Delta n_o / \Delta H = 0.036 \pm 0.006 \text{ Oe}^{-1} \mu\text{m}^{-2}$ . From Eq. (4.18), one can expect the slope,  $\Delta n_o / \Delta H \simeq 1 / \Phi_o = 0.05 \text{ Oe}^{-1} \mu\text{m}^{-2}$ , for assuming  $\Delta M = 0$ . The experimental value is slightly smaller, suggesting  $\Delta M / \Delta H \sim -0.14$ .

The measured  $H_{c1} \ 1050 \pm 100 \text{ Oe}$  which is much larger than  $\sim 372 \text{ Oe}$  calculated, using  $H_{c1} = \Phi_o / (4\pi\lambda_L^2) K_o(\xi/\lambda_L)$  assuming a bulk YBCO superconductor ( $\lambda_L = 1400 \text{ \AA}$  and  $\xi = 16 \text{ \AA}$ ). The low critical field in a *thin-film* superconductor could

be calculated, regarding the total free energy. The total free energy with a single vortex in a superconductor which has a single boundary was described in Eq. (2.14). Using Eqs. (4.7) and (4.8) the total free energy,  $W_T$ , with a single vortex in a *thin-film* superconductor could be described to,

$$W_T = W_o + \Phi_o H L_V \left( \frac{\cosh(z'/\lambda_L)}{\cosh(t/2\lambda_L)} - 1 \right) + \frac{\Phi_o^2 L_V}{4\pi \lambda_L^2} \sum_{n=-\infty}^{n=\infty} (-1)^{|n|} K_0 \left( \frac{|z' - nt - (-1)^{|n|} z'|}{\lambda_L} \right) \dots\dots\dots (5.1)$$

where  $W_o$  is the total free energy without the vortex and  $t$  is the film thickness.

For vortices entering a thin film superconductor, the surface barrier for a single vortex per the vortex unit length at the surface should be zero or smaller than zero.  $H_{c1}$  could be determined by defining  $(W_T - W_o) / (\Phi_o L_V) \text{---} z' = -t/2 + \xi \equiv 0$ .

$$H_{c1}(t) = \frac{1}{\cosh([-t + 2\xi]/2\lambda_L)/\cosh(t/2\lambda_L) - 1} \frac{\Phi_o}{(4\pi \lambda_L^2)} \times \left\{ K_0 \left( \frac{\xi}{\lambda_L} \right) + \sum_{n=-\infty, \neq 0}^{n=\infty} (-1)^{|n|} K_0 \left( \frac{|(-t + 2\xi)(1 - (-1)^{|n|}) - 2nt|}{2\lambda_L} \right) \right\} \dots\dots (5.2)$$

Equation (5.2) shows that  $H_{c1}$  for a thick specimen would not be the same as  $H_{c1}$  for a bulk superconductor because there is a surface barrier for a vortex at the surfaces without depending on the film thickness. Using Eq. (5.2),  $H_{c1}$  is calculated to be  $\sim 5000$  Oe with  $\lambda_L$  1400 Å and  $\xi$  16 Å.

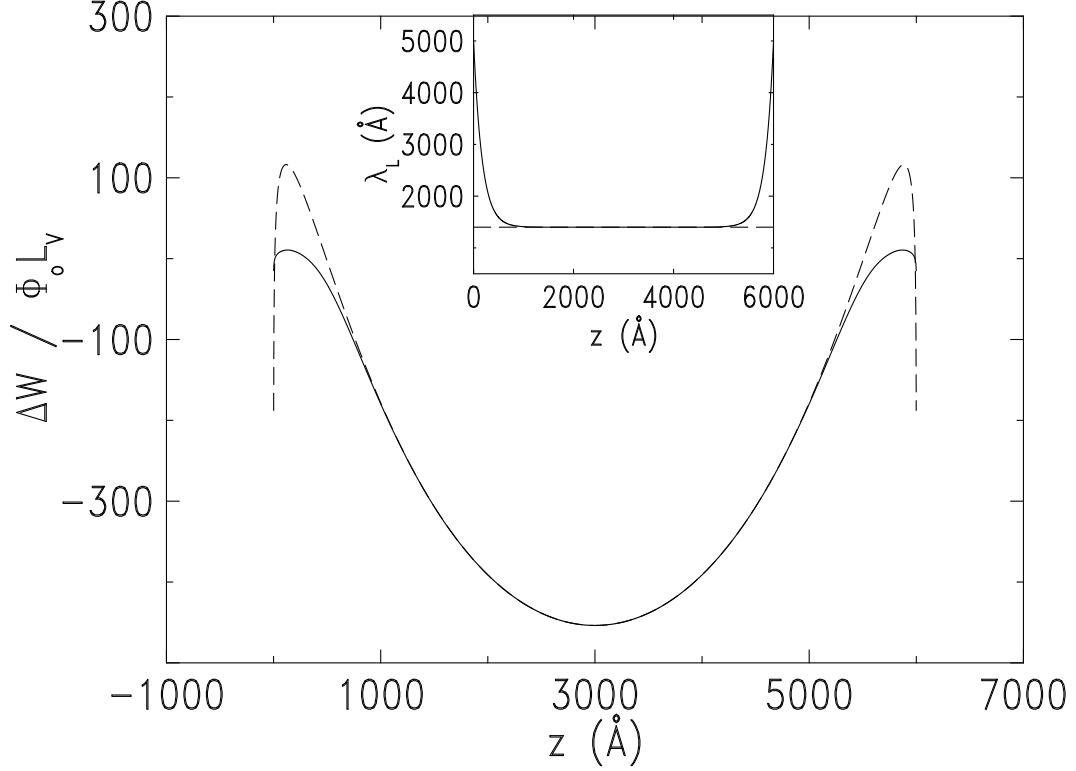


FIG. 22. Vortex potential was calculated as a function of position with assuming  $\lambda_L = 1400 \text{ \AA}$  and  $\xi = 20 \text{ \AA}$  (dashed line). The solid line is the calculation with assuming  $\lambda_L(z)$  shown in inset (solid line).

$H_{c1}$  in the measurement  $\sim 1050 \text{ Oe}$  is smaller than the calculated value  $\sim 5000 \text{ Oe}$ . That could be explained with the surface roughness. Near a boundary of a superconductor with rough surface, the density of Cooper pairs is smaller and the magnetic screening length is longer. It will contribute to the lower surface barrier. Figure 22 shows the free energy of a single vortex per its length (vortex thermodynamic potential),  $(W_T - W_o) / (\Phi_o L_V)$ , as a function of position for a  $6000 \text{ \AA}$  thick YBCO superconducting film. Using Eq. 5.1, the dashed line was calculated with  $\lambda_L = 1400 \text{ \AA}$  and  $\xi = 20 \text{ \AA}$  at  $1050 \text{ Oe}$ . The dotted line was calculated with

the same parameters to the solid line except with the magnetic screening length which is exponentially elongated over the length scale of the surface roughness 170 Å, as shown in the inset. The magnetic screening length in a superconductor which has rough surfaces was calculated,

$$\lambda_L(z) = \lambda_{L0} \left\{ 1.0 - \left[ 1.0 - \frac{\lambda_{Ls}}{\lambda_{L0}} \right] \frac{\cosh(\frac{2z-t}{2\sigma})}{\cosh(\frac{t}{2.0\sigma})} \right\} \dots\dots\dots (5.3)$$

where  $\lambda_{L0}$  is the magnetic screening length for the perfect surfaces,  $\lambda_{Ls}$  is the magnetic screening length at the surfaces and  $\sigma$  is the surface roughness. For the calculation in Fig. 22,  $\lambda_{Ls}$  5000 Å was used.

### 5.3. Vortices Pinned by Surface in a $\text{YBa}_2\text{Cu}_3\text{O}_{7-x}$ Film

The vortices pinned by bulk pinning centers in a superconductor could be studied at zero field after cycling the applied field up to above  $H_{c1}$  because the surface pinning vanishes for  $H = 0$  and the bulk pinning of vortices does not depend on the applied field, as shown in Eq. (2.12). In the vortex measurement of a 6000 Å thick YBCO film at 10 K, the density of vortices at 65 Oe was similar to the density at the maximum field within error. It means that most of the vortices were trapped by the bulk pinning centers which are parallel to the surface because the surface pinning (London penetration only) is negligible at 65 Oe. The surface pinning force in a thin film superconductor,  $F_s = -\partial W_T / \partial z'$ , can be calculated with

given the total free energy in Eq. (5.1).

$$F_s = -\frac{\Phi_o H L_V}{\lambda_L} \frac{\sinh\left(\frac{z'}{\lambda_L}\right)}{\cosh\left(\frac{t}{2\lambda_L}\right)} + \frac{\Phi_o^2 L_V}{4\pi \lambda_L^2} \sum_{n=-\infty}^{n=\infty, \neq 0} (-1)^{|n|} \frac{n}{|n|} K_1\left(\frac{|nt - z'(1 - (-1)^{|n|})|}{\lambda_L}\right) \dots\dots\dots (5.4)$$

where  $K_1()$  is the modified Bessel function of order 1. The first term, attractive force, is due to the surfaces and the summation terms are due to the images. It shows that as  $H$  goes to zero, the surface attractive force vanishes and only the force due to the image vortices remain. For a thick film, the contribution of the image vortices to the trapped vortex density is negligible.

For ascending field, the density of vortices would be determined by the characteristics,  $\lambda_L$  and  $\xi$ , of the superconductor. A superconductor will allow a minimum number of vortices which is necessary to keep a superconducting state. However, once vortices enter a superconductor, they may not exit although the density is larger than the minimum number of vortices at a field because of the surface barrier and bulk pinning force.

The reflectivity from the YBCO film at the extremal  $\Delta R / \bar{R}$  were measured as a function of applied field at 40 K, as shown in Fig. 23 (a) after zero field cooled. It shows that the polarization starts to saturate at the applied field,  $610 \pm 100$  Oe. When the field was reduced after cycling the applied field to the maximum field, the polarization curve did not follow the ascending curve. Figure 23 (b) shows the

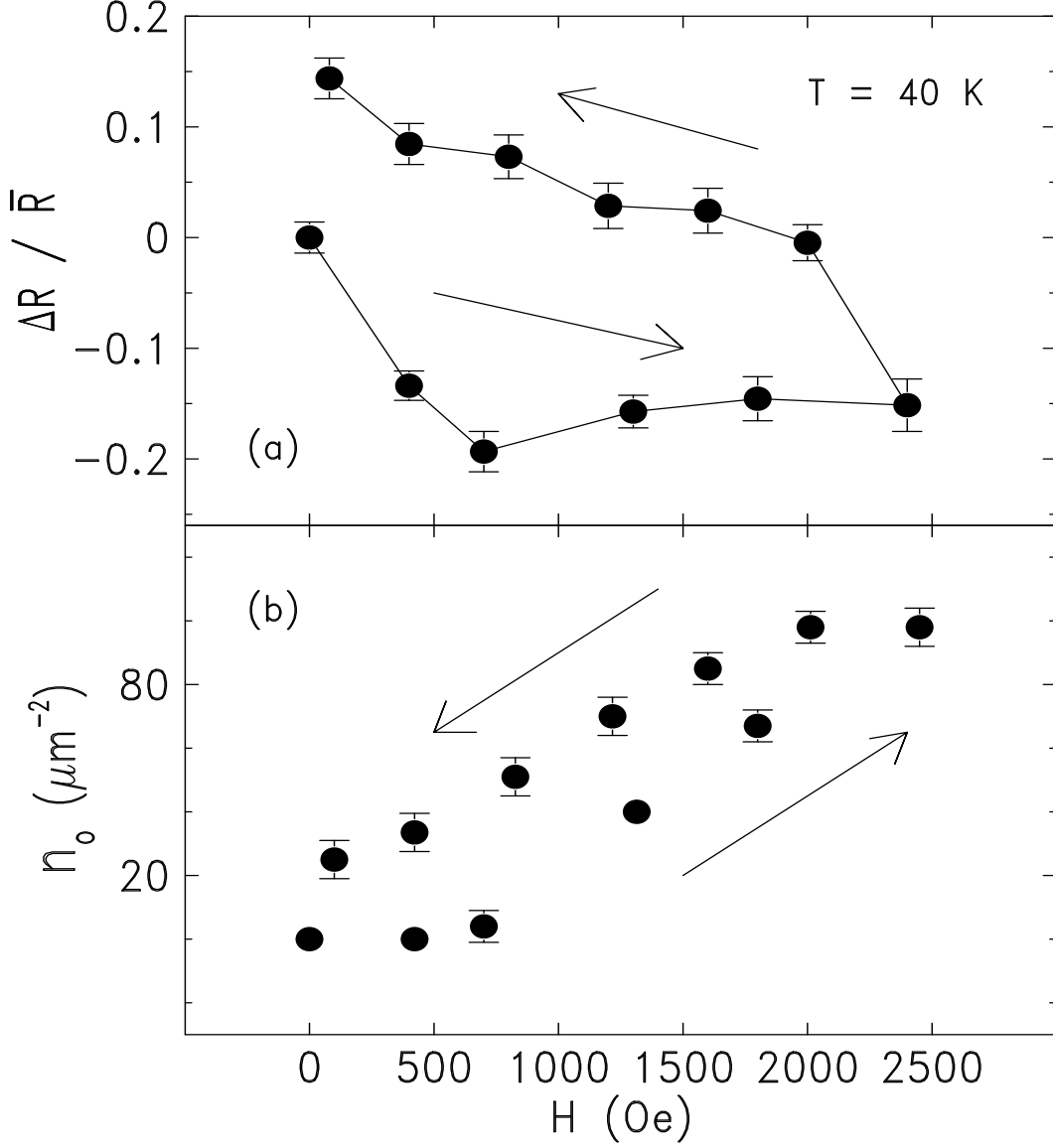


FIG. 23. (a) shows  $\Delta R/\bar{R}$  measured at 40 K as a function of applied field. (b) is the average vortex density extracted from the data in (a). The arrows indicate the directions where the data were taken.

extracted vortex density from the measured polarization in (a). For  $H > H_{c1}$ , the density of vortices was linearly increased as a function of applied field. The slope of vortex density for the ascending field,  $\Delta n_o/\Delta H$ , is  $0.053 \pm 0.005$  which

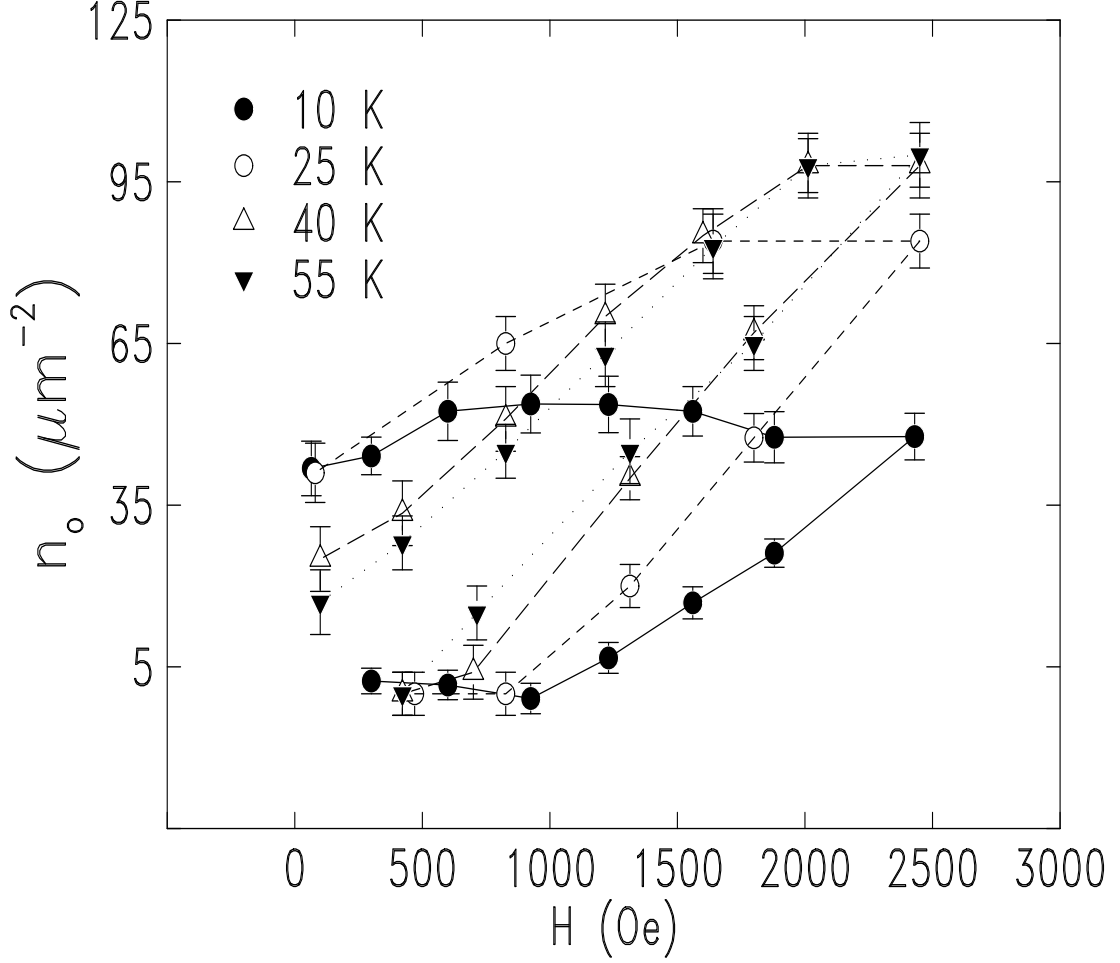


FIG. 24. The vortex densities vs. applied field were measured at 10 K, 25 K, 40 K and 55 K. The lines are for a guide to the eye.

could be compared to the expected value, 0.05, as assumed  $\Delta M = 0$ , that could be calculated, using Eq. (4.18). It clearly shows that the vortex density at 40 K is different from the density at 10 K shown in Fig. 21.

The vortex densities as a function of applied field were measured for different temperatures, as shown in Fig. 24. For the increasing field,  $H_{c1}$  is slightly dependent on temperature because the critical field is determined by magnetic screening



length and coherence length which are temperature dependent. The slope of the vortex density for ascending field,  $\Delta n_o/\Delta H$  is close to  $0.05 \text{ Oe}^{-1}m^{-2}$  except the slope at 10 K. It suggests that the magnetizations reaches the thermodynamic equilibrium above  $H_{c1}$  except at 10 K. For the decreasing field, the slope as well as the density of vortices at zero field are temperature dependent. As mentioned above, the vortex density at zero field is trapped by only the bulk pinning centers in a superconductor. The bulk pinning force is determined by the magnetic screening length and coherence length, as described in Ch. 2. As temperature is increased, the characteristic lengths are longer and the pinning force is smaller. Therefore less vortices trapped at higher temperature would be expected at the zero field after cycling to above  $H_{c1}$ . Figure 24 shows the well agreement with it.

At intermediate descending field, the vortices are trapped by surface screening as well as bulk pinning centers. For descending field, the density of vortices could be determined by surface screening, bulk pinning centers and the vortices for the thermodynamic equilibrium which could be determined from the measurement of vortices for ascending field. Assuming that the vortices trapped by the surface pinning is constant, the vortices trapped by surface  $n_s(H)$  could be extracted.

$$n_s(H) = n_d(H) - n_d(0) - n_a(H) \dots\dots\dots (5.5)$$

where  $n_d(H)$  is the vortex density for descending field,  $n_d(0)$  obtained by a best fit to the slope of the vortex density for the descending field is the vortex density at zero field after cycling the field to the maximum field and  $n_a(H)$  is the vortex

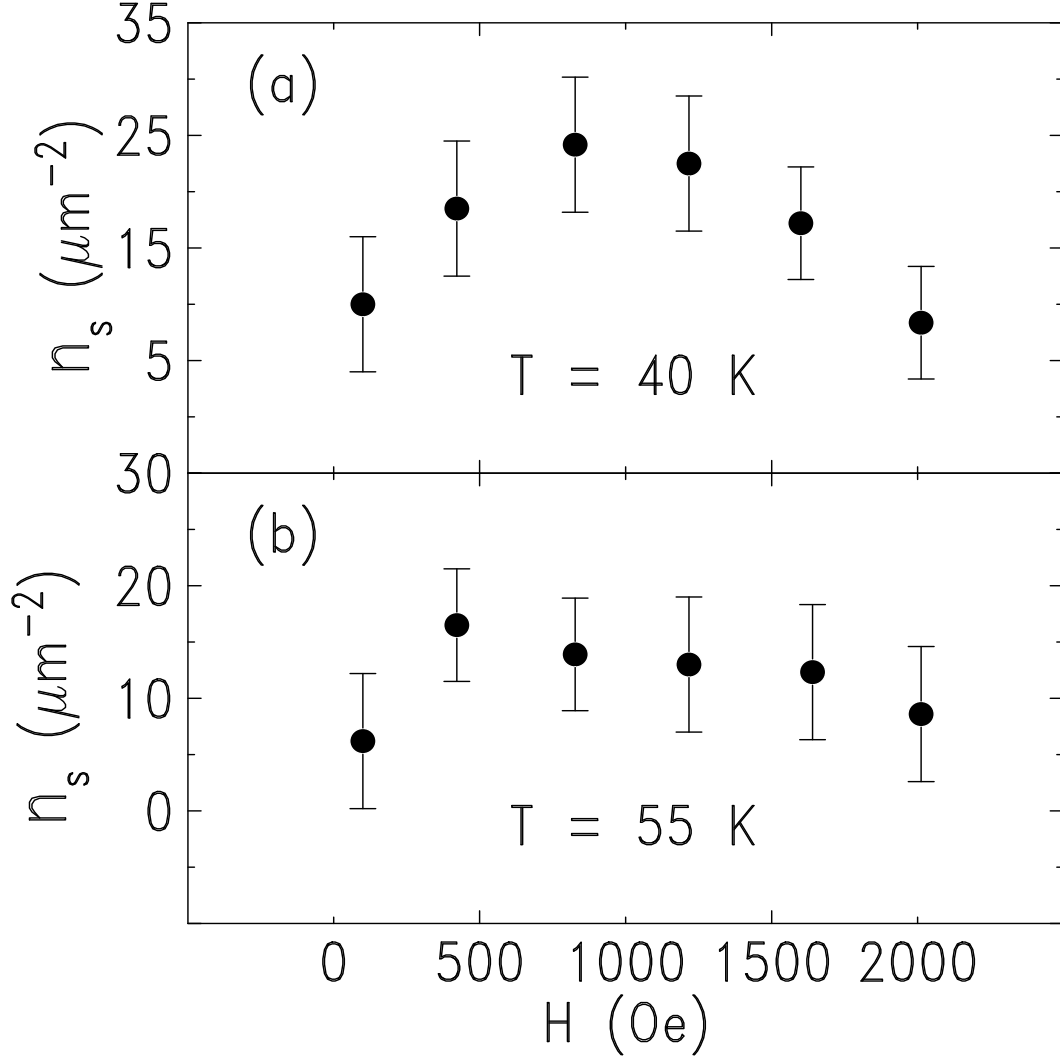


FIG. 25. The vortex density pinned by surface as a function of applied field at 40 K (a) and 55 K (b) is extracted from the data in Fig. 24 using Eq. (5.5).

density for ascending field.

Figure 25 shows that the density of vortices trapped by the surfaces were extracted from the data of 40 K and 50 K in Fig. 24. Figure 25 (a) shows that the vortices trapped by surface is maximum at the middle field. At a maximum applied field, vortices are not trapped by surface because they are required for the

thermodynamic equilibrium at which a specimen keeps it in the superconducting state for  $H > H_{c1}$ . Near zero field, the density of vortices trapped by surface is negligible because the surface pinning force is vanished at zero field. In Fig. 25 (b) at 55 K, the vortices trapped by the surfaces are nearly same for descending field within the error but is clearly bigger than zero. At the surface ( $z' = -t / 2$ , in Eq. (5.4)), for vortices entering a superconductor, their images give an attractive force on the vortices to pull out the vortices from the superconductor and thus there is a barrier near the surface. For vortices exiting from superconductor, the surface screening pushes the vortices toward the middle of the film.

For more understanding of the trapped vortices and the surface barrier, we have measured DC magnetization from a Au(300Å) /YBCO(2500Å) /SrTiO<sub>3</sub> using a SQUID magnetometer. YBCO(2500Å) c-axis perpendicular to the substrate surface (0.5 cm  $\times$  0.5 cm) was deposited by magnetron sputtering [36] and *in-situ* Au(300Å) was sputtered on the YBCO film to protect the YBCO film surface.

Figure 26 shows the magnetization from the Au(300Å) /YBCO(2500Å) /SrTiO<sub>3</sub> film measured as a function of applied field with the geometry where applied field near parallel to the film surface at zero-field cooled 4.5 K (open circle) and 40 K (solid dot). At 4.5 K, the vortices first enter the superconductor is *sim*5500 Oe which is slightly smaller than 7000 Oe predicted using Eq. (5.2) with  $\lambda_L$  1400 Å and  $\xi$  16 Å. The surface roughness ( $> 50$  Å [30]) helps the vortices entering the superconductor at slightly smaller field, as described above. For the descending field (after cycling the field up to 5 Tesla), the magnetization curve

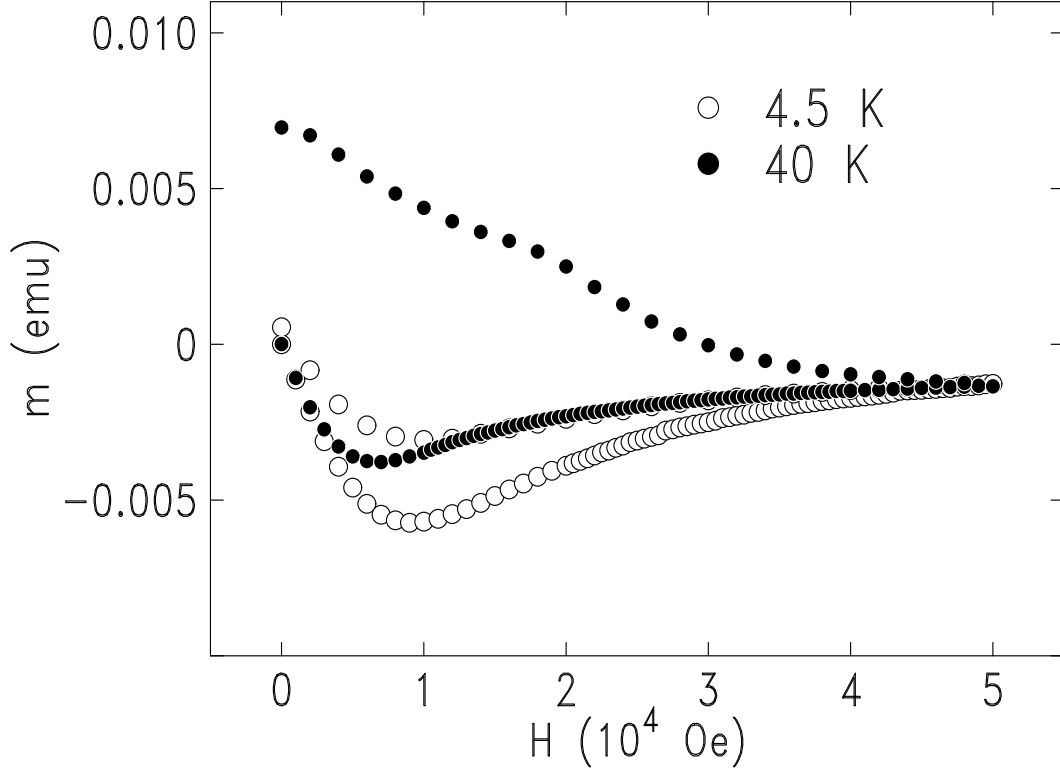


FIG. 26. The magnetic moment was measured from a  $\text{Au}(300\text{\AA})/\text{YBCO}(2500\text{\AA})/\text{SrTiO}_3$  film by SQUID at zero-field cooled 4.5 K and 40 K with applied field parallel to the surface.

slightly different from the magnetization for the ascending field. That is big different from the SPNR measurements from a  $\text{YBCO}(6000\text{\AA})/\text{SrTiO}_3$ , as described above. It suggests that the film thickness affects the trapped vortices.

At 40 K, the vortices first enter the superconductor at  $\sim 4000$  Oe which is smaller than 5500 Oe at 4.5 K.  $H_{c1}$  in a film superconductor depends on  $\lambda_L(T)$  and  $\xi(T)$ . The temperature dependent London penetration depth,  $\lambda_L(T)$ , and the

coherence length,  $\xi(T)$  [5] could be calculated using,

$$\left. \begin{aligned} \lambda_L(T) &= \lambda_L(0) \frac{1}{\sqrt{1-(T/T_c)^4}} \\ \xi(T) &= \xi(0) \frac{\sqrt{1+(T/T_c)^2}}{\sqrt{1-(T/T_c)^2}} \end{aligned} \right\} \dots\dots\dots (5.6)$$

where  $\lambda_L(0)$  and  $\xi(0)$  are the London penetration depth and coherence length at zero temperature and  $T_c$  is the critical temperature. At 40 K,  $\lambda_L$  1428 Å and  $\xi$  19.5 Å are calculated using Eq. (5.6). Using Eq. (5.2), the lower critical field could be calculated to be 5700 Oe with  $\lambda_L$  1428 Å and  $\xi$  19.5 Å. That is somewhat higher than the measurement  $\sim$ 4000 Oe and was expected, comparing to the measurement and calculation at 4.5 K.

For the descending field at 40 K, the magnetization shows large number of vortices trapped in the superconductor that was not expected. The vortex pinnings, surface pinning and bulk pinning, depends on temperature and they would be weaker at higher temperature. The large magnetic signal for descending field at 40 K will be explained by the vortex orientation change in the following section. The SQUID pick-coil measures the magnetization perpendicular to the surface (with demagnetization) as well as the magnetization parallel to the surface.

## 5.4. Vortices in a Nb Film

### 5.4.1. Characterization of a Nb Film

A 1370 Å thick Nb was deposited on a 1 cm  $\times$  1 cm Al<sub>2</sub>O<sub>3</sub> (1 $\bar{1}$ 02) substrate by dc-magnetron sputter deposition [39] in a UHV-compatible stainless-steel chamber with a base pressure of less than  $\sim 1 \times 10^{-8}$  Torr. Before the Nb deposition, gentle, *in-situ* Ar<sup>+</sup> etch was performed to remove any oxide layer on the substrate surface. During Nb deposition, an Ar partial pressure of  $7 \times 10^{-3}$  Torr and the temperature of the substrate at  $\simeq 470^\circ\text{C}$  were kept. Al of thickness 500 Å was consecutively deposited, *in-situ*, to protect the surface of Nb.  $T_c = 9.25 \pm 0.25$  was determined by SQUID magnetization measurement at 50 Oe that is consistent with  $T_c = 9.11$  K with width of the transition of 0.06 K found by 4-probe resistivity measurement on an adjacently grown sample. X-ray reflectivity measurements were performed on the specimen to understand the interfaces of the sample and discussed in Sec. 7.4 in detail.

The neutron reflectivity measurements were performed at the GANS reflectometer, Missouri University Research Reactor. For the measurements, the sample was zero-field cooled and held at  $2 \pm 0.2$  K in the superconducting magnetic cryostat which can generate 7 Tesla of static magnetic field and hold sample temperature from 1.5 K to 300 K. The beam size at the sample position  $\simeq 0.23$  mm and the angular divergence of the beam  $0.018^\circ$  was measured in the scattering plane. The polarization efficiency of the incident neutrons 93 % were taken into

account during the analysis of the reflectivity data. The SPNR was consecutively measured for spin up and spin down of neutrons near the critical angle below which the beam is totally reflected by the surface.

For the SQUID magnetization measurements, the sample used in the neutron experiments was cut to  $0.36 \times 0.26 \text{ cm}^2$  and placed in a SQUID magnetometer cryostat in which the sample surface was near parallel to applied field. The magnetization of the zero-field cooled sample was measured for depending on applied field and tilt angle between the applied field and the surface.

#### 5.4.2. SPNR from a Nb Film

The specular reflectivities for spin-up and down neutrons were measured as a function  $q$ ,  $4\pi\sin\theta/\lambda$  at 1000 Oe and 2 K, as shown in Fig. 27 (a). The period of the oscillations is corresponding to the Nb thickness of  $1370 \pm 10 \text{ \AA}$  and the solid line, a best fit gave the interface roughnesses,  $13 \pm 1 \text{ \AA}$  at Al/Nb and  $30 \pm 2 \text{ \AA}$  at Nb/Al<sub>2</sub>O<sub>3</sub> which could be compared with the grazing angle X-ray reflectivity measurement (discussed in Sec. 7.4). Figure 27 presents the reflectivity difference for spin up and down neutrons divided by their average,  $\Delta R/\bar{R}$ . The solid line is calculated with the magnetic screening length,  $\lambda_L$ , of 490  $\text{\AA}$  assuming that the applied field 1000 Oe is in Meissner regime. The reason of  $\lambda_L$  490  $\text{\AA}$  chosen will come later. The dotted line and dashed line are calculated with including vortices, by using a theoretical model discussed in Sec. 4.2.

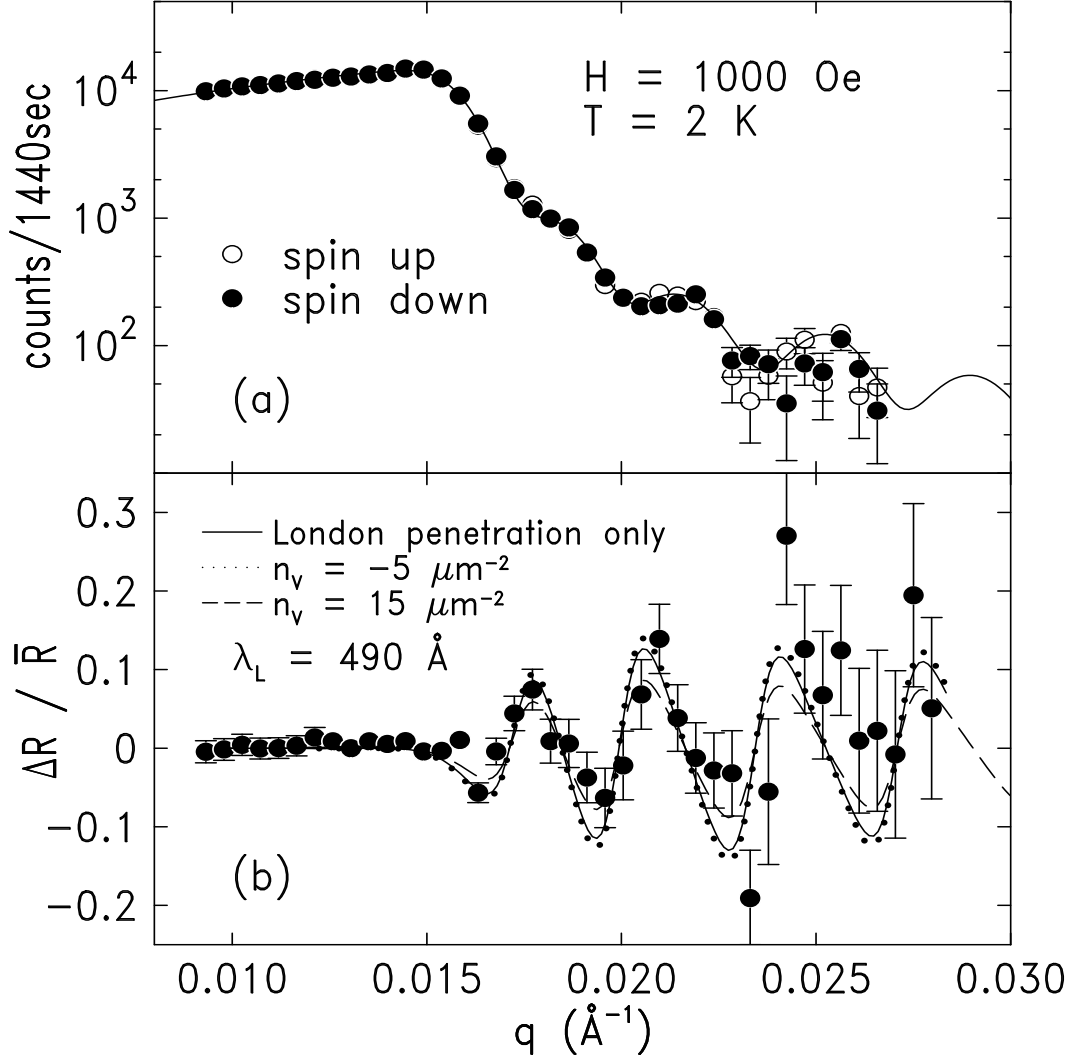


FIG. 27. (a) shows the reflectivities for spin-up and spin down neutrons measured at 2 K and 1000 Oe. The solid curve is a best fit. (b) shows  $\Delta R / \bar{R}$  from the data in (a) and the solid line is theoretical calculation with assuming no vortices and dashed and dotted curves with assuming vortices uniformly distributed.

$\Delta R / \bar{R}$  at  $0.38^\circ$  of  $2\theta$  (the first maximum) was measured as a function of applied field, as shown in Fig. 28. The curve of ascending field gradually increased up to the applied field 2000 Oe and then declined. Figure 28 obviously shows that



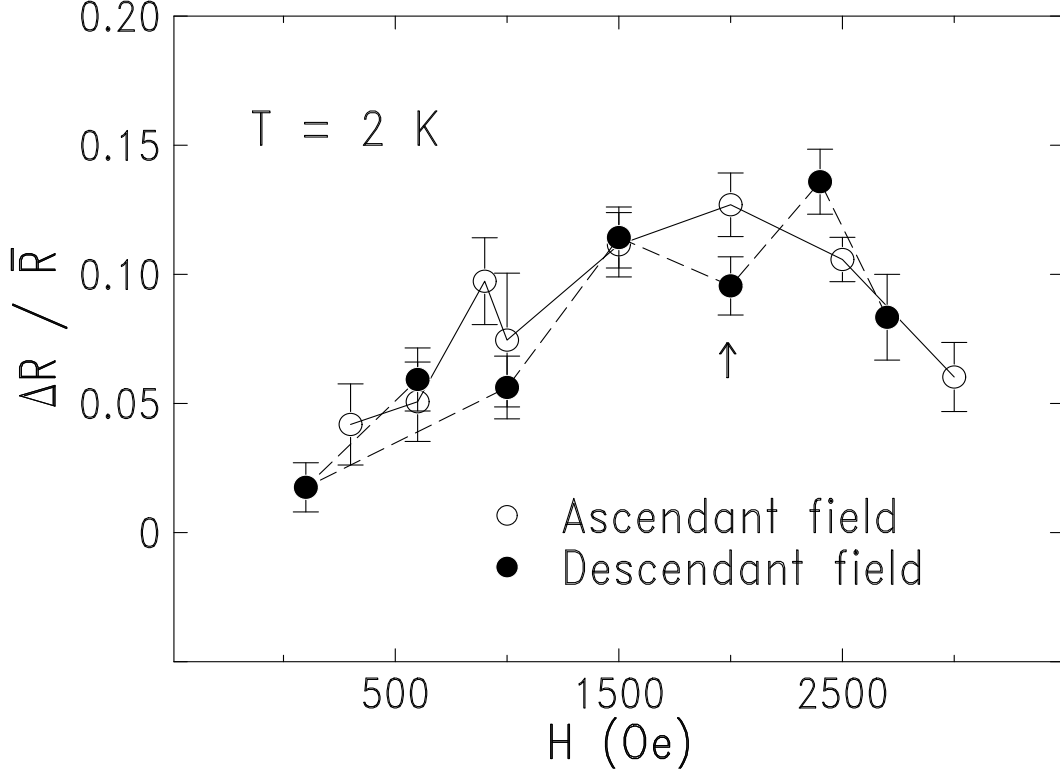


FIG. 28.  $\Delta R/\bar{R}$  at  $2\theta$  of  $0.38^\circ$  was measured for increasing and decreasing field. The lines are for a guide to the eye.

vortices first enter the superconductor at  $\sim 1500$  Oe and the density increases with the applied field. When the field decreased, the curve of descending field (closed circle) is similar to the ascending curve within error. At a small applied field, 100 Oe, it shows no remanent field in the Nb film. That is quite different from the studies on a  $6000 \text{ \AA}$  thick YBCO film that was discussed in the previous section. The difference of  $\Delta R/\bar{R}$  curve on Nb from the curve on YBCO for the increasing field might be due to the material difference, such as  $\lambda_L$  and  $\xi$ , which determine the thermodynamic critical field,  $H_c = \Phi_o / (2\sqrt{2}\pi\lambda_L\xi)$ . The descending curve difference of Nb and YBCO comes from the intrinsic pinning of the superconducting

films. The  $\Delta R/\bar{R}$  near zero field suggests that no strong bulk pinning centers run parallel to the surface in the Nb film. At a intermediate field, the vortices pinned by surface was not observed because the longer coherence of vortex creates lower vortex energy and spreads the energy over the core. Therefore the surface barrier to a vortex in a Nb film is lower than that in a YBCO film.

Using SPNR which is sensitive to the spatial gradient of magnetic field, the magnetic screening length of Nb was measured at 2 K and 600 Oe, as shown in Fig. 29 (a). Assuming that the contribution of vortices to the magnetization at 600 Oe zero-field cooled is negligible, we found  $\lambda_L = 490 \pm 110$  Å which well agrees with the previous SPNR works G. Felcher *et al.* [6] and H Zhang *et al.* [7]. At a high field, SPNR might reveal the spatial distribution of vortices. After the maximum field, 3000 Oe, had been applied and it was reduced to 2000 Oe, the reflectivity was measured as a function of  $q$ , as shown in Fig. 29 (b). The three lines are a best fit with assuming different distribution of vortices, a uniform distribution (solid line) with the vortex density of  $40 \mu m^{-2}$ , the vortices located in the middle line of the sample (dashed line) with the vortex density of  $28 \mu m^{-2}$ , and two lines of vortices (dotted line) with the vortex density of  $33 \mu m^{-2}$ . The small difference between the curves arises because the beat of the reflections from the front (Al/Nb) and back (Nb/Al<sub>2</sub>O<sub>3</sub>) interfaces of superconducting film dominates over the magnetic contribution of the vortex distribution. This effect is system dependent. Therefore we assume uniform distribution since we are not sensitive to the difference in this system.

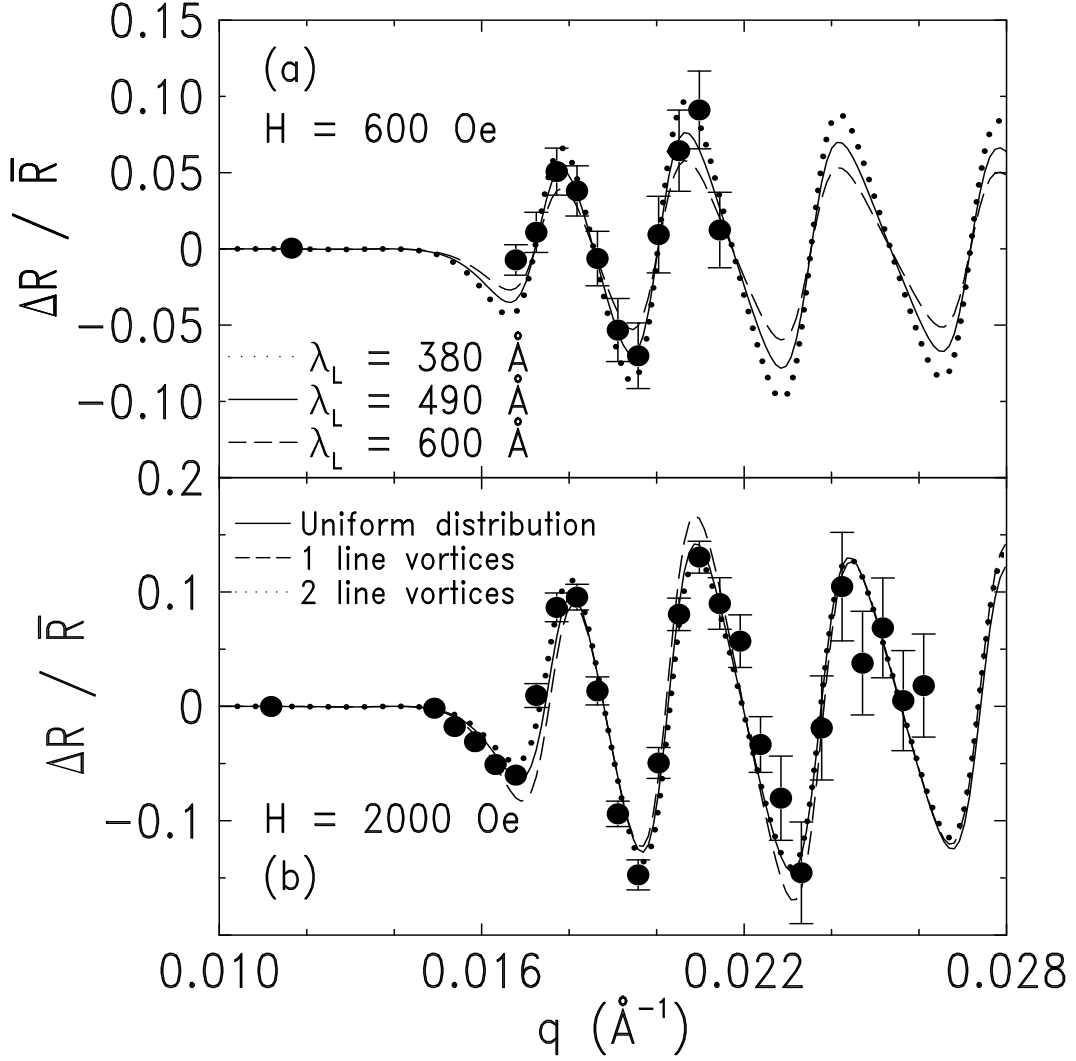


FIG. 29. (a) shows the  $\Delta R/\bar{R}$  at  $H = 600$  Oe and  $T = 2$  K and the lines are the theoretical calculations with different magnetic screening lengths. (b) shows the polarization at  $H = 2000$  Oe after the field cycling to 3000 Oe. The lines are a best fit, assuming that vortices are uniformly distributed through the sample (solid line), in the middle line of the sample (dashed line), and in two rows (dotted line).

By using the theoretical model described in Sec. 4.2 with the magnetic screening length 490 Å and the uniform distribution of vortices, the density of

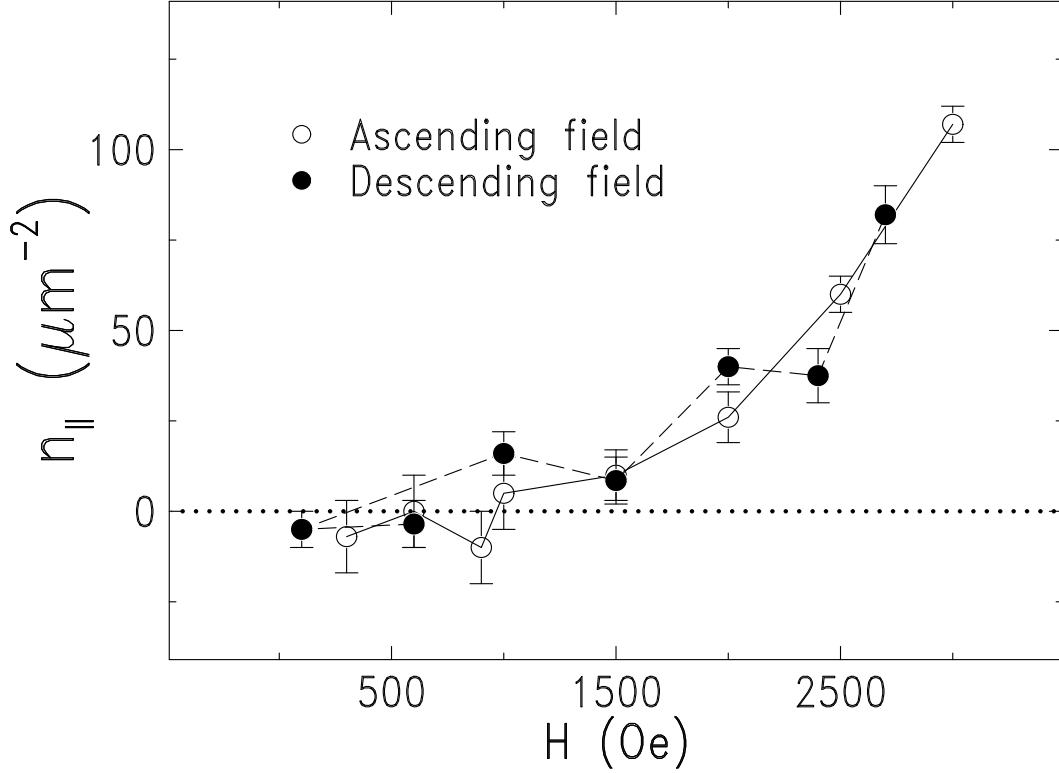


FIG. 30. Density of vortices was extracted from the data in Fig.28 assuming a uniform distribution of vortices and  $\lambda_L$  490 Å.

vortices was extracted from the data in Fig. 28 and shown in Fig. 30. It can be seen that  $H_{c1} \sim 1000$  Oe and the vortex density steadily increases at higher field. The reversible behavior of these data is preserved in the analysis of Fig. 30 and we explore this further with magnetization measurements.

### 5.5. DC Magnetization in a Nb Film

The DC magnetization measurements were performed on the same sample, Al(700Å) /Nb(1370Å) /Al<sub>2</sub>O<sub>3</sub>, which had been used in SPNR studies but it was

cut to  $2.6 \times 3.6 \text{ mm}^2$  because the original sample ( $10 \times 10 \text{ mm}^2$ ) did not fit the SQUID cryostat and we could not obtain a good SQUID data from a long rectangular sample ( $2.6 \times 10 \text{ mm}^2$ ). The sample ( $2.6 \times 3.6 \text{ mm}^2$ ) was mounted on an extension (G3 plastic rod) of a SQUID sample holder and the film surface runs near parallel to applied field. The SQUID magnetization was measured at different tilt angle between the film surface and applied field. The tilt angle was controlled by a non-magnetic plastic piece shimming the sample. The specimen was cooled at zero field, held 2 K and subsequently magnetic field was applied near parallel to the film surface. Figure 31 shows the magnetization measurements as a function of applied field with different tilt angles. Above  $H_{c1}$  at which the magnetization curves are maximum, the curves do not show the bumps which have been associated with vortex line transitions in artificially layered superconductors, Nb/Cu [20,21], Nb/Ti [22], Nb/Si [23] and Nb/Al [24]. That might suggest a uniformly distributed vortices in the film which is consistent with the SPNR measurements, as mentioned in the previous section.

$H_{c2}$  of the Nb was determined to be  $5300 \pm 300 \text{ Oe}$  by the SQUID magnetization measurement. Therefore the Nb characteristic length,  $\xi = \sqrt{\Phi_o/(2\pi H_{c2})}$  which is predicted by Ginzburg-Landau theory, can be calculated to be  $253 \pm 3.7 \text{ \AA}$  which is somewhat smaller than  $390 \text{ \AA}$  of A. V. Pronin *et al.* whose London penetration depth of the Nb was  $350 \text{ \AA}$  [61]. Using Eq. 5.2 and with the magnetic screening length ( $490 \pm 110 \text{ \AA}$ ) and coherence length ( $253 \pm 3.7 \text{ \AA}$ ), we could predict the lower critical field,  $H_{c1}$ ,  $995 \pm 85 \text{ Oe}$  which well agrees with the

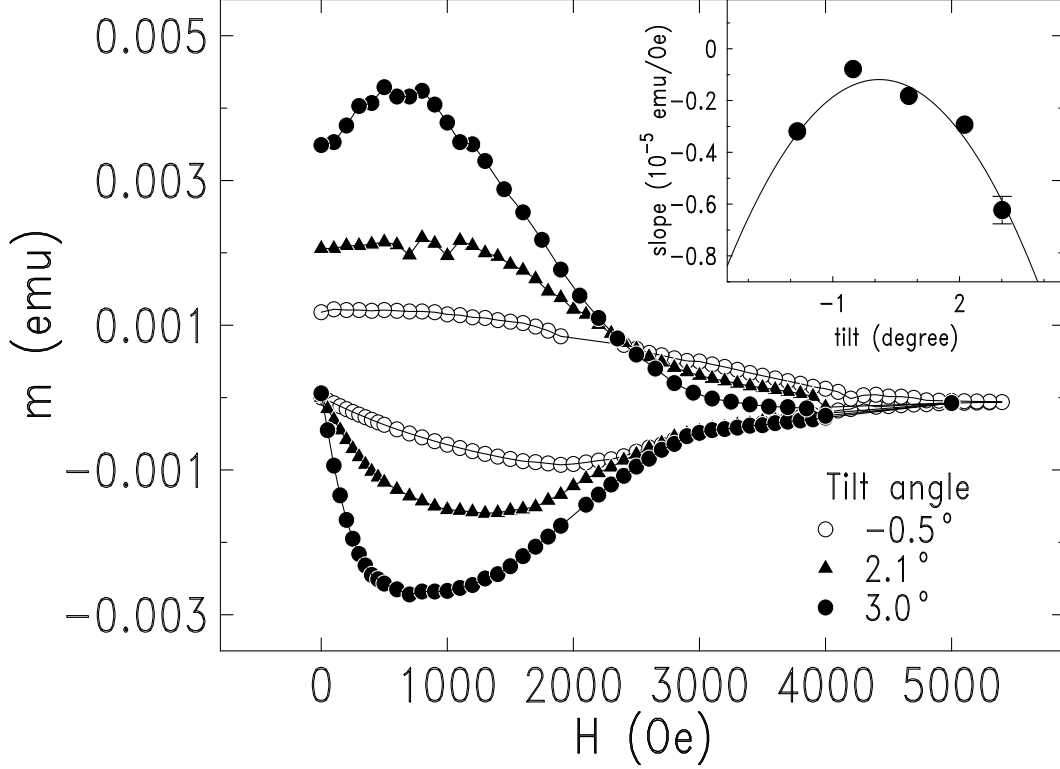


FIG. 31. Magnetic moment measured as a function of applied field for different tilt angles at 2 K, using a SQUID magnetometer. The solid lines are for a guide of the eye. The inset shows the initial slope of the magnetization in the linear region of small field as a function of tilt angle. The solid line is a best fit to a model described in the text.

measurements, shown in Fig. 27 and Fig. 30 ( $-0.5^\circ$  tilt).

Depending on the tilt angle, the magnetization for a small increasing field as well as  $H_{c1}$  was different. The inset of Fig. 31 shows the slope for small field,  $H < H_{c1}$  as a function of tilt angle. With the geometry of applied field perpendicular to the film surface, the magnetization in a superconductor can be calculated to

[28,40],

$$4\pi M_{\perp} = -\frac{H_{\perp}}{(1-N)} \dots\dots\dots (5.7)$$

where N is a demagnetization factor, a pure geometrical factor. As a superconducting film is placed with an angle to applied field, the magnetization of the film for the Meissner regime will be,

$$4\pi \vec{M} = H \cos\theta \left\{ \frac{2\lambda_L}{t} \tanh\left(\frac{t}{2\lambda_L}\right) - 1 \right\} \hat{\parallel} - \frac{H \sin\theta}{1-N} \hat{\perp} \dots\dots\dots (5.8)$$

where  $\theta$  is tilt angle. The measured magnetization by SQUID is  $M_{\parallel} \cos\theta + M_{\perp} \sin\theta$ . The solid in the inset of Fig. 31 is a best fit to this model and shows the demagnetization factor  $0.998 \pm 1.4 \times 10^{-3}$  which is slightly bigger than the calculation of 0.994 assuming a square. For a square, the demagnetization factor [43] will be,

$$N = \frac{2}{\pi} \sin^{-1} \left( \frac{1}{1+q} \right) \dots\dots\dots (5.9)$$

where q is the thickness divided by the lateral length of a square film.

## 5.6. Vortex Direction Transition

For the descending field, the magnetization curves show strong remanent field. That is dramatically different from the measurements by SPNR, shown in Fig. 28. For uniform distribution of the vortices of a given density, the average

magnetization for H parallel to the film surface could be calculated, using Eqs. (4.12) and (4.13).

$$4\pi\vec{M}_{\parallel} = (\vec{H}_{\parallel} - \vec{\Phi}_o n_{\parallel}) \left\{ \frac{2\lambda_L}{t} \tanh\left(\frac{t}{2\lambda_L}\right) - 1 \right\} \dots\dots\dots (5.10)$$

where  $n_{\parallel}$  is laterally averaged vortex density for vortices parallel to the surface. Figure 32 (a) shows the magnetization calculated from the data of Fig. 28. As we expected, the average magnetizations for ascending and descending fields are quite similar. What can cause the difference between SQUID magnetization measurements and SPNR measurements?

The ascending field SPNR data can be quantitatively compared with the SQUID magnetization data in Fig. 32 (b). Here it was assumed that the magnetization measurements had a small sample tilt of  $0.12^\circ$ . A scale factor  $0.157 \pm 0.073$  (determined by matching the data at zero tilt angle in the inset to Fig. 31) was applied to account for the inaccuracy of getting an absolute magnetic moment from the SQUID [42] for ascending and descending fields. Both the SQUID and SPNR measurements suggest that the magnetization due to vortices as well as surface screening lie parallel to the film surface as the field is ascending.

The difference between the SQUID and SPNR measurements arises only for descending field. Given that the SQUID data is very sensitive to  $M_{\perp}$  and that the  $M_{\parallel}$  measured by SPNR is reversible, we conclude that the vortices rotate as the field is reduced. However we expect that vortices will either be parallel or perpendicular to the surface because intermediate angles have higher energy [27].



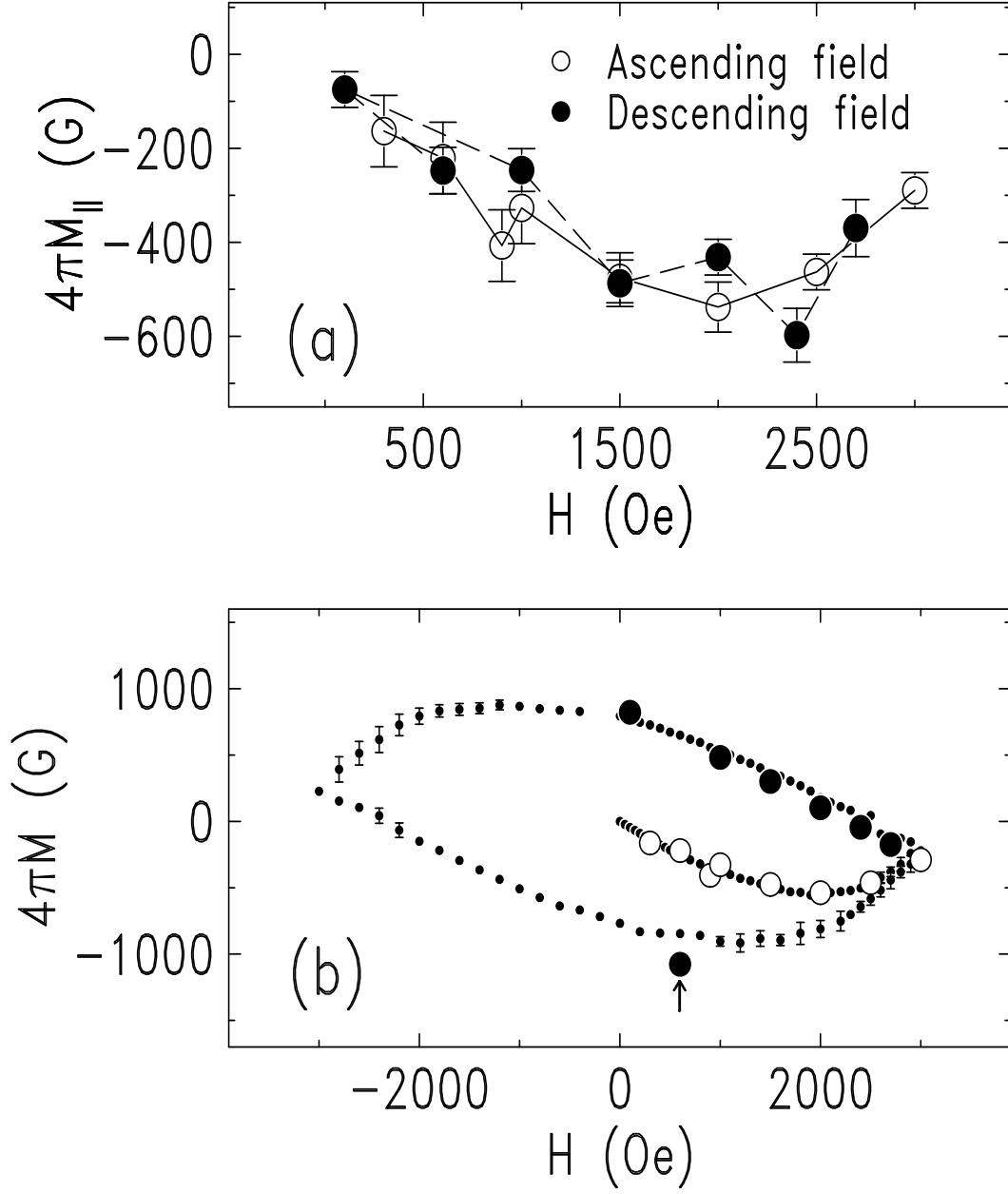


FIG. 32. (a) shows magnetization measured by SPNR. (b) the dotted line shows the measured magnetization by a SQUID magnetometer, open circle is the recalculated magnetization from the data in (a) for ascending field and closed circle is for descending field, assuming the vortex changing their direction perpendicular to the surface.

Therefore, as the field is reduced, we assume that a fraction of the vortices remain parallel to the surface and the other rotate out of the surface. Using this model, both data sets can be explained if it is assumed that the total stored magnetic field of the vortices obtained by linearly adding the parallel and perpendicular components is constant:  $n_{||max}\Phi_{eff} = n_{||}\Phi_{eff} + n_{\perp}\Phi_o$ , where  $n_{||max}$  is the vortex density at the maximum field and  $\Phi_{eff}$  is the average effective vortex flux quantum due to image vortices (discussed in Sec. 4.2.). Using Eq. (4.17) and assuming uniform distribution of vortices, the average effective vortex flux quantum  $\Phi_{eff}$  is calculated to  $0.37\Phi_o$  with  $\lambda_L$  490 Å.

$$\Phi_{eff} = \Phi_o \left\{ 1 - \frac{2\lambda_L}{t} \tanh(t/2\lambda_L) \right\} \dots\dots\dots (5.11)$$

Applying this to the SPNR data so that it matches the descending field SQUID data in Fig. 32 (b) yields the solid circles.

With assumed that the total magnetic field magnitude due to the vortices is conserved:  $(n_{||max}\Phi_{eff})^2 = (n_{||}\Phi_{eff})^2 + (n_{\perp}\Phi_o)^2$ , the calculated magnetization from the SPNR data for the decreasing field is shown in Fig. 33. For the calculation, the same scale factor and parameters used in Fig. 32 (b) was used but the tilt angle  $0.3^\circ$  was assumed. Figure 33 shows that near the maximum field, 3000 Oe, the calculated magnetization from the SPNR data do not match well the SQUID magnetization data.

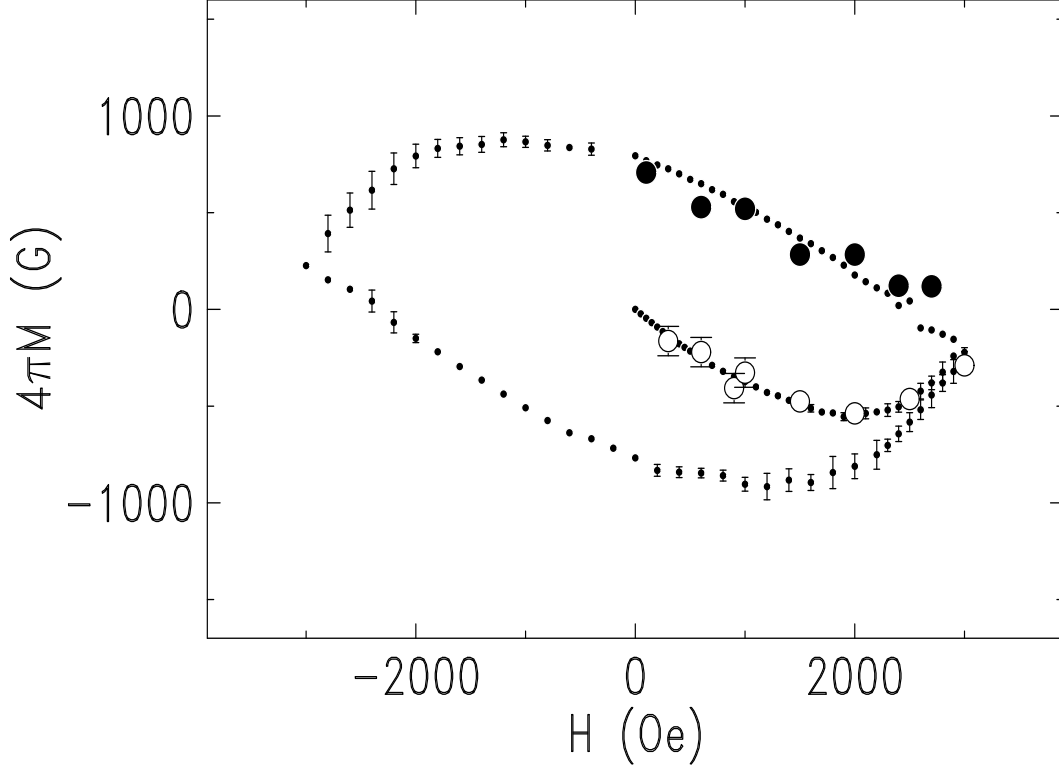


FIG. 33. The dotted line shows the measured magnetization by a SQUID magnetometer, open circle is the recalculated magnetization from the data in Fig. 32 (a) for ascending field and closed circle is for descending field, assuming that the total flux due to the vortices is constant and change their direction perpendicular to the surface.

Therefore we assumed that the total stored magnetic field due to the vortices is conserved,  $n_{||max}\Phi_{eff} = n_{||}\Phi_{eff} + n_{\perp}\Phi_o$ , and extracted the vortex density of the vortices perpendicular to the surface for the descending field from the data in Fig. 30. Figure 34 (a) shows the resulting vortex densities perpendicular and parallel to the surface for descending field.  $n_{||}$  is obtained from the SPNR data shown in Fig. 30 and  $n_{\perp}$  is calculated using  $n_{\perp}\Phi_o = \Phi_{eff}(n_{||max} - n_{||})$ . This magnetic field due to the vortices,  $0.37 n_{||}\Phi_o$  and  $n_{\perp}\Phi_o$ , has been used for the calculation (solid

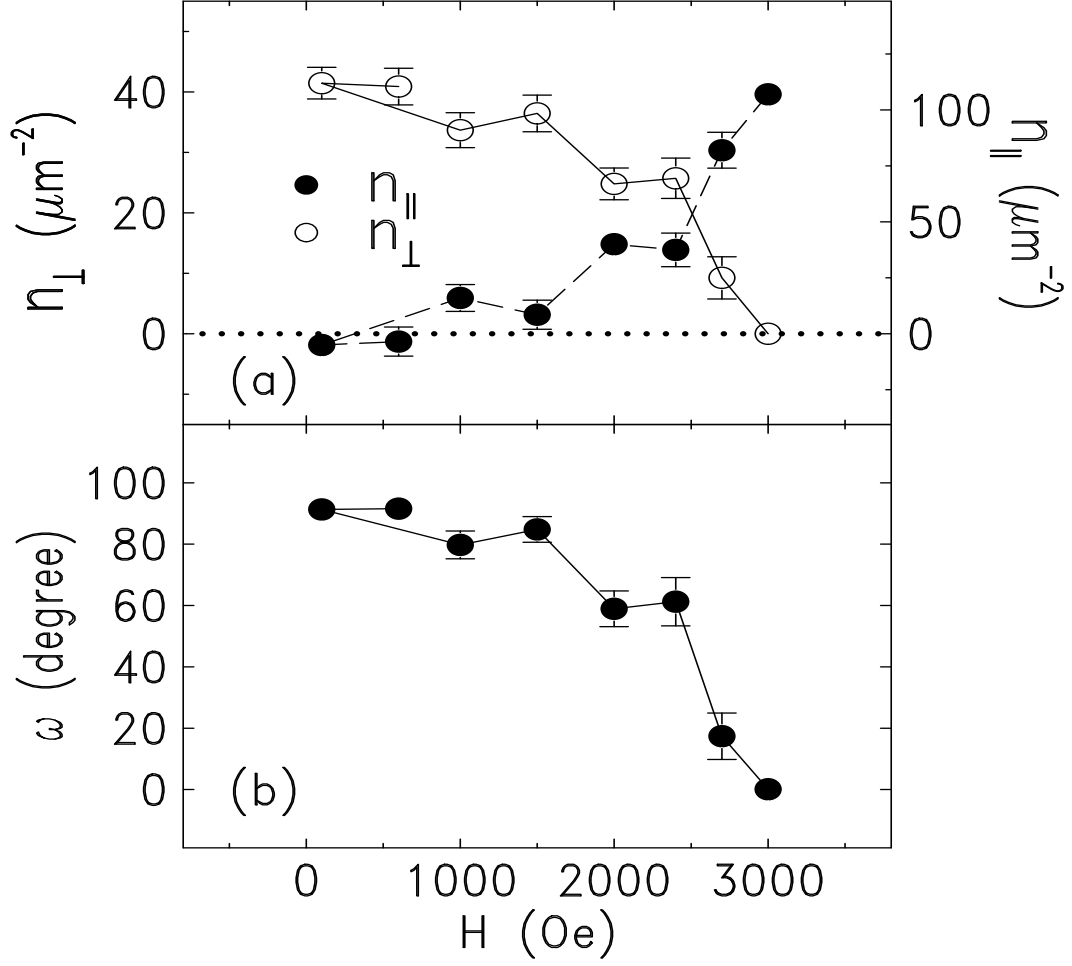


FIG. 34. (a) shows the extracted vortex density running perpendicular (open circle) and parallel (solid circle) to the surface, basing on the data in Fig. 30 (b). (b) shows the vortex angle,  $\omega = \tan^{-1}(n_{\perp}\Phi_o/n_{\parallel}\Phi_{eff})$ , as the applied field decreased from 3000 Oe to zero.

circle) shown in Fig. 32 (b). Figure 34 (b) shows the angle between the magnetic field of the vortices and the film plane,  $\omega = \tan^{-1}(n_{\perp}\Phi_o/n_{\parallel}\Phi_{eff})$ .

As the field is cycled to the minimum field -3000 Oe and to the maximum field 3000 Oe, the SQUID magnetization above 2700 Oe is identical to the zero

field cooled magnetization, as shown in Fig. 32 (b). It indicates that the vortices rotate perpendicular to the surface as field is reduced from the maximum field and retrace to the original orientation when the field approaches the maximum field. The vortex lattice in inclined fields has intensively studied (2H-NbSe<sub>2</sub>, Bi-Sr-Ca-Cu-O) [41]. They showed that the vortex density perpendicular to the film surface is proportional to the projection of the applied field. However with the applied field parallel to the surface, the vortices rotate depending on the field strength shown in Fig. 32 (b) that is first observed by us [25]. At 600 Oe after the field cycling to -3000 Oe, SPNR was measured. The magnetization calculated from the SPNR data is indicated by an arrow in Fig. 32 (b). In the calculation, the density of vortices at -3000 Oe was assumed to be the same to that at 3000 Oe however the direction is opposite. The agreement of SPNR and SQUID magnetization at 600 Oe suggests that the vortices at the minimum field run along the applied field (in film plane), anti-parallel to the maximum field. SPNR and SQUID magnetization measurements in Fig. 32 obviously demonstrate that the vortices take a turn with a step 90° while the field is cycling from 3000 Oe to -3000 Oe and to 3000 Oe.

As the applied field reduced after cycling to above  $H_{c1}$ , one can expect that vortices will exit if the vortex-vortex interaction is stronger than the pinning forces [34]. However, what we observe is that the vortices change orientation instead of exiting the superconductor. Previous studies have showed that the vortices follow the applied field [41]. Near the maximum field, we also observe that the vortices in a thin Nb film run parallel to the applied field. However the vortices are not along

the applied field when the field is smaller than the maximum field.

The observation of the vortex direction transition and demagnetization in a thin film is quite important. Once a vortex changes its direction out of the film surface, it will not be easily removed from the superconductor, although the field is cycled by applying positively and negatively several times that technique is generally used to remove a remanent field in a specimen. Also for the average magnetization studies in a thin film superconductor, particularly with a small tilt angle, the vortex direction transition and the demagnetization effect could not be ignored.



## 6. VORTEX LINE TRANSITION IN Nb/Al MULTILAYERED FILMS

### 6.1. Introduction

The interaction of vortices and the surface in a *thin-film* superconductor is an important subject for understanding the vortex pinning which is useful for practical application. A maximum in the magnetization curve just above  $H_{c1}$  was first observed by J. Guimpel *et al.* [20] in a  $[\text{Nb}(16.5\text{\AA})/\text{Cu}(16.5\text{\AA})]\times 250/\text{Al}_2\text{O}_3$  multilayer and a  $[\text{Nb}(54\text{\AA})/\text{Cu}(54\text{\AA})]\times 100/\text{Al}_2\text{O}_3$  multilayer by using SQUID magnetometer with the applied field parallel to the surface. They explained the maximum in terms of a vortex rearrangement, (into one line, two lines, etc.) and compared to a model calculation which minimized the Gibbs free energy. S. H. Brongersma *et al.* also studied the maxima in Nb/Cu multilayers, by using a torque magnetometer with applied field near parallel to the surface and reported the observation of several maxima in the magnetization curve. They also performed the results of Monte Carlo simulations in which they chose 60 vortices in a superconductor and allowed them to freely locate by minimizing the free energy under a given field [21]. The maxima, in a  $[\text{Nb}(100\text{\AA})/\text{Si}(15\text{\AA})]\times 20$  multilayer, was first found by S. M. Yusuf *et al.* with a SQUID magnetometer [23].

The above described techniques can measure only the average magnetization. Furthermore, with a torque magnetometry, one will measure only the mag-



netization which is perpendicular to applied field [21,26].

$$\vec{\tau} = \mu_o \vec{M} \times \vec{H} \dots \dots \dots (6.1)$$

It obviously shows that the magnetization should have a certain angle to applied field and the contribution of the perpendicular magnetization (even small amount) to the torque should not be neglected S. H. Brongersma *et al.* argued that with the applied field near parallel to the surface (for their measurements, the applied field 1° tilted to the sample surface), one can still study the vortex line transitions with torque measurements.

The vortices in a thin film under an applied field tilted to the surface are partial to staying nearly parallel or nearly perpendicular to the surface because intermediate angles will create extra free energy [27]. The vortex transition of its direction to the perpendicular to the surface (as we have seen in Nb described in Sec. 5.6) will considerably contribute to the measured magnetization even with the demagnetization.

We also have studied Nb/Al multilayered films by SQUID magnetization and spin-polarized neutron reflectivity (SPNR) measurements [24]. In the studies of SQUID magnetization measurements on the Nb/Al multilayers, we focused on the demagnetization effect and maxima in the hysteresis loop with different tilt angle in SQUID magnetization measurements. And we studied the distribution of vortices which run parallel to the interfaces by using SPNR.

## 6.2. Characterizations of Nb/Al Multilayered Films

Artificially layered structures, Nb / [Al(20Å) / Nb(70Å)]  $\times$  20, Nb / [Al(20Å) / Nb(100Å)]  $\times$  20 and Nb / [Al(20Å) / Nb(130Å)]  $\times$  20 were deposited on Si substrates (1" diameter and 0.25" thickness disks for the SPNR studies and around  $3.4 \times 6.7 \text{ mm}^2$  and thickness  $\sim 1\text{mm}$  chips for the SQUID magnetization studies) by direct-current sputtering under a base pressure of  $\sim 10^{-4}$  mTorr and the Ar partial pressure of 5 mTorr. During the deposition, the power was applied to a Nb target with 275 watts (297 voltage) and a Al target with 200 watts (372 voltage) at which the deposition rate was 5.9 Å / sec for Nb film and 4.7 Å / sec for Al film meanwhile the substrate was placed at the ambient temperature.  $T_c$  of an Nb / [Al(20Å) / Nb(70Å)]  $\times$  20 chip,  $7.25 \pm 0.25 \text{ K}$ , was found by the SQUID magnetization measurement under applied field 50 Oe. X-ray diffraction measurements was performed on the Nb / [Al(20Å) / Nb(70Å)]  $\times$  20 and the results is discussed in Sec. 7.5 in detail.

## 6.3. DC Magnetization in Nb/Al Multilayered Films

For DC magnetization measurements, a multilayer chip ( $\sim 3.4 \times 6.7 \text{ mm}^2$  and thickness  $\sim 1\text{mm}$ ) mounted on an extended sample holder was placed in a SQUID cryostat with the geometry where the surface normal is near perpendicular to a pick-up coil axis of the SQUID. Figure 35 shows the SQUID magnetization of the zero-field cooled specimens for ascending field. The arrows indicate the maxima

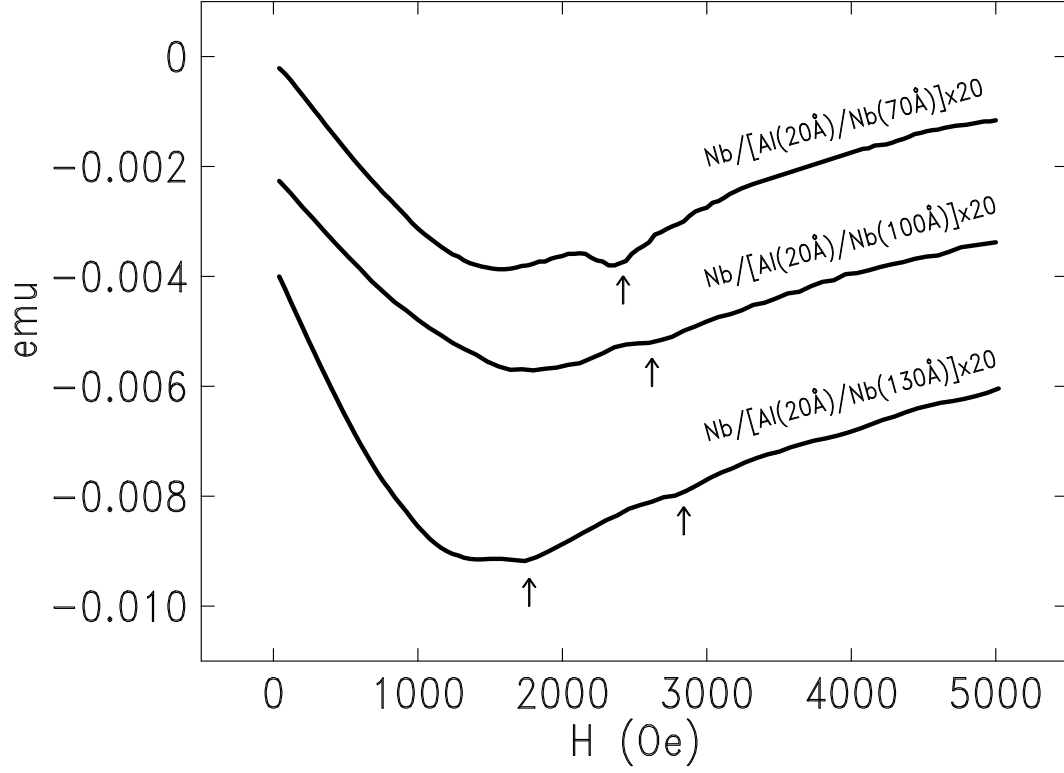


FIG. 35. Magnetizations as a function of applied field at 2.2 K were measured on Nb/Al multilayers by a SQUID magnetometer. The field was applied parallel to the surface. The arrows indicate maxima.

TABLE II. The maximum positions vs. Nb thickness

Nb thickness(Å)	1st maximum position(Oe)	2nd maximum position(Oe)
70	950	2350
100	1360	2640
130	1740	2780

which might be due to the vortex line transitions. In Fig. 35, the maximum in the Nb / [Al(20Å) / Nb(70Å)] film was located at  $\sim 2350$  Oe. That might be the second maximum, compared with Fig. 37 where the first maximum was shown at 950 Oe. The reason for the missing first maximum will be discussed later. Table II shows the maximum positions in the magnetization curve as a function of the Nb layer thickness.

Near  $H_{c1}$ , small number of vortices would enter the superconductor and stay in the middle line of a film because of the surface screening force, as discussed in Ch. 2. With the field increasing, the number of vortices will be grown and their interaction energy would be larger. Therefore they will stay in two rows instead of a single row in the film [20,?]. In that case, they could reduce the interaction energy because they stay at longer distance each other and the effective flux quantum of each vortex could be reduced for the shorter distance between a vortex and the surface.

The average effective flux quantum can be calculated using Eq. (4.17) with  $D(z') = \delta(z')$  for vortices located in a line.

$$\begin{aligned} \frac{\Phi_{eff}(z')}{\Phi_o} &= \frac{1}{2\lambda_L} \int_{-t/2}^{t/2} \left\{ e^{-\frac{|z-z'|}{\lambda_L}} - e^{\frac{z-t/2}{\lambda_L}} \frac{\sinh(\frac{z'+t/2}{\lambda_L})}{\sinh(\frac{t}{\lambda_L})} + e^{-(\frac{z+t/2}{\lambda_L})} \frac{\sinh(\frac{z'-t/2}{\lambda_L})}{\sinh(\frac{t}{\lambda_L})} \right\} dz \\ &= \left\{ 1 - e^{-t/2\lambda_L} \cosh\left(\frac{z'}{\lambda_L}\right) \right\} \\ &+ \frac{e^{-t/2\lambda_L}}{2\cosh(t/2\lambda_L)} \left\{ \sinh\left(\frac{2z'-t}{2\lambda_L}\right) - \sinh\left(\frac{2z'+t}{2\lambda_L}\right) \right\} \dots\dots\dots (6.2) \end{aligned}$$

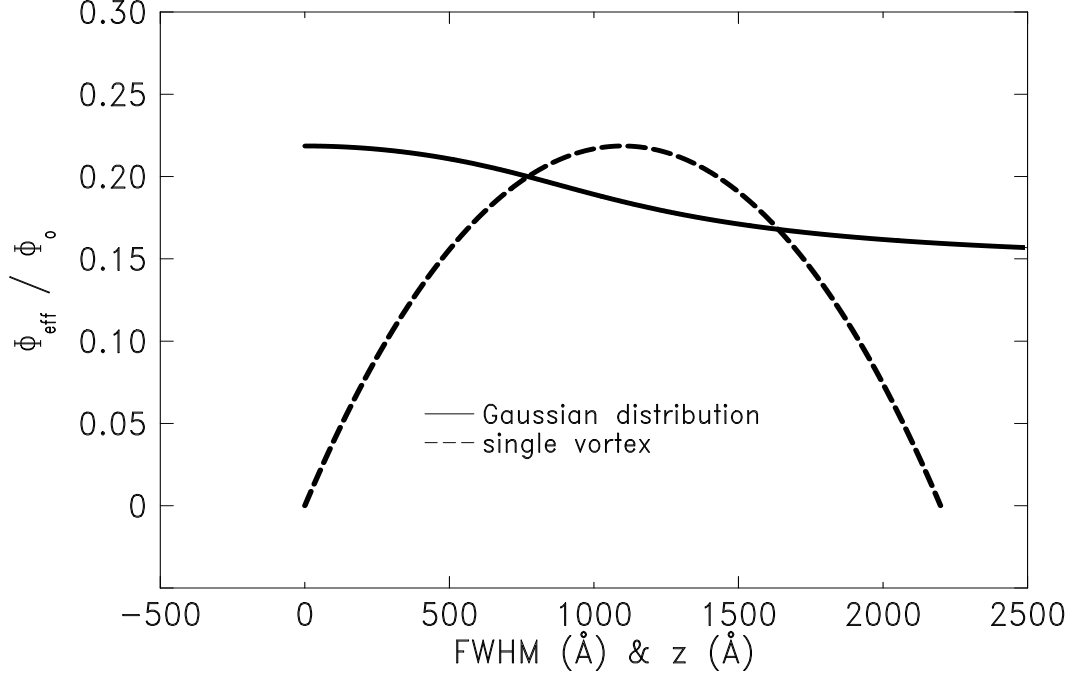


FIG. 36. Effective flux quantum was calculated as a function of vortex core position for a single vortex (dashed line) and FWHM of a Gaussian distribution of vortices (solid line), assuming  $\lambda_L = 1500 \text{ \AA}$  and film thickness  $2200 \text{ \AA}$ .

where  $z'$  is the position of the vortex core. This equation shows that the effective flux quantum in a film depends on the film thickness and the magnetic screening length as well as the position of vortex core. In Fig 36, the dashed line shows the effective flux as a function of a vortex core position and the solid line presents the average effective flux as a function of full width at the half maximum with assuming a Gaussian distribution of vortices. At the interfaces, the effective flux is vanished. As the vortex core moves to the middle line of the film, the effective flux is maximum. As the vortices change from one row (vortex line position at  $1100 \text{ \AA}$ ) to two rows (vortex line positions at  $733 \text{ \AA}$  and  $1467 \text{ \AA}$ ), the effective flux will be

reduced by 13 % with assuming the magnetic screening length 1500 Å and the film thickness 2200 Å, as shown in Fig. 36. The difference of the effective flux quantum between a single row and two rows for a same vortex density generates the first maximum in a magnetization curve, the second maximum due to two row vortices changing into three row vortices and so on.

We have studied the magnetization at two temperatures, 2 K and 4.5 K. The locations of the maxima scarcely depend on temperature, similar to previous works [23,21]. As temperature is increased, the screening length and coherence length will be longer. The interaction of vortex-surface as well as the interaction of vortex-vortex will be weaker with increasing temperature. The compensation of the two force might be ascribed by near the same maximum position under different temperature. However, with different film thickness, different number of vortices could sit on a row even with the same  $\lambda_L$  and  $\xi$ . Therefore, the locations of maxima would be different depending on the film thickness and its characteristic lengths,  $\lambda_L$  and  $\xi$ .

Figure 35 shows that not only the maximum positions but also the size of the maxima depends on films. By using Eq. (6.2), with the magnetic screening length 1500 Å, the field observed for the transition of one row to two rows, the effective flux difference is calculated to be 11% (effective flux from  $0.1795\Phi_o$  to  $0.16\Phi_o$ ) for  $\text{Nb}(150\text{Å}) / [\text{Al}(20\text{Å}) / \text{Nb}(70\text{Å})] \times 20$ , 10.47% (effective flux from  $0.277\Phi_o$  to  $0.248\Phi_o$ ) for  $\text{Nb}(150\text{Å}) / [\text{Al}(20\text{Å}) / \text{Nb}(100\text{Å})] \times 20$  and 10.2% (effective flux  $0.3765\Phi_o$  to  $0.338\Phi_o$ ) for  $\text{Nb}(150\text{Å}) / [\text{Al}(20\text{Å}) / \text{Nb}(130\text{Å})] \times 20$ . With

the Nb(150Å) / [Al(20Å) / Nb(70Å)]  $\times$  20 film, the effective flux difference for the transition from one row to two rows is calculated to be 10.6% (effective flux from  $0.34\Phi_o$  to  $0.304\Phi_o$ ) for  $\lambda_L$  1000 Å and 8.33% (effective flux from  $0.72\Phi_o$  to  $0.66\Phi_o$ ) for  $\lambda_L$  500 Å. It shows that the maxima could be more clearly observed in a thinner film and with a longer magnetic screening length. However, that differences (a few percent) from the calculations is not enough to explain the size difference of the maxima depending on films shown in Fig. 36. The small size of the maxima on the magnetization curve of the Nb(150Å) / [Al(20Å) / Nb(130Å)]  $\times$  20 film might suggest that some vortices were not in a line because of relatively weaker pinning centers, relatively less Al in the film.

SQUID magnetizations measured on the Nb / [Al(20Å) / Nb(70Å)]  $\times$  20 specimen at different tilt angle between the applied field and the sample surface are shown in Fig. 37. In Fig. 37, the distinguishable features between two curves are that  $H_{c1}$  where the magnetization is minimum is shifted and also the magnetic moment and the maximum positions are different depending on tilt angle.  $H_{c1}$  shifted and the different magnetic moments are discussed with demagnetization factor in Sec. 5.4 in detail. In this chapter, I will focus on the maxima.

The magnetization curve for zero tilt does not exhibit the first maximum, compared with the magnetization curve measured at a tilt angle. Under tilt field, vortices enter the film at rather small field because the perpendicular component of the applied field helps the vortex entrance. And they might run parallel to the surface or perpendicular to the surface because at an intermediate angle, they will

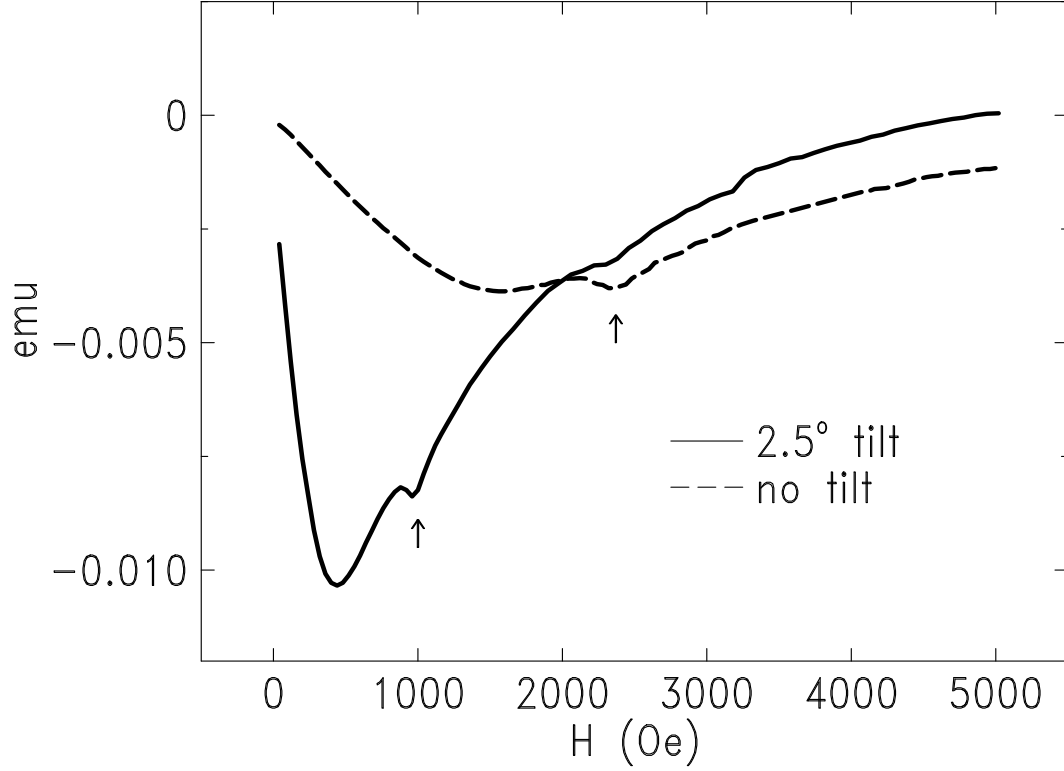


FIG. 37. SQUID magnetic moment was measured at two different tilt angles. The arrows indicate the maxima.

create an extra free energy [27]. Here, I concern only the vortices running parallel to the surface. Near  $H_{c1}$  small number of vortices will enter and stay in the middle of the film because of the surface screening force and relatively weak interaction force between vortices. As the field increases, the number of vortices increases and at a certain point, the vortices would stay in two rows instead of one row to reduce the interaction energy between vortices [20,21]. When the film surface is placed parallel to the applied field, vortices should not enter a *thin-film* superconductor at a small field because of the surface barrier. Once the vortices overcome the surface barrier, many vortices will immediately enter the superconductor because



the superconductor needs a certain amount of vortices to keep it in superconducting state with an applied field [5]. However, the number of vortices are too large to stay in a single row. Therefore they would stay in at least two lines. That might be the explanation of which the second maximum position in a tilt field is near the same to the first maximum position under no tilt angle. The first maximum of 950 Oe could not be observed under small tilt angle  $< 1^\circ$ . At the tile angle  $\sim 2.5^\circ$ , the first maximum was more clearly observed than under other angles.

The slope below  $H_{c1}$  at which the vortices first enter the superconductor is different depending on tilt angle. Figures 38 shows the measurements of the slope as a function of tilt angle at 2 K and 4.5 K. The solid lines are a best fit to a model calculation with counting the demagnetization effect which was discussed in Sec. 5.4. The fit shows the demagnetization factors of  $0.9986 \pm 0.0011$  at 2 K and  $0.9935 \pm 0.0007$  at 4.5 K which can be compared with 0.9993 for 2 K and 0.9942 for 4.5 K. The demagnetization factor was calculated with assuming a square film, using Eq. (5.9).

The studies of the demagnetization in a superconductor under the geometry of applied field near parallel to surface is very important for understanding the magnetization measurement because  $M_\perp$  is large as well as contributes to the magnetization measured by a SQUID magnetometer. It is possible that the maxima were dominantly determined by the kind of direction transition that was found in Nb [25] instead of the line transition of vortices. The maxima would be affected by  $M_\perp$ . For a long length of vortices in a thin film, one can easily assume the flux

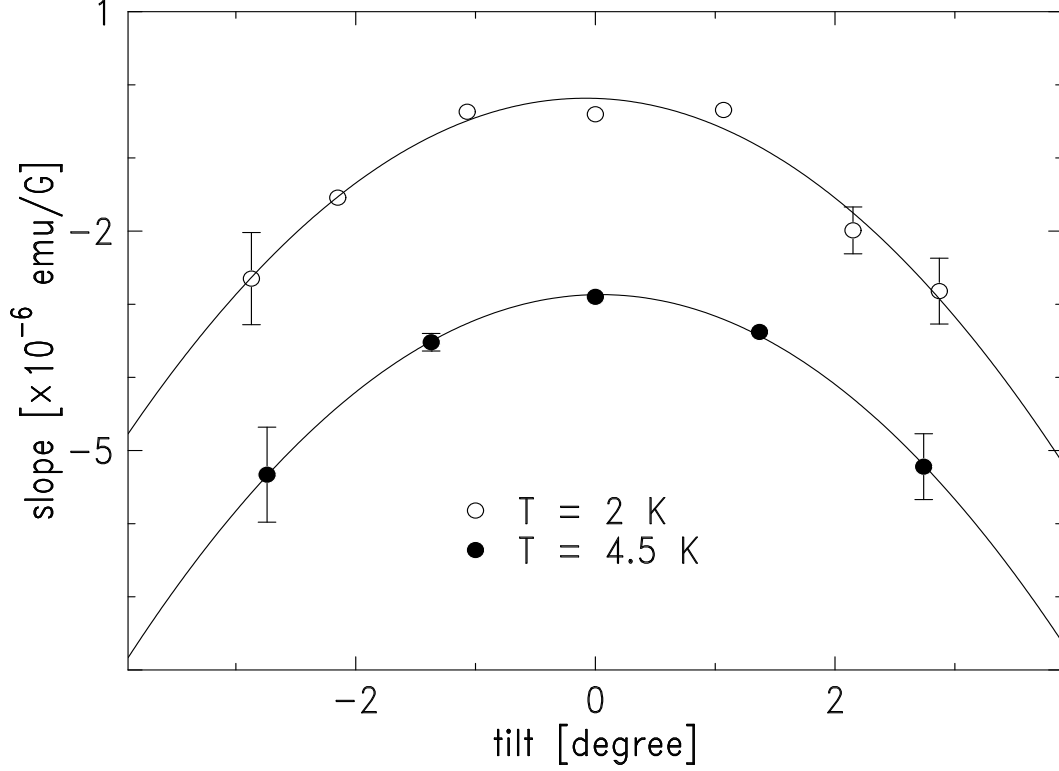


FIG. 38. The magnetization slopes below  $H_{c1}$  were measured as a function of tilt angle at 2 K and 4.5 K. The data of 4.5 K was intentionally shifted down. The solid lines are a best fit to the model calculation described in Sec. 5.4.

lines are cut and the end of the flux lines come out through the film surface [27].

As the vortex lines break to several pieces at a certain field, the ends of the broken vortices running perpendicular to the surface will considerably affect the magnetization measured by a SQUID magnetometer. Therefore we really need the measurements for the spatial distribution of vortices which run parallel to surface and SPNR would be a promising tool for the studies. Then which field will give the best condition to observe the vortex line transition?

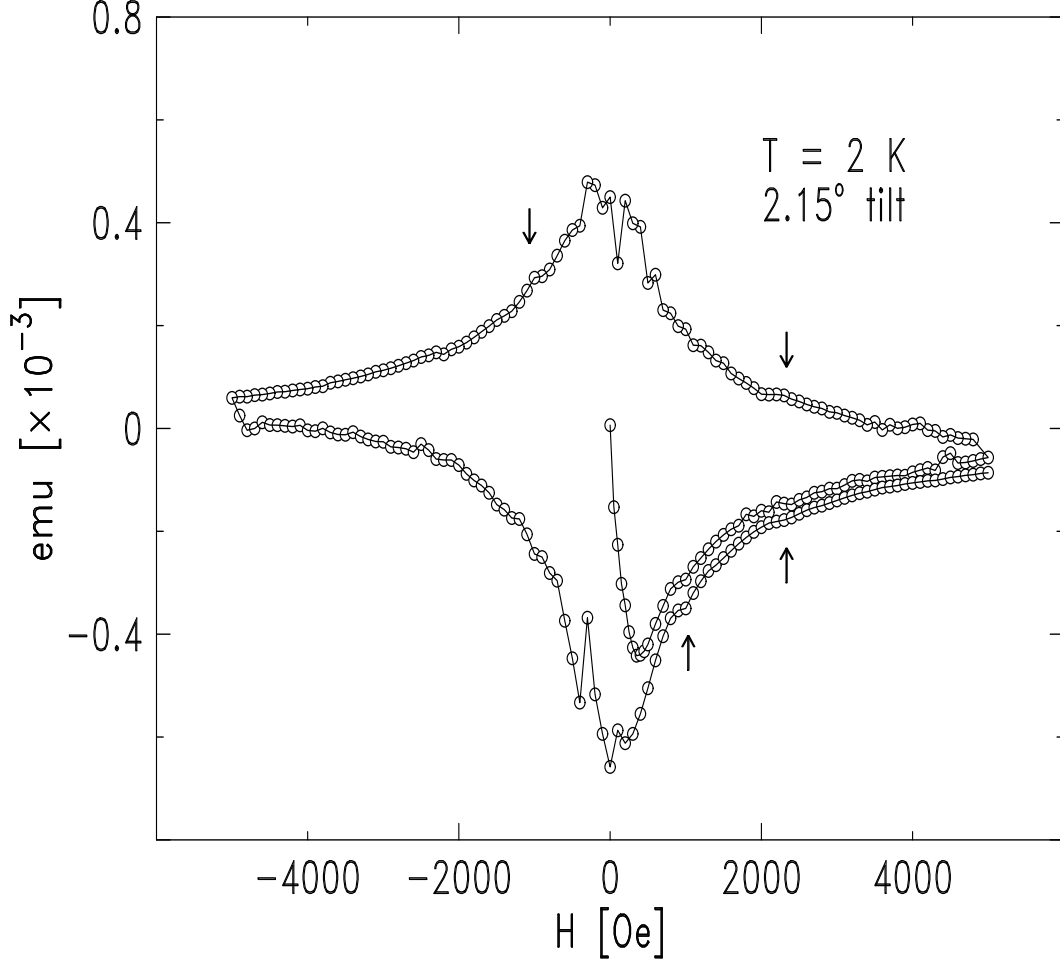


FIG. 39. Hysteresis loop was measured on a Nb / $[Al(20\text{\AA}) / Nb(70\text{\AA})] \times 20$  multilayer at 2 K with tilt angle of  $2.15^\circ$ . The arrows indicate the positions of the maxima and the solid line is for a guide to the eye.

Figure 39 shows the hysteresis loop measured a  $3.2 \times 3.4 \text{ mm}^2$  Nb / $[Al(20\text{\AA}) / Nb(70\text{\AA})] \times 20$  at 2 K under applied field tilted  $2.15^\circ$  to the film surface. The arrows indicate the maxima. From 0 Oe to 5400 Oe, two maxima were observed. The first maximum could be corresponding to the vortex line transition of single line to double lines and the second maximum could be due to the vortex line

changing from double lines to triple lines. For the descending field after cycling to 5400 Oe, the maxima were observed at  $\sim 2300$  Oe and -1100 Oe which were reproducible. For the ascending field after cycling to -5400 Oe, the maxima at 950 Oe and 2400 Oe were observed. In the fourth quadrant, the magnetization curves were quite similar without depending on an initial condition, zero-field cooled or training to -5400 Oe, except  $H < H_{c1}$ . That might suggest that for  $H > H_{c1}$ , vortices which run parallel or perpendicular to the surface are independent on the initial condition, zero-field cooled or trained by a field. With the SQUID magnetization measurements alone, understanding the maxima in the magnetization curve for the descending field is slightly difficult because the perpendicular as well as parallel component of magnetization contributes to the measured magnetization. The loop shows that for the studies of the vortex line transition, the parallel magnetization would be measured at zero-field cooled  $H_{c1} < H < H_{c2}$  or after the field cycling to the negative below  $H_{c1}$ .

#### 6.4. SPNR from a Nb/Al Multilayered Film

Spin-polarized neutron reflectivity (SPNR) measurements on a Nb/[Al(20 Å)/Nb(70 Å)]  $\times$  20 /Si disk (1" diameter and 0.25" thickness) was performed on the POSY1 reflectometer at Intense Pulsed Neutron Source at Argonne National Laboratory. The polarization efficiency was 85 % and the instrumental resolution,  $\Delta q / q = 0.053$ , of the incident beam was used to analyze the SPNR data. The specimen was zero-field cooled in a cryostat and applied field near parallel ( $< 0.5^\circ$ )

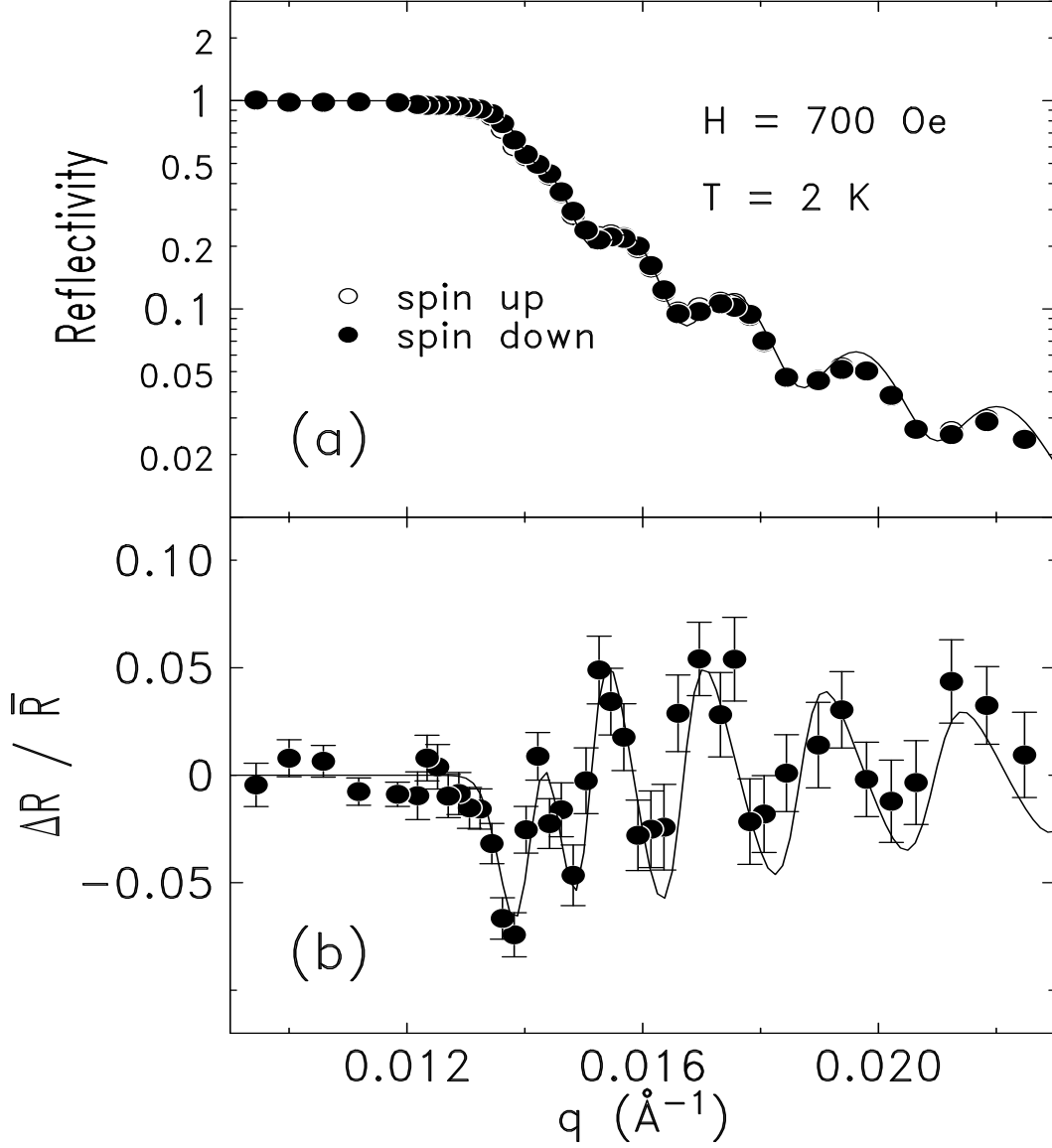


FIG. 40. (a) shows the grazing neutron reflectivity from a Nb(180Å) / [Al(20Å) / Nb(72Å)]  $\times$  20 / Si film measured as a function of  $q$  at 2 K and 700 Oe. The solid line is a best fit. (b) shows the normalized reflectivity difference for spin up and spin down neutrons obtained from the data in (a). The solid line is a best fit and gives  $\lambda_L$   $1500 \pm 200 \text{ \AA}$ .

to the surface by an electromagnet. The polarized neutrons were reflected from the

surface of film with an incident angle  $0.225^\circ$ .

The grazing angle neutron reflectivities measured for spin up and spin down neutrons from the multilayer at 700 Oe and 2 K are shown in Fig. 40 (a). The oscillation period is corresponded to the total film thickness 2000 Å. The solid line, best fit, shows that the top Nb layer thickness is  $180 \pm 40$  Å and multilayer  $[\text{Al}(20 \pm 2\text{Å}) / \text{Nb}(72 \pm 5\text{Å})] \times 20$  which is consistent with the X-ray reflectivity measurements shown in Fig. 54. However it does not give the information of the interface of Al/Nb because the reflectivity was measured at small  $q$ . Figure 40 (b) shows the normalized reflectivity difference which more clearly demonstrates the magnetization contribution to SPNR. The solid line is a best fit without including vortices in the magnetization of the film. From the fit, the magnetic screening length  $1500 \pm 200$  Å was determined.

In Fig. 37, one can see that at 700 Oe, vortex contribution to the magnetization would be negligible for the untilted the specimen. Based on Fig. 37, the lower critical field,  $H_{c1}$ , could be determined to  $1200 \pm 100$  where there is no tilt. Given the London penetration depth and  $H_{c1}$ , the coherence length of the superconductor,  $\xi = 52 \pm 13$  Å is calculated using Eq. (5.2). With the coherence length, the  $H_{c2}$  of the superconductor,  $\Phi_o / 2 \pi \xi^2$ , which is predicted by the Ginzburg-Landau theory is calculated to be  $\sim 12$  Tesla.

Figure 41 (a) shows the polarization measured at 1500 Oe. The dashed line is a best fit assuming a single row of vortices and vortex density  $28 \mu m^{-2}$ . The

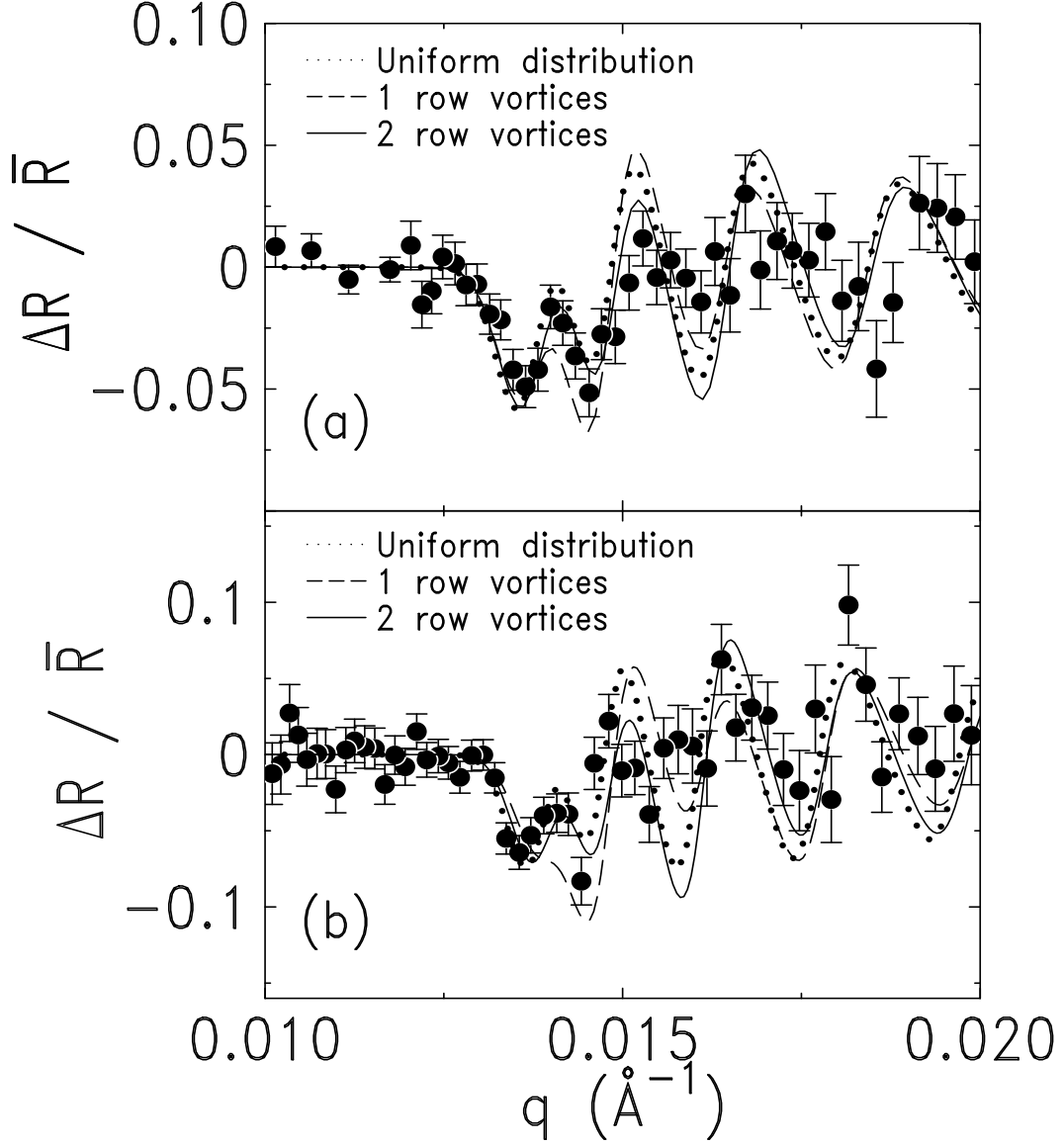


FIG. 41. The polarizations were measured at zero-field cooled 1500 Oe (a), 2000 Oe (b) and 2 K on a Nb(70Å) /Al(20Å) multilayer. The lines are a best fit with assuming different distribution of vortices and the magnetic screening length 1500 Å.

solid line is a best fit assuming the vortices staying in two rows and shows the density of vortices  $28 \mu m^{-2}$ . The dotted line is a best fit assuming vortices distributed uniformly through the specimen and shows the density of vortices  $38 \mu m^{-2}$ . The

difference is not large. However the fit with assumption of two rows of vortices might be better than others. Figure 41 (b) shows the polarization measured at 2000 Oe. The dashed line is a best fit assuming a single row of vortices and vortex density  $45 \mu m^{-2}$ . The solid line is a best fit assuming two rows of vortices and vortex density  $45 \mu m^{-2}$ . The dotted line is a best fit assuming vortices distributed uniformly through the specimen and shows the density of vortices  $60 \mu m^{-2}$ . The difference between 2 row vortices and uniform distribution of vortices is not large but with assumption of a single row of vortices the theoretical model could not fit the data well.

For the descending field after cycling to 5400 Oe, a magnetization maximum was observed at 2350 Oe, as shown in Fig. 39. The SPNR measured at 2 K and 2000 Oe after cycling the field 5400 Oe is shown in Fig. 42. The solid line is a best fit, assuming a Gaussian distribution of vortices with the full widths at half maximum (FWHM)  $400 \pm 200 \text{ \AA}$ . The fit shows the density of vortices  $53 \pm 2 \mu m^{-2}$ . The dotted line is a best fit assuming the uniform distribution of vortices and with a density of vortices  $60 \mu m^{-2}$ . It clearly demonstrates the vortices are localized near the middle of the film rather than uniformly distributed through the specimen. The maximum applied field 0.54 T is considerably smaller than the higher critical field ( $30.4 \pm 27.6 \text{ Tesla}$ ) of the superconductor. However it is high enough for a large number of vortices to enter the superconductor, as shown in the SQUID magnetization measurements. As the field reduced to 2000 Oe, the vortices might leave or they might rotate as observed in Nb.



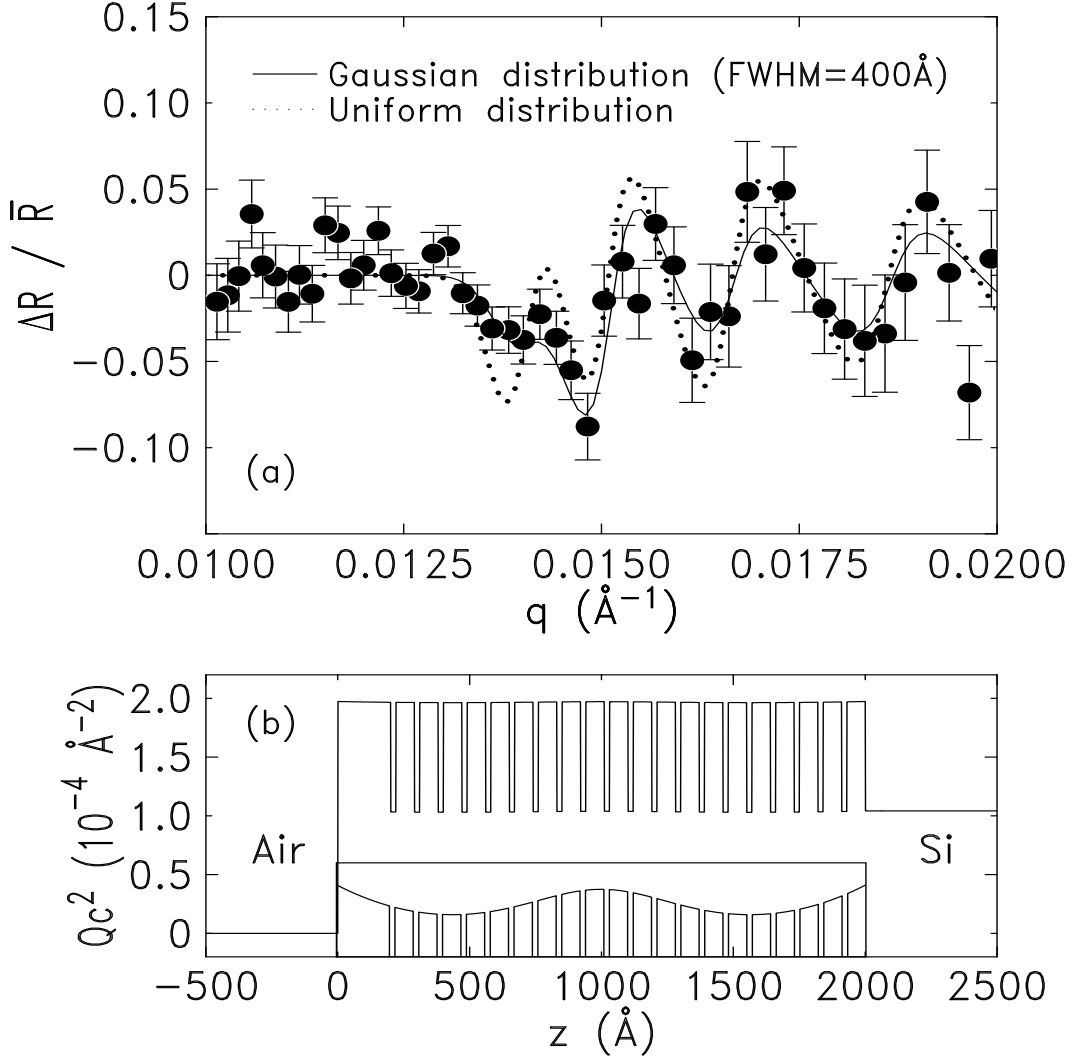


FIG. 42. (a) shows the polarization at 2000 Oe and 2 K after the field cycling to 5400 Oe. The curves are for a Gaussian distribution of vortices with FWHM 400  $\text{\AA}$  (solid line) and a uniform distribution of vortices (dotted line). (b) shows the scattering density profile corresponding to the solid line in (a) for spin-up neutrons as a function of position. The inset is a vertical expansion.

With the given vortex density  $53 \mu m^{-2}$ , the Gaussian distribution of vortices (FWHM = 400  $\text{\AA}$ ), the magnetic screening length 1500  $\text{\AA}$  and the film thickness

2000 Å, the average magnetization of the film would be calculated to -51.8 G which is different from the magnetization measured by a SQUID. The SQUID magnetization shows the positive magnetization for the descending field. The origin of the difference could be due to the vortex direction transition for the descending field, as discussed in Sec. 5.6.

We have observed the maxima in SQUID magnetization curve from Nb/Al multilayer films. The SQUID magnetization measurements are considerably sensitive to the tilt angle between the film surface and applied field because of demagnetization effect. As the applied field being close to parallel  $< 0.5^\circ$ , the first maximum was not observed. That might suggested that vortices could not enter the superconducting film because of the surface barrier. However in a tilt field, the perpendicular component of the applied field helps for vortices entering. Therefore, vortices could enter the superconductor at rather smaller field under tilt angle. SPNR could not be done at a tilt field (at the first maximum). SPNR at 1500 Oe suggested that the vortex distribution is close to two vortex rows or uniform distribution of vortices whereas the SQUID magnetization measurement with untilted field 2 rows of vortices. At 2000 Oe after cycling to 5400 Oe, SPNR suggested that most of vortices are located in the middle of the specimen with FWHM 400 Å of a Gaussian distribution whereas SQUID magnetization shows a maximum which might be related a vortex line transition.



## 7. X-RAY SCATTERING STUDIES ON THIN FILMS

### 7.1. General Introduction of Reflectivity

When a wave propagates through interface, the flux will be partially reflected from the surface and the rest will transmit, if the energy of the incident beam is higher than the optical potential barrier. Reflectivity is sensitive to an interface and an optical potential of material. The measured specular reflectivity is the integral over all beams that satisfy the reflection condition of which only the momentum perpendicular to surface is transferred during the scattering process. Therefore, reflectivity will give the information of one-dimensional optical potential as a function of position parallel to the momentum transfer direction. For a given optical potential, a 1-D Schrödinger equation could be analytically solved [44] for the smooth surface. Above the critical angle below which the beam is totally reflected by the surface, the reflectivity falls, following  $q^{-4}$  [45], where  $q = 4\pi \sin \theta / \lambda$ .

However, there is surface roughness at a practical interface. X-ray and neutron reflectivity have capability to study a buried interface without destroying a specimen. Particularly, x-ray reflectivity is considerably sensitive to the surface roughness. Fig. 44 shows the reflectivity from a 2500 Å thick  $\text{YBa}_2\text{Cu}_3\text{O}_{7-x}$  (YBCO) superconductor. The reflectivity falls sharply near the critical angle,  $2\theta \sim 0.32^\circ$ , because of the surface roughness. For a best fit (solid line) to a

reflectivity model [44], the distorted-wave Born approximation (DWBA) was used to treat the surface roughness problem. With a Gaussian distribution of the surface height (actually, it is the root-mean-square slope) for the rough surface, the reflectivity [45] will be

$$R_f = R_o e^{-\frac{\sigma^2 q_z^2}{2}} \dots\dots\dots (7.1)$$

where  $R_o$  is the reflectivity from the smooth surface and  $\sigma$  is the root-mean-square (rms) roughness. It shows the sensitivity of x-ray reflection on the surface roughness.

There is a different way to describe the surface roughness using a multi-sliced method. Over the length scale of surface roughness, the scattering density is gradually changed as a function of position at most of interfaces. One can chop the scattering density profile along the position by a thin slice and assume that the scattering density is constant within the slice. Figure 43 shows a normalized scattering density profile; dashed line is for a smooth real interface and solid line shows the chopped steps. For a Gaussian distribution of surface height at an interface, the scattering density could be calculated as a function of position.

$$Q_c^2(z) = Q_{c1}^2 + (Q_{c1}^2 - Q_{c2}^2) \times \frac{1 + \text{erf}(z/\sqrt{2}\sigma)}{2} \dots\dots\dots (7.2)$$

where  $Q_{c1}^2$  and  $Q_{c2}^2$  are scattering densities,  $\text{erf}()$  is an error integral and  $\sigma$  is rms surface roughness.

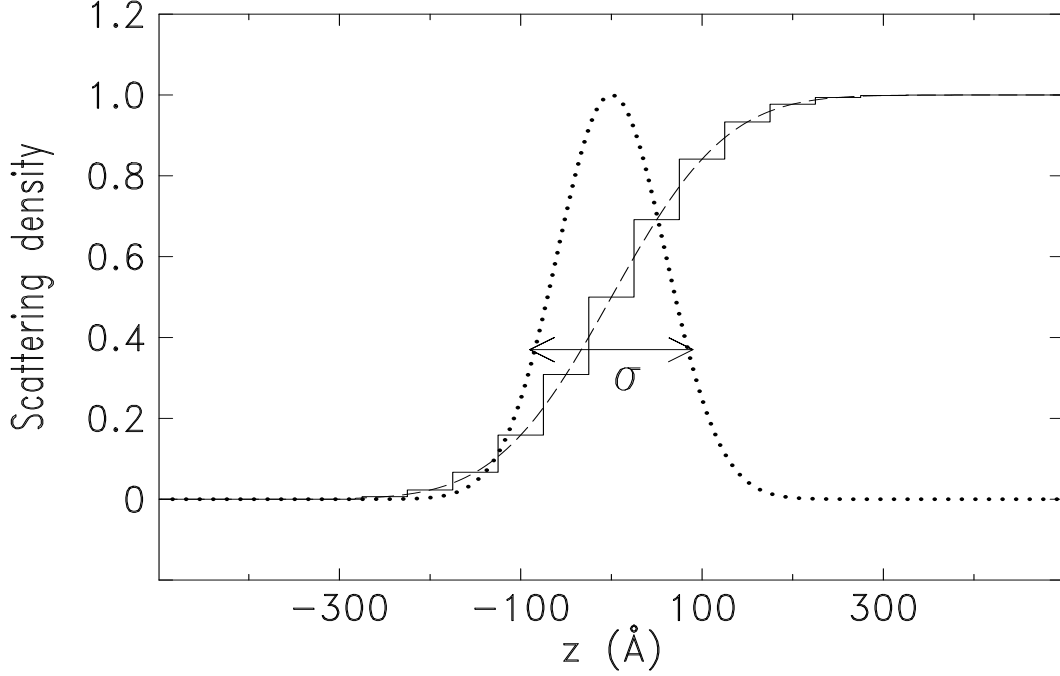


FIG. 43. Normalized scattering density profile for a Gaussian distribution of surface high. Solid line shows slices in multi-sliced method.

DWBA method to treat the surface roughness is simple and the calculation by a computer is fast because of only a single interface added for one more layer. However as the scattering density is changing with position, such as spin-polarized neutron reflectivity from a thin superconducting film, DWBA method could not be applicable because the scattering density is not constant within the superconducting film whereas multi-sliced method is considerably useful for the reflectivity calculation with the spatially varying scattering density profile. However the calculation by a computer with multi-sliced method would take much longer than with DWBA method.

X-ray reflectivity is a convenient tool to study interfaces. For x-ray scatter-

ing studies, the Mo  $K_{\alpha 1}$ , wave length 0.70926 Å, which was obtained by reflecting from a Ge(111) monochromator after radiating from a rotating anode line beam x-ray generator was used. The incident and exiting beam angular divergence was around  $0.005^\circ$  and the beam size at the sample position was 0.15 mm. The distance from the x-ray source to the sample position is  $\sim 1$  m and the distance of the sample position to a detector was  $\sim 1$  m. A guard slit 0.3 mm was located just after the sample position to reduce the back ground and another 0.3 mm slit was placed at the detector. The measurements were performed at the room temperature and atmosphere.

## 7.2. X-ray Diffraction from $\text{YBa}_2\text{Cu}_3\text{O}_{7-x}$

YBCO superconductor has been widely attractive by people for its application as well as academic research because of the high critical temperature,  $\sim 90$  K [46], the high upper critical field  $\sim 230$  T [9], and the intrinsic strong vortex pinning at high field [46,9]. People have studied the surface phenomena, such as, London penetration depth [6–8], Josephson tunneling [47] and proximity coupling [64], with this material. However, the surface of YBCO superconductor could not be studied by x-ray reflectivity very much [48] because of surface roughness. Modern growth techniques could fabricate rather smooth surface of a thin film [49,36,50] and also modern analysis facilities have helped to understand the surface of YBCO [38,48,51,52].

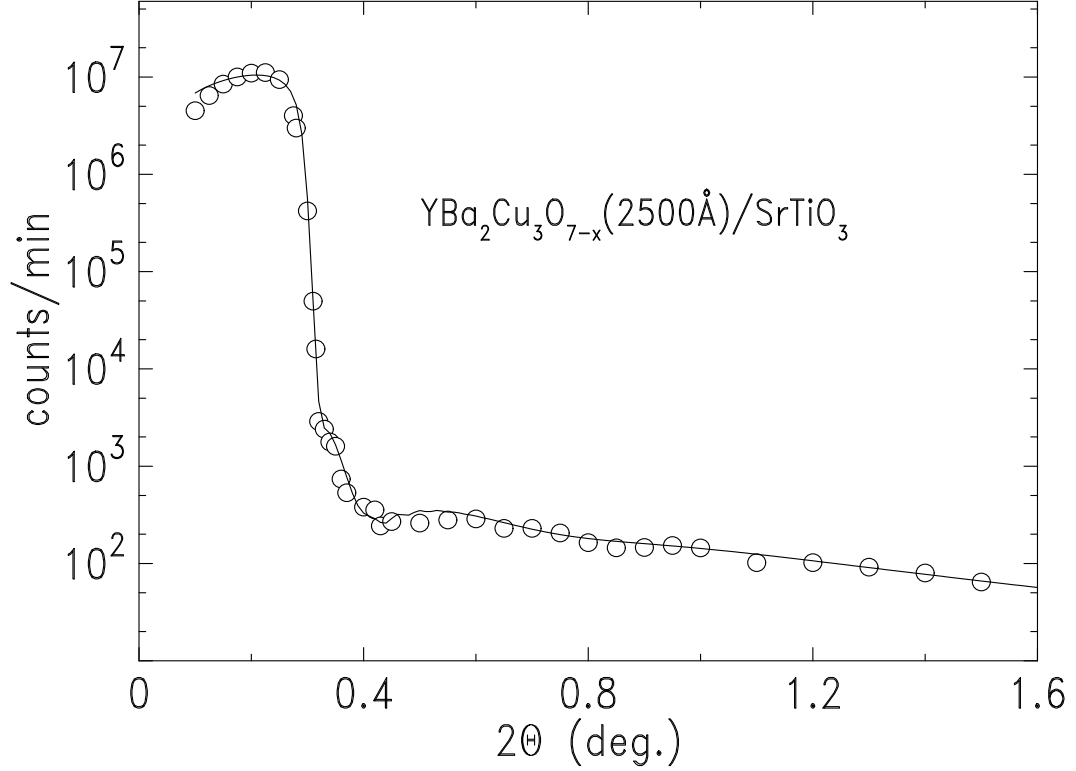


FIG. 44. X-ray reflectivity was measured on a YBCO(2500Å) /SrTiO<sub>3</sub> film vs.  $2\theta$ . The solid curve is a best fit.

#### 7.2.1. YBCO(2500Å)/SrTiO<sub>3</sub> by PLD

The Ag-doped YBCO film was deposited on a (001) SrTiO<sub>3</sub> substrate by D. H. Lowndes's group at the Oak Ridge National Laboratory with pulsed laser deposition [49]. During the deposition, the substrate temperature was held at 750 °C and the oxygen partial pressure was 200 mTorr.

The interface at air/YBCO was studied by x-ray specular reflectivity [38]. Figure 44 shows the grazing angle x-ray specular reflectivity from a 2500 Å thick



YBCO on SrTiO<sub>3</sub>. The solid line is a best fit to a x-ray reflectivity model [44]. From the fit a rms surface roughness of  $60 \pm 20$  Å was found and a  $\sim 100$  Å thick low scattering density layer at the interface of air/YBCO makes the better fit to the data. It might suggest that an oxide layer has been developed after the YBCO film was exposed to air. Just above the critical angle ( $2\theta_c \simeq 0.32^\circ$ ), the reflectivity dropped down sharply because of the surface roughness. At higher angles, the small amplitude intensity oscillations which is corresponding to  $40 \pm 10$  Å suggested that an additional layer is present between YBCO film and the substrate. The scattering density of the middle layer is slightly higher than YBCO. The surface roughness of the substrate was  $\sim 3$  Å was found from the best fit.

Figure 45 shows the typical transverse scans from the YBCO film at different  $2\theta$ . For  $2\theta < 0.3^\circ$ , one can see a sharp specular peak. However the a diffuse scattering intensity is suddenly grown up near the critical peak meanwhile the specular peak intensity is dropped down very quickly. Above the critical angle, strong intensity Yoneda wings appear [45]. The Yoneda wings is diffuse scattering due to the large surface roughness and the characteristics of x-ray [53]. In the neutron reflectivity studies on a 6000 Å thick YBCO film with the surface roughness  $170 \pm 30$  Å, we do not see the Yoneda wings at all. As  $2\theta$  increasing, the Yoneda wings move further angle from the specular peak position. The specular reflectivity shown in Fig. 44 was obtained by the transverse scans and subtracting the background scattering intensity from the specular peak intensity.

X-ray diffraction measurements were performed at higher angles, as shown

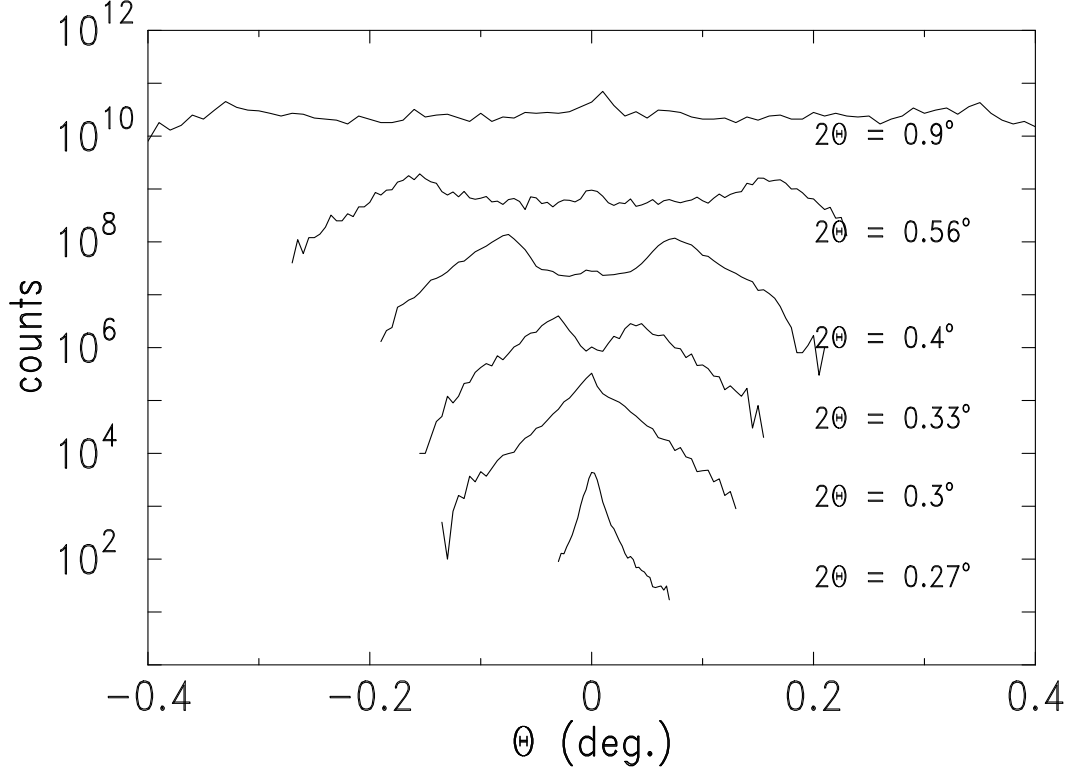


FIG. 45. X-ray transverse scans from the YBCO(2500Å) /SrTiO<sub>3</sub> film at different  $2\theta$ .

in Fig. 46. top shows the diffraction from Bragg peaks of (00l) YBCO and (00l) SrTiO<sub>3</sub>. YBCO is orthorhombic and SrTiO<sub>3</sub> is cubic. The c-axis lattice parameter of YBCO is  $\sim 3$  times of the SrTiO<sub>3</sub> lattice parameter. Therefore the Bragg peak (003) YBCO and (001) SrTiO<sub>3</sub> was not available to be distinguished because of the limit of the instrumental resolution. From the Bragg peak position, the c-axis lattice parameter of YBCO was determined to  $11.6785 \pm 0.0005$  Å which is corresponding to the oxygen concentration  $\sim 6.96$  and the critical temperature  $\sim 90$  K [55]. The broadening of the Bragg peaks is mainly contributed by the residual strain and finite sample thickness. As the broadening is a Gaussian shape,

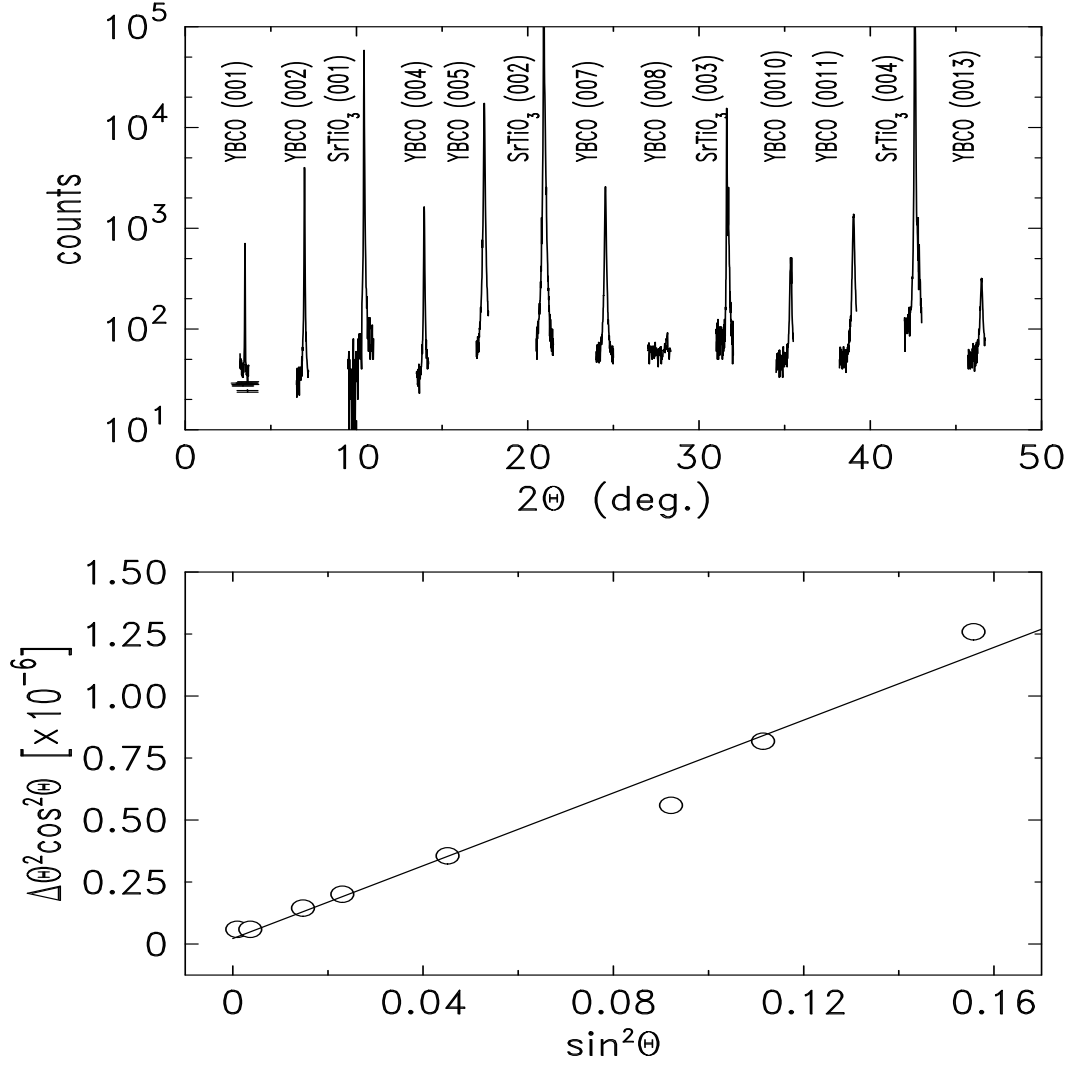


FIG. 46. Top shows the Bragg peaks of YBCO and SrTiO<sub>3</sub>. Bottom shows the broadenings of Bragg peaks as a function of  $\theta$  and the solid line is a best fit.

the broadenings as a function of  $\theta$  can be described to [56],

$$\Delta\theta^2 \cos^2\theta = \sin^2\theta \left( \frac{\Delta d}{d} \right)^2 + \left( \frac{\lambda}{L} \right)^2 \dots\dots\dots (7.3)$$

where  $d$  is lattice parameter along scattering plane and  $\lambda$  is incident wave length.

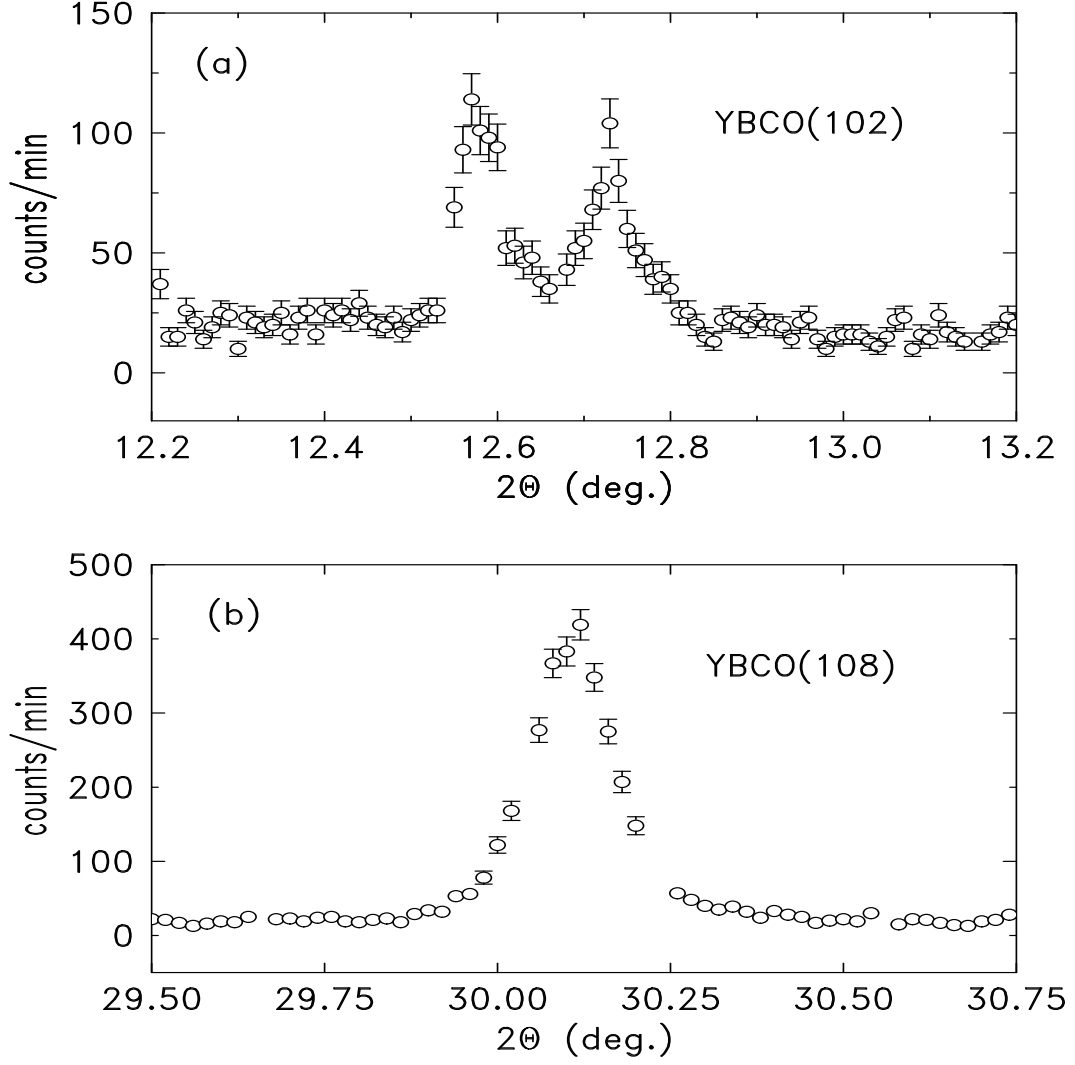


FIG. 47. (a) shows the Bragg diffraction at (102) of YBCO single crystal and (b) for (108) Bragg peak.

Fig. 46 bottom the broadening as a function of  $\theta$ . A best fit, solid line, gives that the film thickness  $L$  is  $\sim 2907 \text{ \AA}$  and the residual strain  $\Delta d / d$  is  $2.71 \times 10^{-3} \pm 6.86 \times 10^{-4}$ .

X-ray diffraction was also studied along (101) direction of the YBCO crystal.

Figure 47 shows the longitudinal scans near (102) and (108) Bragg peaks of YBCO. Figure 47 (a) obviously shows two peaks at (102). The reason why we did not observe the two peaks at (108) is the limit of instrumental resolution. The two peaks at (102) indicates that the crystal is in twin structure corresponding to (102) and (012). The lattice parameters, a and b, of YBCO are mixed in a sample plane. From the peak positions, the lattice parameters could be determined to be  $a = 3.828 \text{ \AA}$  and  $b = 3.88 \text{ \AA}$ .

### 7.3. Interdiffusion at YBCO Metal Interface

In this section, x-ray reflectivity studies at interfaces of YBCO superconductor and metals, Au /YBCO, Ag /YBCO and Pb /YBCO will be discussed [57]. For the x-ray reflectivity studies, a YBCO(300Å) /SrTiO<sub>3</sub> film, a Au(300Å) /YBCO(300Å) /SrTiO<sub>3</sub> film and a Pb(300Å) /YBCO(300Å) /SrTiO<sub>3</sub> film were sputtered on SrTiO<sub>3</sub> (100) substrate with off-axis magnetron sputter deposition [36] by L. H. Greene's group at University of Illinois-Urbana. The YBCO (300Å) layer was sputtered in 110 mTorr total pressure of (Ar + O<sub>2</sub>) - in the ratio Ar : O<sub>2</sub> = 5 : 1; the substrates temperature was held at 720 °C during the sputtering process. These parameters were used in order to get a smooth surface. After sputtering the YBCO layer, one of the YBCO thin films was covered with a mask (stainless steel) *in-situ* and the Au (300Å) layer was sputtered on the other film, in 7 mTorr Ar only. The substrate temperature was held at 65 °C during this part of the sputtering process. For the Pb deposition, a YBCO (300Å) film was moved to

an other chamber and Pb (300Å) was evaporated on the YBCO (300Å) film. The resistivity of a film grown on the side at room temperature was 208  $\mu\Omega$  cm, and Tc measured to 89.5K with a transition width of about 0.5 K.

A Ag(300Å) /YBCO(300Å) and a Pb(300Å) /YBCO(300Å) film *in-situ* was deposited on SrTiO<sub>3</sub> (100) by a coevaporation technique [54]. During the growth of YBCO, the substrate was held at 750 °C and the O<sub>2</sub> partial pressure was  $\sim 1$  mTorr. After deposited YBCO, the chamber was pumped to 10<sup>-8</sup> Torr. In that pressure, Ag and Pb was evaporated on the YBCO film. The Tc of a similar sample was 86 K and the resistivity was 150  $\mu\Omega$  cm at room temperature.

The interdiffusion at YBCO metal interface was studied by x-ray reflectivity at room temperature and atmosphere. For the measurements, the Mo K <sub>$\alpha$ 1</sub>, wave length 0.70926 Å from a Ge(111) monochromator was used from a rotating anode line beam x-ray generator. The same scattering geometry as given in Sec. 7.1 was used.

### 7.3.1. YBCO(300Å)/SrTiO<sub>3</sub> by Sputtering

X-ray reflectivity from the 300 Å thick YBCO film which was deposited by magnetron sputter is shown in Fig. 48. The oscillations of the reflectivity corresponds to a 210 Å thickness of the YBCO film with  $14 \pm 0.5$  Å of the rms surface roughness. A best fit (solid line) shows that a 32 Å thick oxide layer had developed at the air/YBCO interface. The inset shows the x-ray scattering density

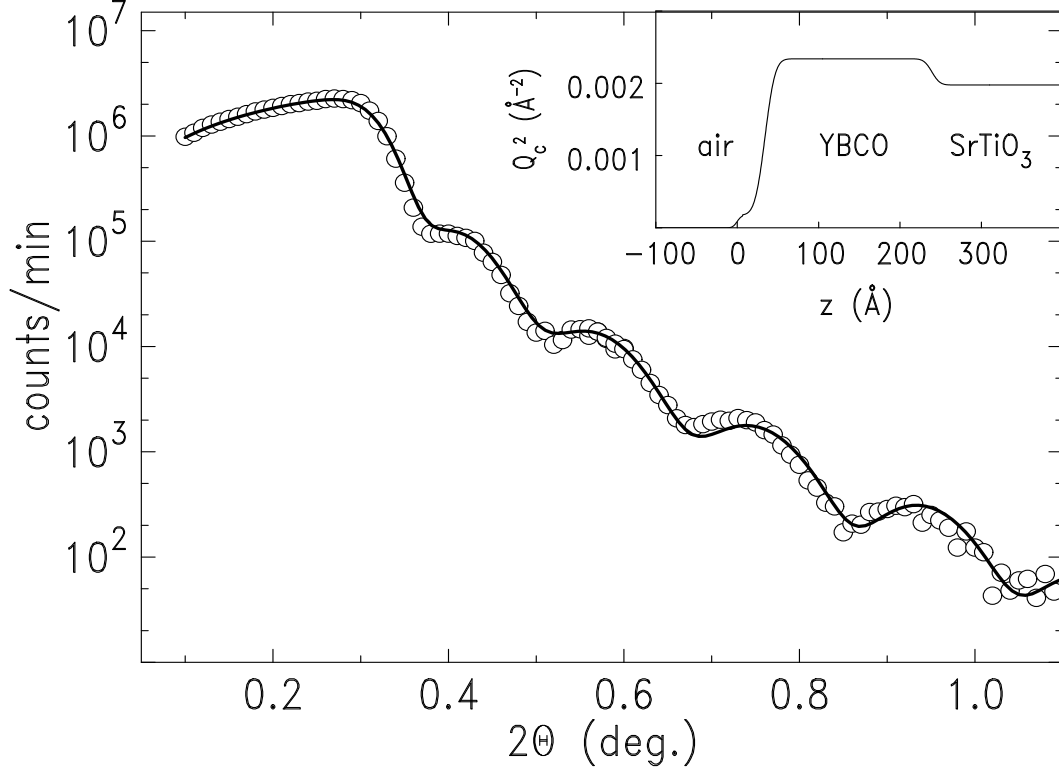


FIG. 48. X-ray reflectivity was measured on a 300  $\text{\AA}$  thick YBCO on a SrTiO<sub>3</sub>. The solid curve is a best fit. The film oscillations correspond to 210  $\text{\AA}$  of the YBCO. The scattering density profile of the sample is shown in the inset.

vs. position in scattering plane which is determined by incident and exiting wave vectors.

For more understanding on the crystal grains of the YBCO film and the substrate, the reflection at higher  $q_z$  was measured. Fig. 49 (a) shows the reflectivity, near the Bragg peaks, along the (100) direction of the SrTiO<sub>3</sub> substrate. According to the Bragg peak positions, the lattice parameter in  $c$ -axis is calculated

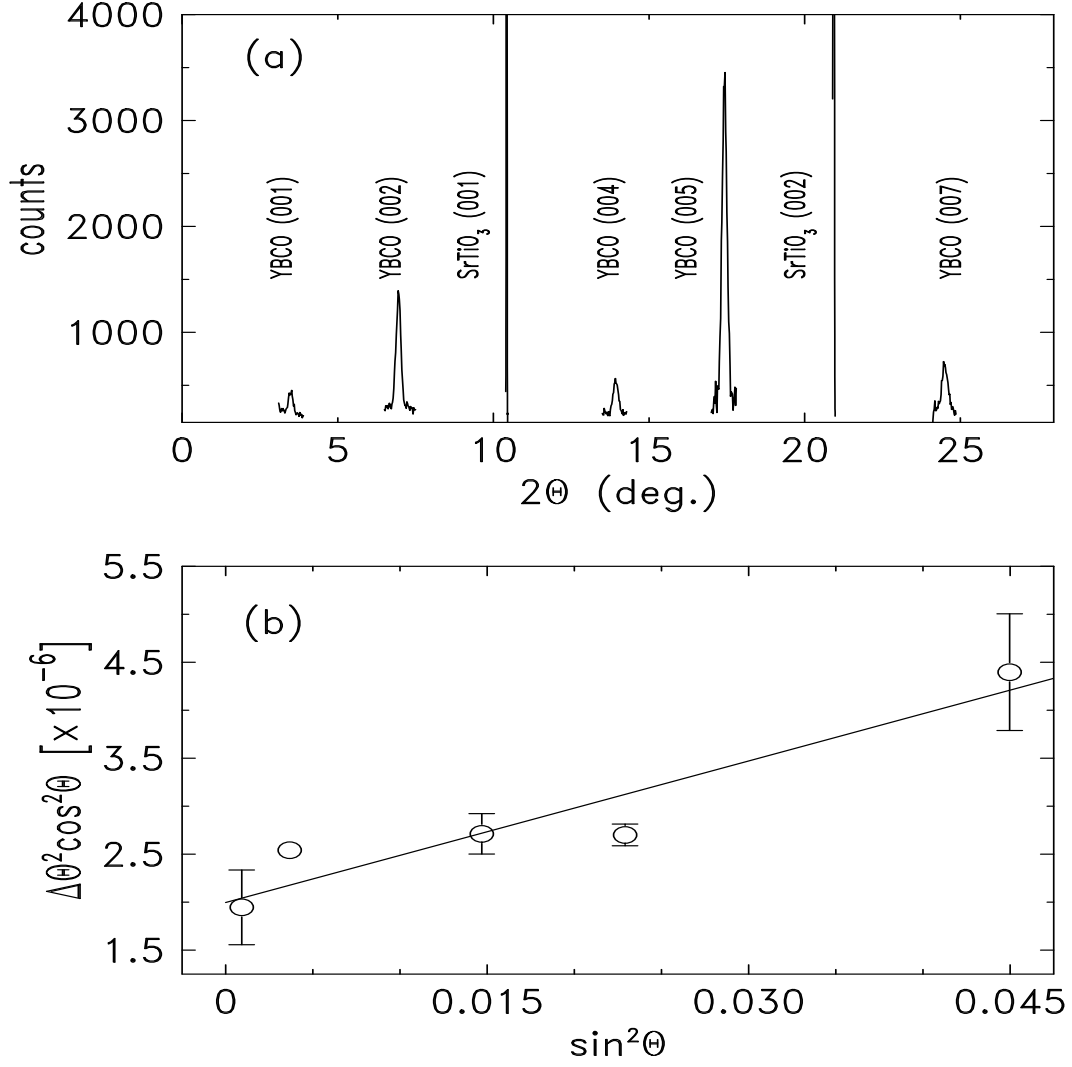


FIG. 49. (a) shows the Bragg diffraction from a c-axis YBCO single crystal on a SrTiO<sub>3</sub> (001) substrate. (b) shows the broadenings of the YBCO Bragg peaks in (a) vs.  $\theta$ .

to be  $11.69 \pm 0.01$  Å which is corresponding to the oxygen concentration 6.96 and critical temperature around 90 K [55].

Fig. 49 (b) shows the width of the Bragg peak as a function of  $\theta$ , as described in Eq. (7.3). The best fit, solid line, shows that the residual strain,  $\Delta d/d$ , is 0.7



$\pm 0.14$  % and the thickness of the film (L) is  $289 \pm 70$  Å which can be compared to the results of the grazing angle x-ray reflectivity measurement. These results shows that the grains are mostly oriented along the *c*-axis which is perpendicular to the surface. From a transverse scan at (005) YBCO Bragg peak, the mosaicity  $\sim 0.5^\circ$  was found.

### 7.3.2. *Au(300Å)/YBCO(300Å)/SrTiO<sub>3</sub> by Sputtering*

Gold has been widely used as a contact on devices. Au /YBCO junction has been used to study Josephson coupling as well as proximity effect [64]. The x-ray reflectivity studies of the interface at Au /YBCO would be useful for the potential applications of Au /YBCO bilayer of multilayer. Fig. 50 shows the x-ray reflectivity from a Au /YBCO /SrTiO<sub>3</sub> film. The critical angle is determined by the Au layer because the x-ray scattering density of Au is higher than that of YBCO and the x-ray characteristic length is shorter than the Au film thickness. The reflectivity is contributed by the reflections from the air/Au interface, the Au/YBCO interface and the YBCO /SrTiO<sub>3</sub> interface. At small angle, near the critical angle, the reflectivity is dominantly contributed by the beams reflected from the air /Au interface. And angle, the contribution of the beam reflected from the YBCO /SrTiO<sub>3</sub> interface dominates over the reflectivity. Therefore, one could independently determine the interdiffusion at each interface by analyzing the reflectivity data.

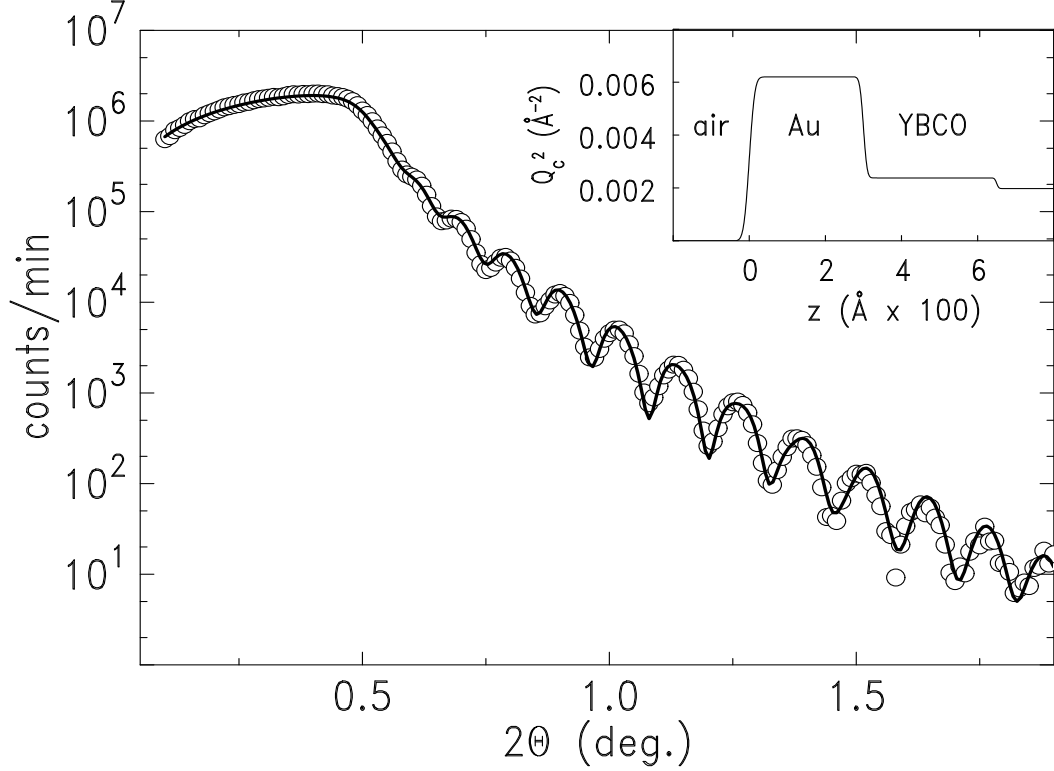


FIG. 50. X-ray reflectivity was measured from Au(300Å) /YBCO(300Å) /SrTiO<sub>3</sub> film and the solid line is a best fit. The scattering density profile of the film is shown in the inset.

The best fit, solid line, shows that the roughness at the air /Au interface is  $11.4 \pm 0.06$  Å and the thickness of Au film is  $300 \pm 0.25$  Å. The interdiffusion at the interface Au /YBCO was found to be  $7.56 \pm 0.07$  Å which is around 2 % of the YBCO film thickness ( $350 \pm 1$  Å). The roughness at the interface of YBCO /SrTiO<sub>3</sub> was less than 2 Å. The relatively clean YBCO film surface might suggest that the gold cap protects the developing reaction of the YBCO surface with the ambient. The inset shows the scattering density profile which is corresponding with the fit to the x-ray reflectivity data.

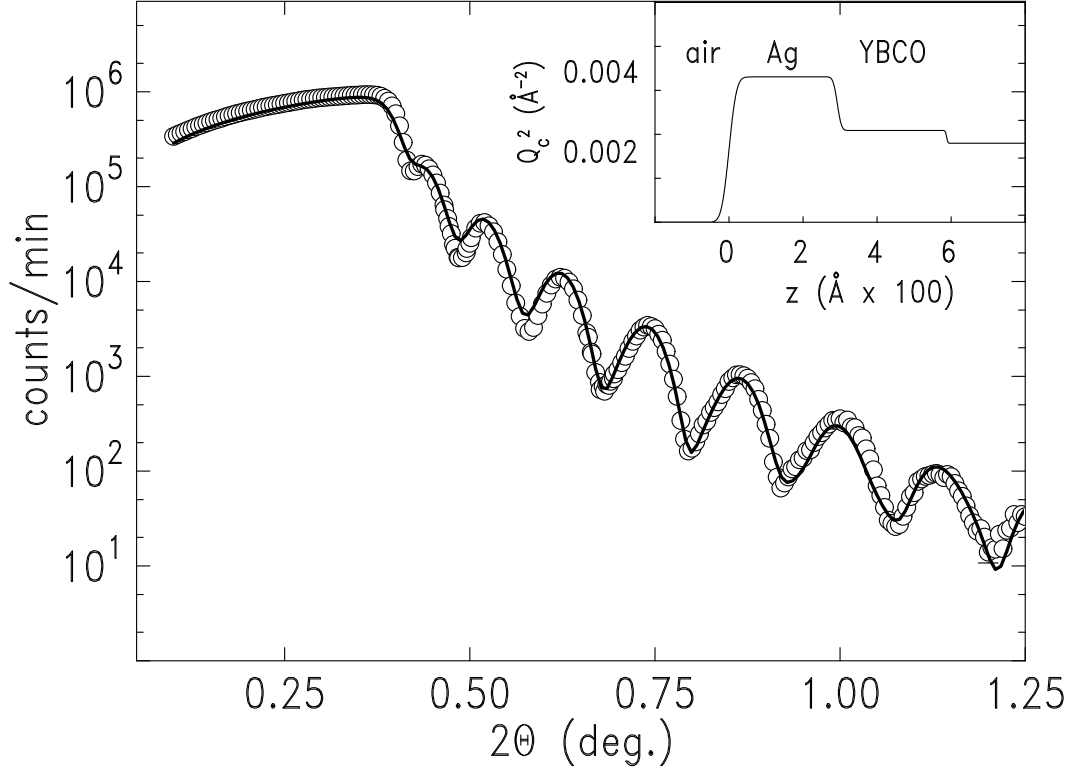


FIG. 51. X-ray reflectivity was measured from Ag(300Å) /YBCO(300Å) /SrTiO<sub>3</sub> film and the solid line is a best fit. The inset shows the scattering density profile of the film.

### 7.3.3. Ag(300Å)/YBCO(300Å)/SrTiO<sub>3</sub> by Coevaporation

Figure 51 shows the x-ray reflectivity from the Ag(300Å) /YBCO(300Å) /SrTiO<sub>3</sub> film grown *in-situ* by coevaporation technique [54]. The solid line is a best fit. From the fit, the roughness at the interface, air /Ag, was found to be  $10 \pm 2 \text{ \AA}$  which is around 3.4 % of the Ag film thickness. The interdiffusion at the Ag /YBCO interface,  $15 \pm 3 \text{ \AA}$  which is around 5 % of the YBCO film thickness was determined by the fit. The interdiffusion between Ag and the YBCO film can be compared to the roughness of the no capped YBCO film, although the

interdiffusion is around twice bigger than that of Au /YBCO. The inset shows the scattering density profile which is corresponding with the fit to the reflectivity data.

#### 7.3.4. $Pb(300\text{\AA})/YBCO(300\text{\AA})/SrTiO_3$

For the x-ray reflectivity studies, we have prepared two samples of which the growth conditions and techniques were different. For the first sample, Pb was deposited *ex-situ* on a YBCO film by the magnetron sputtering, as described above. The x-ray reflectivity on the Pb /YBCO /SrTiO<sub>3</sub> specimen is shown in Fig. 52 (a). Near the critical angle the reflectivity was sharply dropped down because of the huge surface roughness at the interface air /Pb ( $80 \pm 10 \text{ \AA}$ ) and the beating of reflections from the air/Pb interface and the Pb/YBCO interface.  $50 \pm 10 \text{ \AA}$  of the interdiffusion between Pb and the YBCO film was found by a best fit, solid line. The scattering density profile is shown in the inset. The scattering density of Pb was 84 % of the theoretical calculation. It suggests that the Pb film is entirely oxidized.

The other sample, Pb, was deposited *in-situ* on a YBCO film by a co-evaporation technique, after YBCO evaporated on a SrTiO<sub>3</sub> substrate by the same technique. Fig. 52 (b) shows the x-ray reflectivity from the sample. An oxide layer (thickness  $285 \pm 13 \text{ \AA}$ ) had developed on the top of the Pb film and the Pb film itself was totally oxidized. The interdiffusion on the interface Pb/YBCO was

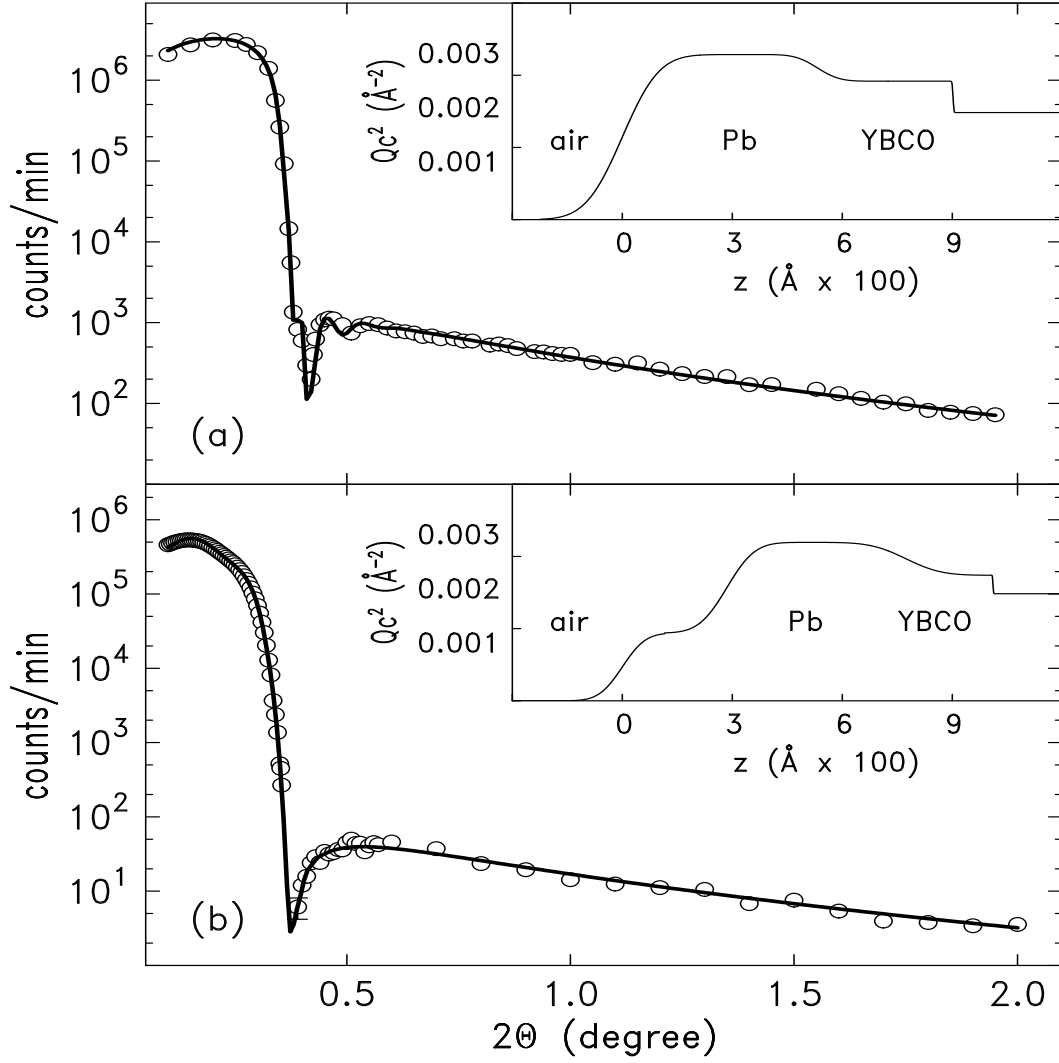


FIG. 52. X-ray reflectivity was measured as a function of  $2\theta$  from Pb /YBCO /SrTiO<sub>3</sub> films. (a) Pb was sputtered *ex-situ* on a YBCO film and (b) Pb was evaporated *in-situ* on a YBCO film. The insets show the scattering density profiles.

$75 \pm 15$   $\text{\AA}$  which is around 30 % of the YBCO film thickness was found by a best fit (solid line). The inset shows the scattering density profile.

X-ray diffraction measurements were performed on the films, near the Bragg peaks of YBCO. The diffractions from the Au /YBCO /SrTiO<sub>3</sub> and the Ag /YBCO

/SrTiO<sub>3</sub> shows that the YBCO film has a single crystal with *c*-axis perpendicular to the substrate surface however a Bragg peak from the Pb /YBCO films was not observed. It might suggest that the crystal grains of YBCO have been totally destroyed during interdiffusion developing at the Pb /YBCO interface.

In conclusions of x-ray reflectivity studies at YBCO metal interfaces, we have observed large interdiffusion at the interface of Pb /YBCO without depending on the growth conditions (*in-situ*, *ex-situ*) and deposition techniques (magnetron sputtering, co-evaporation). However interdiffusion at the interfaces of Au /YBCO and Ag /YBCO was much smaller. The surface of YBCO was rather protected from oxidation by the caps, Au and Ag. The thinner film has small surface roughness. However, we would find an oxide layer at a naked surface of YBCO without depending on the film thickness.

#### 7.4. X-ray Reflectivity from Nb Films

Nb, T<sub>c</sub> of  $\sim 9.2$  K [39], is a conventional type-II superconductor. The London penetration depth, around 400 Å, was found by using different techniques [8,7,61]. The coherence length of Nb 350 Å [61] was also known. As a superconductor, Nb, Nb alloy and Nb multilayers (Nb /Si, Nb /Al, Nb /Cu) have been widely studied for fundamental understanding of superconductivity and also practical applications because of the relatively smooth interface with other materials.

L. H. Greene's group have prepared Nb films for x-ray scattering studies

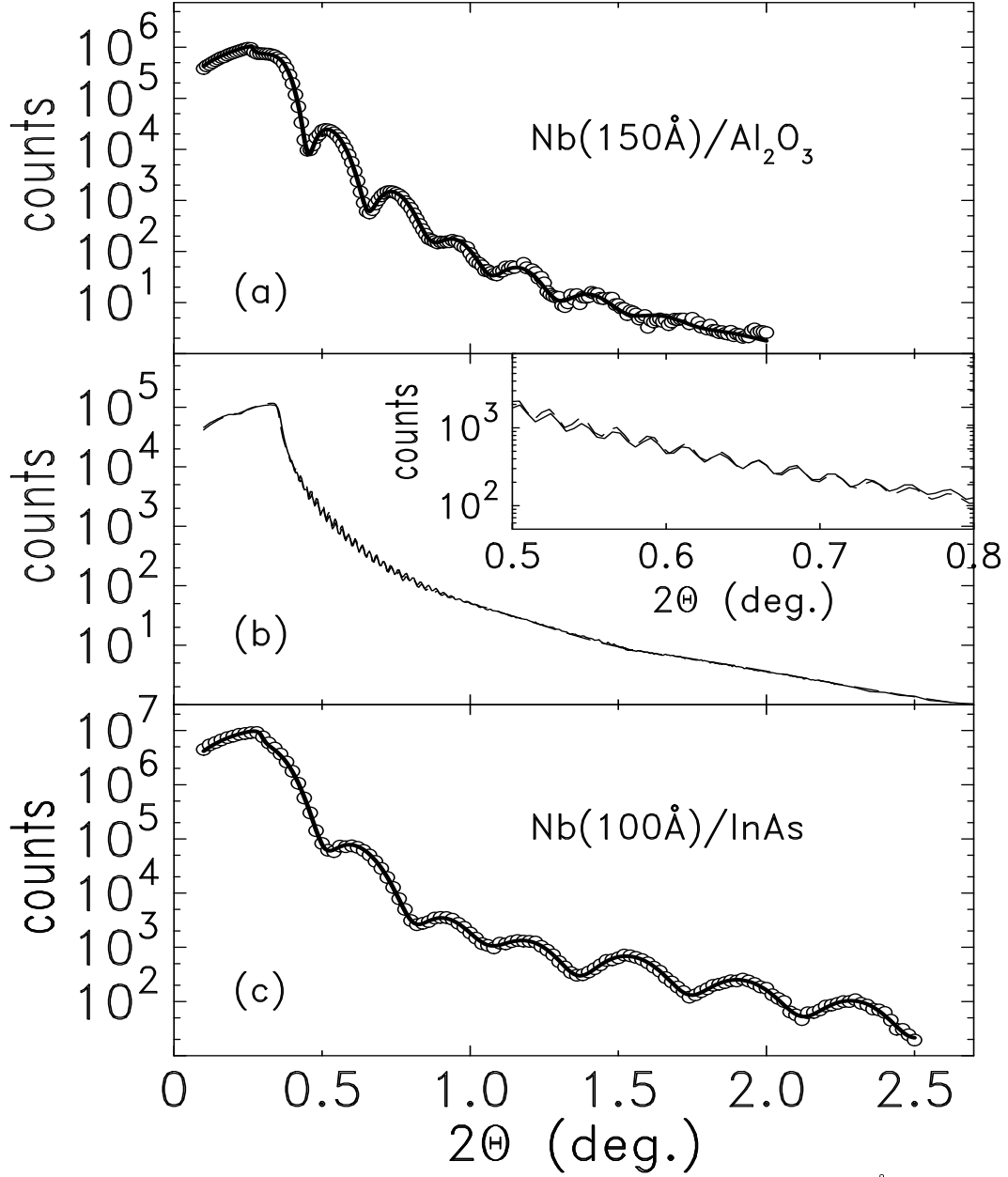


FIG. 53. (a) shows the grazing angle x-ray reflectivity from Nb(144Å) /Al<sub>2</sub>O<sub>3</sub>, (b) from Al(760Å) /Nb(1380Å) /Al<sub>2</sub>O<sub>3</sub> and (c) from Nb(97Å) /InAs.

by magnetron sputtering deposition [39]. Figure 53 (a) shows the x-ray specular reflectivity from a Nb /Al<sub>2</sub>O<sub>3</sub> measured as a function of  $2\theta$ . A best fit, solid line, shows that the thickness of Nb film is  $144.1 \pm 0.3$  Å with the roughness at air/Nb

interface  $16.6 \pm 2.5 \text{ \AA}$ . The roughness of the substrate,  $11.9 \pm 1.7 \text{ \AA}$  makes the film oscillations diminished at high angle. At the air /Nb interface, an oxide layer thickness  $15.8 \pm 0.2 \text{ \AA}$  with roughness  $2.3 \pm 0.2 \text{ \AA}$  have been developed.

Figure 53 (b) shows the x-ray reflectivity from a Al( $\sim 760 \text{ \AA}$ ) /Nb( $1380 \text{ \AA}$ ) /Al<sub>2</sub>O<sub>3</sub> film which has been used for spin-polarized neutron reflectivity studies on vortices at 2 K, as described in Sec. 5.4. The solid line is measured data and the dashed line is a best fit. However there was a fluctuation in the Nb thickness within  $\pm 20 \text{ \AA}$  depending on the position at the film surface. The non-uniformity of thickness occurs reducing the amplitude of the film oscillation in the reflectivity. The roughness at the interface, Al/Nb, of  $13 \pm 1 \text{ \AA}$  was found from a best fit. At higher angle, the small oscillation is corresponded to the thickness of  $37 \pm 2 \text{ \AA}$  which is located between the Nb film and the Al<sub>2</sub>O<sub>3</sub> substrate. The scattering density of the intermediate layer is lower than the Nb scattering density but higher than the substrate. By using x-ray reflectivity, it is difficult to find the information of Al layer because the signal from the Al layer was relatively weak due to the low scattering density. However, below the critical angle, the small bump was shown due to the x-ray absorption from Al layer in Fig. 53. The scattering density of the Al layer of  $\sim 10 \%$  lower than pure Al was determined from the fit. The position and depth of the bump is contributed by the thickness and absorption coefficient of the Al layer. The thickness of Al layer is  $760 \pm 55 \text{ \AA}$  and the roughness at the air /Al interface  $70 \pm 26 \text{ \AA}$  was found by the fit.

X-ray specular reflectivity from a Nb /InAs film measured as a function of



$2\theta$  is shown in Fig. 53 (c) and the solid line is a best fit. The fit shows the thickness of Nb film  $97.2 \pm 0.8 \text{ \AA}$  with roughness  $2.1 \pm 1.6 \text{ \AA}$ . At the top was a oxide layer of which thickness is  $22 \pm 1 \text{ \AA}$  with the roughness  $7 \pm 5 \text{ \AA}$ . The substrate, InAs, has a smooth surface, roughness  $1.4 \pm 1.0 \text{ \AA}$ . However with assuming a layer between the Nb film and the substrate with thickness  $10.4 \pm 2.3 \text{ \AA}$ , one could obtain a better fit.

In conclusions, the surface of Nb was relatively smooth, as deposited on the substrates,  $\text{Al}_2\text{O}_3$  and InAs. There is an oxide layer developed at air/Nb interface. And we observed an extra-layer at the interface Nb/substrate without depending on material of substrates.

### 7.5. X-ray Diffraction from a Nb/Al Multilayered Film

Artificially layered structures are attractive for practical application as well as academic research. Nb /Al multilayered films have been used to study the vortex-surface interaction by using SQUID and spin-polarized neutron reflectivity measurements, as discussed in Ch. 6. In this chapter, I will discuss the x-ray diffraction studies on a Nb /Al multilayer.

The grazing angle x-ray reflectivity from a Nb / $[\text{Al}(19\text{\AA}) \text{ /Nb}(74\text{\AA})] \times 20$  /Si film was measured as a function of  $2\theta$  with  $\lambda 0.70926 \text{ \AA}$ , as shown in figure 54. The solid line is a best fit to a reflectivity model [44] and shows that Nb( $120 \pm 20 \text{ \AA}$ ) / $[\text{Al}(19 \pm 1.5 \text{ \AA}) \text{ /Nb}(74.5 \pm 2.5 \text{ \AA})] \times 20$  /Si and at the interface of air /Nb, a  $\sim 60 \text{ \AA}$

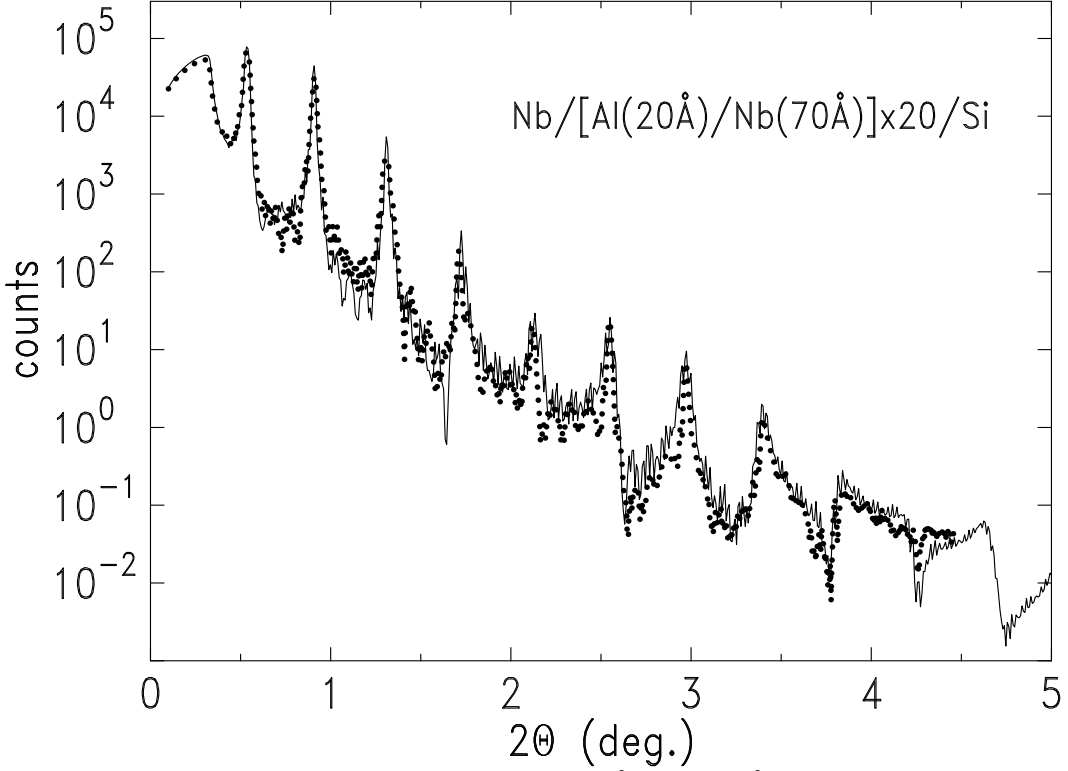


FIG. 54. X-ray reflectivity from a Nb / $[Al(19\text{\AA}) /Nb(74\text{\AA})] \times 20$  /Si film is measured as a function of  $2\theta$ .

thick layer, scattering density half of Nb made a better fit. The surface roughness of the substrate was  $\sim 2.2$  Å and the bottom Nb layer had 5 Å surface roughness and the bottom Al layer had 2.2 Å surface roughness. However, as the bilayers were stacked in the model, 0.5 Å surface roughness was added the Nb layer. The top Nb layer roughness was 15 Å. For the Al bilayer, 0.16 Å added the Al layer for each subsequent bilayer thus the top Al layer roughness was 5.4 Å.

The x-ray diffraction peaks from the multilayer up to the 9<sup>th</sup> order could be observed. The peak positions corresponds to the bilayer (Nb/Al) thickness  $\sim 94$  Å. The reflectivity intensity at the 5th peak relatively weak suggests that the

thickness ratio, Nb : Al (or Al : Nb) is 4 : 1 and the fit shows that Nb : Al is 3.92 : 1 which is close to fabricating parameters. The critical angle below which beam is totally reflected by surface is mainly determined by the top Nb scattering density however the bilayer Nb/Al also affects the critical angle.

Figure 55 shows the x-ray transverse scans on the Nb / [Al(19Å) / Nb(74Å)]  $\times$  20 /Si sample. At  $2\theta$  1.3 and 1.7 are the multilayer Bragg peaks and the others are measured at intermediate angle. At  $2\theta$  1.3, one can clearly see the second-order multilayer Bragg peak at  $\theta \pm \sim 0.21^\circ$  which has been previously studied by J. B. Kortright *et al.* [62]. And the diffusion scattering from a multilayer Bragg peak have been insensitively studied by D. E. Savage *et al.* [63]. In this thesis, I will not discuss the roughness correlation in a multilayer film in detail. In Fig. 55, first we will notice that the transverse width at a multilayer Bragg peak is narrow than at a intermediate angle. The broadening at intermediate angles is smaller at higher  $2\theta$ . The broadening will be determined by surface bending, mismatch of the surface direction of multilayers, slight difference of the thickness of multilayers and instrumental resolution. The contribution of the surface bending effect and the surface direction mismatch of multilayers to the broadening is basically same in a multilayer. And the broadening due to the bending effect is identical as  $2\theta$  changed. The diffraction domain size could be the main factor for reducing the broadening at higher  $2\theta$ .

For further understanding the crystal structures in Nb / [Al(19Å) / Nb(74Å)]  $\times$  20 /Si, x-ray reflectivity was measured at higher angle, as shown in Fig. 56. It

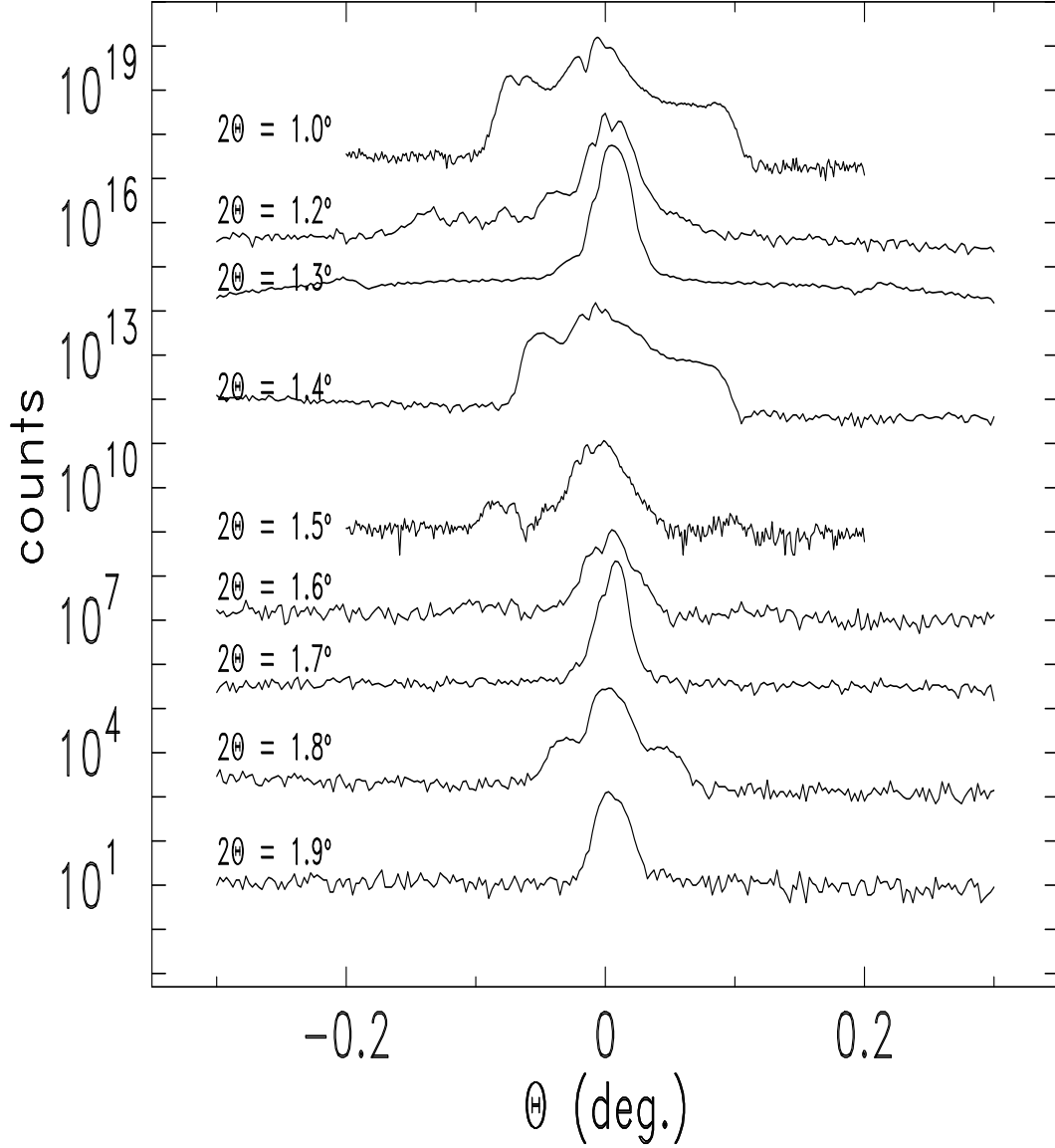


FIG. 55. X-ray transverse scans from Nb  $/[Al(19\text{\AA}) /Nb(74\text{\AA})] \times 20$  /Si at different  $2\theta$  are shown.

shows that Si(111) substrate is in the scattering plane which is determined by incident and exiting wave vectors. As Si is a perfect crystal, one will not observe the (222) Si Bragg peak. The observation of the (222) Si Bragg peak implies that the x-ray beam used for this measurement is mixed with the wave length  $\lambda / 2$ .

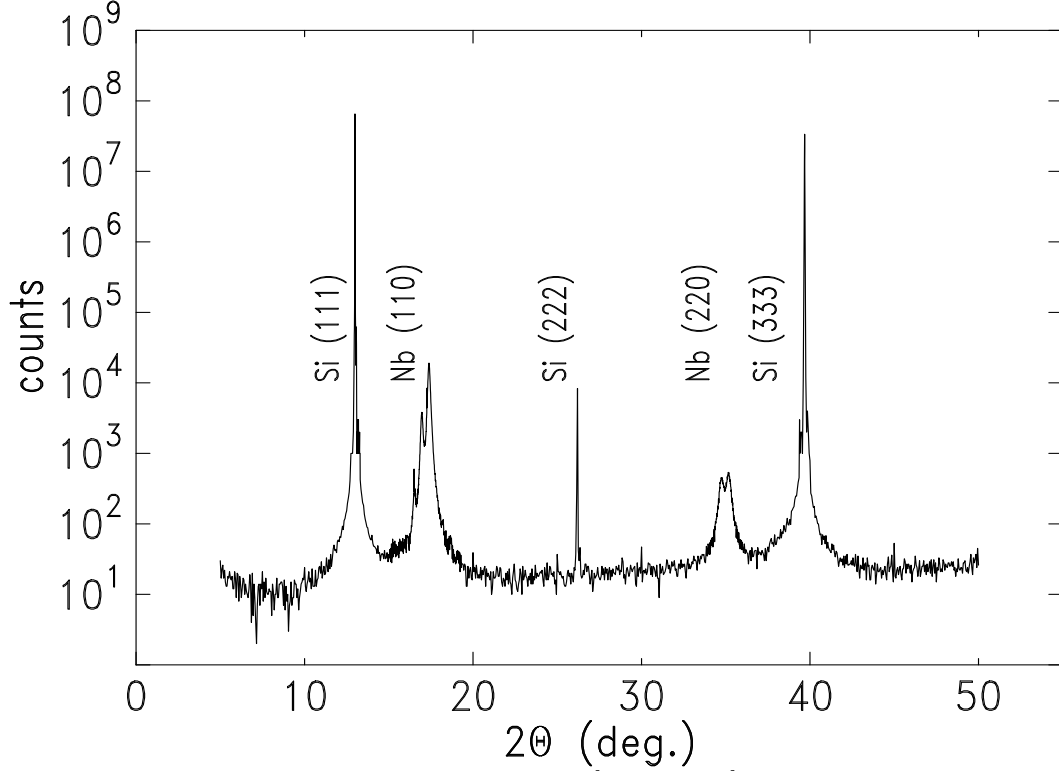


FIG. 56. X-ray diffraction from Nb / $[Al(19\text{\AA}) / Nb(70\text{\AA})] \times 20$  /Si was measured as a function of  $2\theta$ .

We also could observe two more peaks, Nb(110) and Nb(220). Because of the instrumental resolution limit, it is not possible to distinguish if the peaks are from Nb layer or Al layer because Nb(110) and Al(111) are corresponding to  $2\theta$   $17.692^\circ$  and  $2\theta$   $17.45^\circ$  each other. And Nb(220) and Al(222) are corresponding to  $2\theta$   $37.48^\circ$  and  $37.348^\circ$ . The oscillations at Nb(110) Bragg peak are due to the multilayer.

In conclusions of x-ray reflectivity studies on Al /Nb multilayer, we could observe several multilayer Bragg peaks from a Nb / $[Al(19\text{\AA}) / Nb(74\text{\AA})] \times 20$  /Si film. By fitting the measurement data to a reflectivity model calculation [44], we could obtained the rms roughness and average thickness of each multilayer.

From the transverse scans, we could obtain more information of the multilayer surfaces. However, to more understand the multilayer diffusion scattering, we will need further studies. At the high angle x-ray diffraction studies, two Bragg peaks from Nb or/and Al were observed. To know if they are from Nb or Al, we need a better resolution and a strong intensity beam.



- 
- [1] B. E. Warren, *X-ray diffraction*, (Dover, New York, 1990); A. Guinier, *X-ray diffraction in crystals, imperfect crystals, and amorphous bodies*, (Dover, New York, 1994).
- [2] G. E. Bacon, *Neutron diffraction*, (Oxford, New York, 3th Edt., 1975); G. L. Squires, *Introduction to the theory of thermal neutron scattering*, (Cambridge, New York, 1978); H. Dosch, *Critical phenomena at surfaces and interfaces* (Springer-Verlag, New York, 1992).
- [3] C. Detlefs, A. H. M. Z. Islam, A. I. Goldman, C. Stassis, P. C. Canfield, J. P. Hill, D. Gibbs, Phys. Rev. B **55**, R680 (1997).
- [4] C. F. Majkrzak, Physica B **221**, 342 (1996); A. Schreyer, J. F. Ankner, Th. Zeidler, H. Zabel, M. Schäfer, J. A. Wolf, P. Grünberg, C. F. Majkrzak, Phys. Rev. B **52**, 16066 (1995); J. F. Ankner, A. Schreyer, H. Zabel, J. A. Borchers, C. F. Majkrzak, M. Schäfer, J. A. Wolf, P. Grünberg, M. E. Filipkowski, C. J. Gutierrez, J. J. Krebs, G. A. Prinz, J. Appl. Phys. **76**, 7092 (1994).
- [5] P. G. de Gennes, *Superconductivity of Metals and Alloys* (Addison-Wesley, New York, 1989); T. P. Orlando, K. A. Delin, *Foundations of Applied Superconductivity* (Addison-Wesley, New York, 1991).
- [6] G. P. Felcher, R. T. Kampwirth, K. E. Gray, R. Felici, Phys. Rev. Lett. **52**, 1539 (1984).
- [7] H. Zhang, J. W. Lynn, C. F. Majkrzak, S. K. Satija, J. H. Kang, X. D. Wu, Phys. Rev. B **52**, 10 395 (1995).
- [8] A. Mansour, R. O. Hilleke, G. P. Felcher, R. B. Lainbowitz, P. Chaudhari, S. S. P.



- Parkin *Physica B* **156** & **157**, 867 (1989); R. Felici, J. Penfold, R. C. Ward, E. Olsi & C. Matarotta, *Nature* **329**, 523 (1987); S. V. Gaponov, E. B. Dokukin, D. A. Korneev, E. B. Klyuenkov, W. Löbner, V. V. Pasyuk, A. V. Petrenko, Kh. Rzhany, and L. P. Chernenko, *JETP Lett.* **49**, 316 (1989); V. Lauter-Pasyuk, H. J. Aksenov, E. L. Kornilov, A. V. Petrenko, P. Leiderer, *Physica B* **248** 166 (1998).
- [9] G. Blatter, M. V. Feigel'man, V. B. Geshkenbein, A. I. Larkin, V. M. Vinokur, *Rev. Mod. Phys.* **66**, 1125 (1994).
- [10] G. W. Crabtree and D. R. Nelson, *Physics Today* (April, 1997), pp. 39.
- [11] Matthew F. Schmidt, N. E. Israeloff, and A. M. Goldman, *Phys. Rev. Lett.* **70**, 2162 (1993).
- [12] J. W. Lynn, N. Rosov, T. E. Grigereit, H. Zhang, and T. W. Clinton, *Phys. Rev. Lett.* **72**, 3413 (1994).
- [13] P. L. Gammel, D. J. Bishop, G. J. Dolan, J. R. Kwo, C. A. Murray, L. F. Schneemeyer, and J. V. Waszczak, *Phys. Rev. Lett.* **59**, 2592 (1987).
- [14] K. Harada, T. Matsuda, J. Bonevich, M. Igarashi, S. Kondo, G. Pozzi, U. Kawabe, & A. Tonomura, *Nature* **360**, 51 (1992).
- [15] H. F. Hess, R. B. Robinson, R. C. Dynes, J. M. Valles, Jr., and J. V. Waszczak, *Phys. Rev. Lett.* **62**, 214 (1989).
- [16] A. M. Chang, H. D. Hallen, L. Harriott, H. F. Hess, H. L. Kao, J. Kwo, R. E. Miller, R. Wolfe, and J. van der Ziel, *Appl. Phys. Lett.* **61**, 1974 (1992).
- [17] A. Tonomura, *Adv. Phys.* **41**, 59 (1992); J. E. Bonevich, K. Harada, T. Matsuda, H. Kasai, T. Yoshida, G. Pozzi, *Phys. Rev. Lett.* **70**, 2952 (1993).
- [18] D. K. Christen, H. R. Kerchner, S. T. Sekula, and P. Thorel, *Phys. Rev. B* **21**, 102

- (1980); D. Cribier, B. Jacrot, L. M. Rao, and B. Farnoux, Phys. Lett. **9**, 106 (1964); E. M. Forgan, D. Mck. Paul, H. A. Mook, P. A. Timmins, H. Keller, S. Sutton, J. S. Abell, Nature **343**, 735 (1990); U. Yaron, P. L. Gammel, G. S. Boebinger, G. Aeppli, P. Schiffer, E. Bucher, and D. J. Bishop, Phys. Rev. Lett. **78**, 3185 (1997).
- [19] S.-W. Han, J. F. Ankner, H. Kaiser, P. F. Miceli, E. Paraoanu, L. H. Greene, Phys. Rev. B **59**, 14 692 (1999)
- [20] J. Guimpel, L. Civale, F. de la Cruz, J. M. Murduck, I. K. Schuller, Phys. Rev. B **38**, 2342 (1988); I. K. Schuller, J. Guimpel, Y. Bruynseraede, MRS BULLETIN, 29 (Feb., 1990).
- [21] S. H. Brongersma, E. Verweij, N. J. Koeman, D. G. de Groot, R. Griessen, and B. I. Ivlev, Phys. Rev. Lett. **71**, 2319 (1993).
- [22] P. Lobotka, I. Vávra, R. Senderák, D. Machajdík, M. Jergel, Š. Gaži, E. Rosseel, M. Baert, Y. Bruynseraede, M. Forsthuber, G. Hilscher, Physica C **299**, 231 (1994).
- [23] S. M. Yusuf, E. E. Fullerton, R. M. Osgood II, G. P. Felcher, J. Appl. Phys. **83**, 6801 (1998).
- [24] S.-W. Han, J. Farmer, P. F. Miceli, G. P. Felcher, G. Kiehne, J. Ketterson (to be published).
- [25] S.-W. Han, H. Kaiser, J. Farmer, P. F. Miceli, I. R. Roshchin, L. H. Greene (to be published).
- [26] D. E. Farrell, C. M. Williams, S. A. Wolf, N. P. Bansal, V. G. Kogan, Phys. Rev. Lett. **61**, 2805 (1988).
- [27] A. Sudbø, E. H. Brandt, Phys. Rev. Lett. **67**, 3176 (1991); D. A. Huse, Phys. Rev. B **46**, 8621 (1992).

- [28] A. A. Abrikosov, *Fundamentals of the theory of metals* (North-Holland, 1988).
- [29] L. Krusin-Elbaum, R. L. Greene, F. Holtzberg, A. P. Malozemoff, and Y. Yeshurun, Phys. Rev. Lett. **62**, 217 (1989); J. Annett, N. Goldenfeld, S. R. Renn, Phys. Rev. B **43**, 2778 (1991); W. N. Hardy, D. A. Bonn, D. C. Morgan, R. Liang, K. Zhang, Phys. Rev. Lett. **70**, 3999 (1993); J. Y. Lee, K. M. Paget, T. R. Lemberger, Phys. Rev. B **50**, 3337 (1994).
- [30] S.-W. Han, J. Ankner, H. Kaiser, P. F. Miceli, E. Paraoanu, L. H. Greene (to be published)
- [31] R. M. Moon, T. Riste, W. C. Koehler, Phys. Rev. **181**, 920 (1969).
- [32] K.E. Gray, G. P. Felcher, R. T. Kampwirth, R. Hilleke, Phys. Rev. B **42**, 3971 (1990).
- [33] H. Kaiser, K. Hamacher, R. Kulasekere, W.-T. Lee, J. F. Ankner, B. DeFacio, P. Miceli and D. L. Worcester, in *Inverse Optics III*, SPIE Conf. Proc. Vol. **2241** (SPIE, Bellingham, Washington, 1994), pp. 78 - 89; R. Kulasekere's thesis for the degree of Ph. D..
- [34] C. P. Bean, Phys. Rev. Lett. **8**, 250 (1962).
- [35] I. S. Gradshteyn, *Table of Integrals*, p. 705.
- [36] L.H. Greene, B.G. Bagley, W.L. Feldman J.B. Barner, F. Shokoohi, P.F. Miceli, B.J. Wilkins, V. Pendrick, D. Kalokitis and A. Fathy, Appl. Phys. Lett. **59**, 1629 (1991); J. Lesueur, L.H. Greene, W.L. Feldman and A. Inam, Physica C **191**, 325 (1992); M. Covington, R. Scheuerer, K. Bloom, L. H. Greene, Appl. Phys. Lett. **68**, 1717 (1996).
- [37] S. J. Duray, D. B. Buchholz, S. N. Song, D. S. Richeson, J. B. .

- [38] S.-W. Han, J. A. Pitney, P. F. Miceli, M. Covington, L. H. Greene, M. J. Godbole, D. H. Lowndes, *Physica B* **221**, 235 (1996).
- [39] L. H. Greene, A. C. Abeyta, I. V. Roshchin, I. K. Robinson, J. F. Dirsten, T. A. Tanzer, P. W. Bohn, *Proceedings of the SPIE Conference on Spectroscopic Studies of Superconductors San Jose, CA, 27 Jan - 2 Feb., 1996*.
- [40] A. P. Malozemoff, L. Krusin-Elbaum, D. C. Cronmeyer, Y. Yeshurun, F. Holtzberg, *Phys. Rev. B* **38**, 6490 (1988).
- [41] H. F. Hess, C. A. Murry, J. V. Waszczak, *Phys. Rev. B* **50**, 16 528 (1994); C. A. Bolle, P. L. Gammel, D. G. Grier, C. A. Murray, D. J. Bishop, D. B. Mitzi, A. Kapitulnik, *Phys. Rev. Lett.* **66**, 112 (1991).
- [42] M. McElfresh, S. Li, R. Sager, *Effects of magnetic field uniformity on the measurement of superconducting sample* (Quantum Design, 1996); M. McElfresh, *Fundamentals of Magnetism and magnetic measurements* (Quantum Design, 1994).
- [43] D. Craik, *Magnetism Principles and Applications* (Wiley, New York, 1995) p. 298.
- [44] L.G. Parratt, *Phys. Rev. B* **359** (1954); P. F. Miceli, *Semiconductor Interfaces, Microstructures and Devices: Properties and Applications*, Ed. Z. C. Feng, (IOP publishing, Bristol, 1993), P. 87.
- [45] S. K. Sinha, E. B. Sirota, S. Garoff, H. B. Stanley, *Phys. Rev. B* **38**, 2297 (1988).
- [46] G. B. Lubkin, *Physics Today* (March, 1996), pp 48.
- [47] M. Covington, R. Scheuerer, K. Bloom, L. H. Greene, *Appl. Phys. Lett.* **68**, 1717 (1996); J. Lesueur, M. Aprili, A. Goulon, T. J. Horton, L. Dumoulin; J. Ping, Zhou, J. T. McDevitt, Q. X. Jia, *Appl. Phys. Lett.* **72**, 848 (1998); Q. X. Jia, X. D. Wu, S. R. Foltyn, D. Reagor, M. Hawley, K. N. Springer, P. Tiwari, C. Mombourquette, R. J. Houlton, I. H. Campbell, H. Kung, T. E. Mitchell, D. E. Peterson, *IEEE Trans.*

- Appl. Supercond. **5**, 2103 (1993).
- [48] W. J. Lin, P. D. Hatton, F. Baudenbacher, J. Santiso, Physica B **248** 56.
- [49] D. H. Lowndes, in Modern Topics in Single Crystal Growth (Amer. Inst. of Physics, New York, in press).
- [50] S. J. Duray, D. B. Buchholz, S. N. Song, D. S. Richeson, J. B. Ketterson, T. J. Marks, R. P. H. Chang, Appl. Phys. Lett. **59**, 1503 (1991).
- [51] P. Tiwari, T. Zheleva, J. Narayan, Mat. Res. Soc. Symp. Proc. **285**, 311 (1993).
- [52] S. E. Russek, A. Roshko, S. C. Sanders, D. A. Rudman, J. W. Ekin, J. Moreland, Mat. Res. Soc. Symp. Proc. **285**, 305 (1993).
- [53] Y. Yoneda, Phys. Rev. **131**, 2010 (1963).
- [54] J. Lesueur, M. Aprili, A. Goulon, T. J. Horton, L. Dumoulin, Phys. Rev. B **55**, 3390 (1997).
- [55] D. C. Johnston, A. J. Jacobsen, J. M. Newsam, J. T. Lewndowski, D. P. Goshorn, D. Xie and W. B. Yelon, in *Chemistry of High Temperature Superconductors*, edited by D. L. Nelson, M. S. Wittingham and T. F. George (American Chemical Society, Washington, DC, 1987), p. 136.
- [56] P. F. Miceli, T. Venkatesan, X. D. Wu, J. A. Potenza, AIP Conf. Proc. **165**, 150 (1988).
- [57] S.-W. Han, S. Tripathy, P. F. Miceli, E. Paraoanu, M. Corvington, L. H. Greene (to be published).
- [58] R. K. Singh et al., Appl. Phys. Lett, **60** 255 (1992); D. Kumar et al., Appl. Phys. Lett. **60** 3522 (1993); R. Pinto et al., Physica C **207** 13 (1993).
- [59] K. A. Delin, A. W. Kleinsasser, Supercond. Sci. Technol, **9** 227 (1996).

- [60] P. G. De Gennes, Rev. Mod. Phys. 225 (Jan., 1964).
- [61] A. V. Pronin, M. Dressel, A. Pimenov, and A. Loidl, Phys. Rev. B **57**, 14 416 (1998)
- [62] J. B. Kortright, J. Appl. Phys. **70**, 3620 (1991).
- [63] D. E. Savage, J. Kleiner, N. Schimke, Y.-H. Phang, T. Jankowski, J. Jacobs, R. Kariotis, M. G. Lagally, J. Appl. Phys. **69**, 1411 (1991); Y. H. Phang, D. E. Savage, R. Kariotis, M. G. Lagally, J. Appl. Phys. **74**, 3181 (1993).
- [64] T. Xiang, J. M. Wheatley, Phys. Rev. Lett. **76**, 134 (1996); E. Polturak, G. Koren, D. Cohen, E. Aharoni, G. Deutscher, Phys. Rev. Lett. **67**, 3038 (1991); L. Antognazza, S. J. Berkowitz, T. H. Geballe, K. Char, Phys. Rev. B **51**, 8560 (1995); M. A. M. Gijs, D. Scholten, Th. van Rooy, A. M. Gerrits, Phys. Rev. B **41**, 11627 (1990); V. V. Khanin, D. V. Shuvaev, O. V. Snigirev, E. S. Soldatov, A. S. Trifonov, I. I. Vengrus, JETP Lett. **63**, 1041 (1996); A. W. Kleinsasser, K. A. Delin, Appl. Phys. Lett. **66**, 102 (1995); M. S. Pambianchi, C. Kwon, T. Venkatesan, Steven M. Anlag, Phys. Rev. B **54**, 15513 (1996).



## VITA

Han, Sang-Wook was born February 10, 1964 in Samchuk, Korea. He received a B.S. degree in Physics from Kyung Pook National University in 1989, a M.S. degree in Physics from Western Illinois University in 1993 and a Ph. D. degree in Physics from the University of Missouri-Columbia in 1999. He got married with Im, Kyungha in 1997 and his first daughter, Han, Jeahe Jenny was born October 20, 1999.

He is presently a faculty member of the Department of Physics at University of Washington, Seattle, Washington.